Josephson effect in anisotropic superconductors.

Nikos Stefanakis

Department of Physics

University of Crete

Josephson effect in anisotropic superconductors
by Nikos Stefanakis, 2001

Project Supervisor:

Nikos Flytzanis, Assoc. Prof.
University of Crete
Department of Physics
P.O. Box 2208,
GR-71003, Heraklion, Crete
Greece

Typesetting by LaTeX.

Αφιερώνεται
στη μνήμη του πατέρα μου

Contents

Preface

The present report was written in partial fulfillment for the requirements of Ph.D. degree for the University of Crete, Greece. The work was carried out at the Department of Physics, University of Crete, during the period from (March 1) 1996 to 2001, under the supervision of Assoc. Prof. N. Flytzanis.

Chapters 2,3,4 are based on published papers [22, 92, 88, 89] and conference proceedings [87, 93, 86], chapter 5 is based on a paper accepted for publication [85], and has recently been presented in conferences [90, 91].

The objective of the present report is to provide information concerning the phase sensitive tests on the symmetry of the order parameter in anisotropic superconductors, based on the Josephson effect. The approach used is through the numerical solution of the sine-Gordon equation. Of major importance is the concept of the trapped or spontaneous flux and its influence on observable quantities such as the critical current and the critical magnetic field.

The objective of the first chapter is bilateral. Firstly, it serves as an introduction to the basic theories developed in superconductivity (i.e. BCS and Ginzburg-Landau) and it introduces the reader to the concepts and the language (e.g. order parameter). Secondly a comparison is made between conventional s-wave superconductors and unconventional high temperature cuprate superconductors. Emphasis is given in the experimental methods and theoretical techniques used to probe the symmetry of the order parameter. The Josephson effect is discussed in detail. Some of these techniques are analyzed extensively in the next chapters (i.e. tricrystal junctions, corner junction).

The second chapter is devoted to the static properties of Josephson junction made of conventional s-wave superconductors. We derive the basic Josephson relations and the sine-Gordon equation which is used for the study of the static properties in long Josephson junction i.e. critical currents, magnetic field, length of the junction. Both numerical and analytical (in terms of elliptic functions) approaches are used to study the stability of the solutions. The motivation of this study is also to compare properties of the junction made of conventional s-wave superconductors with the corresponding in junctions made of anisotropic superconductors and the ones with inhomogeneities, which are actually the topic of the next chapters. This chapter serves as a prototype to test the program used, verifying the well known properties of conventional superconductors and comparing with the new results concerning the high T_c superconductors.

In the third chapter, the static properties of a junction containing macroscopic inhomogeneities are derived in terms of the position of the defect, its strength and the external field. Simple arguments are derived that could help the defect characterization and could serve as a tool to study the properties of trapped flux in Josephson junctions or weak links. The last one is very important since the junction made of unconventional superconductors also has spontaneous flux arising from the order parameter symmetry.

In the fourth chapter we introduce Josephson junctions made of superconductors with anisotropic pairing symmetry e.g. $d_{x^2-y^2}$ or $d_{x^2-y^2}+is$. We use the tricrystal junction model - presented in the introduction - to describe the fractional vortex and antivortex that spontaneously appears near the junction center, due to the order parameter symmetry. We are particularly interested in long Josephson junctions since the large length is a prerequisite for the development of the vortex in the junction.

The fifth chapter is devoted in the discussions of three parameters that could modulate the critical current and the spontaneous flux in the corner junction model i.e. junction orientation, magnitude of the order parameter and magnetic field. The pairing symmetries that we examine are $d_{x^2-y^2}+is$ and $d_{x^2-y^2}+id_{xy}$. A theoretical experiment is proposed to distinguish them. The question is crucial since although the $d_{x^2-y^2}$-wave pairing symmetry has been established as the pairing symmetry in the bulk of the high T_c superconductors, near the surface the question has not yet been satisfactorily answered. Theoretical work as well as experimental data are needed to unsolve the puzzle and give a direct answer that could help determining the mechanism responsible for the high T_c superconductivity. Some final remarks and directions for future experiments are reported in the last chapter.

Summary in Greek

Κίνητρο της διατριβής είναι η παρουσίαση των μεθόδων για τον έλεγχο της συμμετρίας της παραμέτρου τάξης σε υπεραγωγούς υψηλής θερμοκρασίας μετάβασης, που εξαρτώνται από την φάση, δηλαδή έχουν άμεση σχέση με το φαινόμενο Josephson. Η προσέγγιση που έχει χρησιμοποιηθεί βασίζεται σε αριθμητική λύση της εξίσωσης sine-Gordon. Μια έννοια που έχει μεγάλη σημασία είναι αυτή της μαγνητικής ροής που έχει εγκλωβιστεί στην επαφή λόγω ανομοιογένειας της κρίσιμης πυκνότητας ρεύματος ή λόγω συμμετρίας της παραμέτρου τάξης, και η επίδραση που έχει αυτή η ροή σε πειραματικά μετρήσιμες ποσότητες όπως το κρίσιμο ρεύμα ή το κρίσιμο μαγνητικό πεδίο.

Στο κεφάλαιο ένα εισάγουμε τις βασικές θεωρίες που έχουν αναπτυχθεί για την ερμηνεία του φαινομένου της υπεραγωγιμότητας δηλαδή την BCS και την Ginzburg-Landau και επίσης διάφορες έννοιες (π.χ. παράμετρος τάξης) και την γλώσσα. Επίσης γίνεται μια σύγκριση μεταξύ s συμμετρίας υπεραγωγών και ανισοτροπικών υψηλής θερμοκρασίας μετάβασης. Ιδιαίτερη έμφαση δίνεται στις πειραματικές μεθόδους και στις αριθμητικές τεχνικές για να διακρίνουμε την συμμετρία της παραμέτρου τάξης. Γίνεται διάκριση ανάμεσα σε τεχνικές που είναι ευαίσθητες στην φάση και σε τεχνικές που δεν εξαρτώνται από αυτήν. Το φαινόμενο Josephson παρουσιάζεται ιδιαίτερα. Μερικές από τις τεχνικές που είναι ευαίσθητες στην φάση της παραμέτρου τάξης αναλύονται εκτενέστερα σε επόμενα κεφάλαια.

Στο κεφάλαιο δύο παρουσιάζουμε τις δυνατές λύσεις σε μια επαφή Josephson με εξωτερικό ρεύμα και μαγνητικό πεδίο σε γεωμετρία επιμήκη και επικάλυψης και εξετάζουμε την σταθερότητα των λύσεων. Ακολουθούμε τις διακλαδώσεις των νέων λύσεων καθώς αυξάνουμε το μήκος της επαφής. Οι αναλυτικές λύσεις εκφράζονται συναρτήσει ελλειπτικών συναρτήσεων και είναι σε συμφωνία με τις αριθμητικές λύσεις εξηγώντας τα έντονα φαινόμενα υστέρησης που παρατηρούνται στον υπολογισμό του μεγίστου ρεύματος. Αυτό προτείνει μια διαφορετική προσέγγιση στο πείραμα που βασίζεται στην χρήση, αντί του εξωτερικού μαγνητικού πεδίου, του υπολοίπου της ελλειπτικής συνάρτησης ή μιας σχετικής ποσότητας που είναι η ολική μαγνητική ροή για να αποφευχθεί η υστέρηση και να αναδιπλωθούν οι επικαλυπτόμενες $I_c(H)$ καμπύλες.

Στο κεφάλαιο τρία υπολογίζουμε το μέγιστο ρεύμα σε επαφή Josephson με μακροσκοπικές ατέλειες για διαφορετικές κρίσιμες πυκνότητες ρεύματος σαν συνάρτηση του μαγνητικού πεδίου. Επίσης εξετάζουμε την εξέλιξη των διαφόρων κλάδων με την θέση της ατέλειας και το εξωτερικό μαγνητικό πεδίο. Μελετούμε τη σταθερότητα των λύσεων και εξάγουμε απλά συμπεράσματα που μπορούν να βοηθήσουν στο χαρακτηρισμό των ατελειών. Στις περισσότερες περιπτώσεις παρατηρούμε ένα μέγιστο και ένα ελάχιστο ρεύμα.

Στο κεφάλαιο τέσσερα υπολογίζουμε το ρεύμα συναρτήσει της μαγνητικής ροής και την αυθόρμητη ροή σε επαφές Josephson υπεραγωγών με $d_{x^2-y^2}+is$ συμμετρία της παραμέτρου τάξης, για διαφορετικά μήκη επαφής και σχετικές φάσεις ανάμεσα στις δύο συνιστώσες της παραμέτρου τάξης. Εξετάζουμε την σταθερότητα του κλασματικού φλαξονίου και αντιφλαξονίου καθώς και την εξέλιξη τους με το μήκος και την σχετική διαφορά φάσης ανάμεσα στην $d_{x^2-y^2}$ και την s συνιστώσα. Ασυμμετρία στο $I(\Phi)$ διάγραμμα υπάρχει για μήκη μέχρι και $L = 10\lambda_J$.

Στο κεφάλαιο πέντε η θεωρία Ginzburg-Landau χρησιμοποιείται για τον υπολογισμό των πιθανών αυθόρμητων φλαξονίων που μπορεί να υπάρχουν σε επαφή Josephson μεταξύ $d_{x^2-y^2}+i\chi$ (όπου $\chi = s$ ή $\chi = d_{xy}$) συμμετρίας της παραμέτρου τάξης υπεραγωγούς και s συμμετρίας υπεραγωγούς, σε γεωμετρία γωνίας. Μελετούμε την μαγνητική ροή και την μεταβολή του κρίσιμου ρεύματος με την γωνία του κρυσταλογραφικού a-άξονα και της μιας πλευράς της επαφής, του μέτρου της παραμέτρου τάξης και του μαγνητικού πεδίου H. Το κρίσιμο ρεύμα σα συνάρτηση της μαγνητικής ροής είναι συμμετρικό (ασυμμετρικό) για $\chi = xy(s)$ όταν η γωνία είναι τέτοια ώστε οι λοβοί της $d_{x^2-y^2}$ συνιστώσας της παραμέτρου τάξης δείχνουν προς τις δύο επαφές που είναι σε κάθετη γωνία ως προς την γεωμετρία γωνίας. Το συμπέρασμα είναι ότι μια μέτρηση της $I_c(\Phi)$ σχέσης ίσως διακρίνει ποιά συμμετρία $d_{x^2-y^2}+is$ ή $d_{x^2-y^2}+id_{xy}$ έχει η παράμετρος τάξης. Στο κεφάλαιο έξι καταγράφουμε τα τελικά συμπεράσματα και δίνουμε κατευθύνσεις για μελλοντικά πειράματα.

Chapter 1

Introduction

1.1 High T_c cuprates

In 1911 Kemerlingh Onnes discovered superconductivity just three years after he first liquefied helium. He found that the electrical resistance of some metals disappeared at a critical temperature T_c of the order of a few Kelvin. In 1986 Bednorz and Muller discovered superconductivity in the copper oxide $La_{2-x}Sr_xCuO_4$, where x denotes the doping level [16]. The transition temperature varies with the concentration of strontium and reaches a maximum of $38K$ when $x = 0.15$. A year later groups from US, Japan, and China reported the discovery of $Y_1Ba_2Cu_3O_{7-\delta}$ or 123 a material with $T_c = 90K$. The basic structure of this new class of materials consists of layers of CuO_2 with elements of yttrium and barium or lanthanum and strontium between the layers. In addition the 123 compounds contain CuO "chains", which are thought to serve as reservoirs to control the electron density in the planes. The basic structure of $Y_1Ba_2Cu_3O_{7-\delta}$ is seen in Fig. 1.1. When $x = 0$ the material La_2SrCuO_4 is an antiferromagnet insulator, but when x increases i.e. Sr with only two available electrons replaces some of the La with three available electrons in a process called doping additional holes which are charge carriers are introduced into the copper-oxide layers and make the material conducting and under certain conditions superconducting. The same doping process occurs in 123 when Ca^{2+} replaces Y^{3+}.

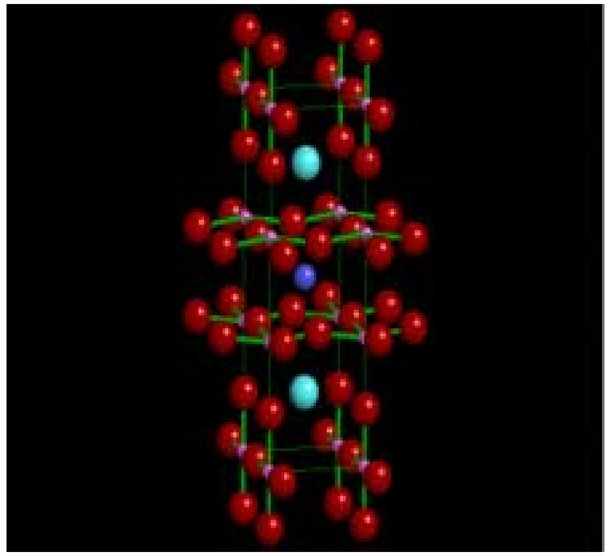

Figure 1.1: Plot of the basic structure of $Y_1Ba_2Cu_3O_{7-\delta}$. Y, Ca:dark blue, Ba: light blue, O: red, Cu:pink

1.2 The phase diagram

The phase diagram of the cuprates seen in Fig. 1.2 consists of the antiferromagnetic region at zero doping i.e. the electron spins on neighboring copper ions point in opposite direction. When doping increases we enter the pseudogap phase which is characterized by the presence of gap and not superconductivity and is not well understood. The most possible scenario is that the Cooper pairs are formed above T_c, at a temperature T_p but due to the small number of charge carriers there is no phase coherence and they condense at T_c [31]. As the doping is further increasing we enter the superconducting region where the resistivity is zero and a gap is present in the single particle excitation spectrum. At high doping level there exists the Fermi-liquid region where the key concept is the quasiparticle and the non Fermi liquid which is characterized by unusual power laws in all of the transport properties as a function of temperature. For a review see [73].

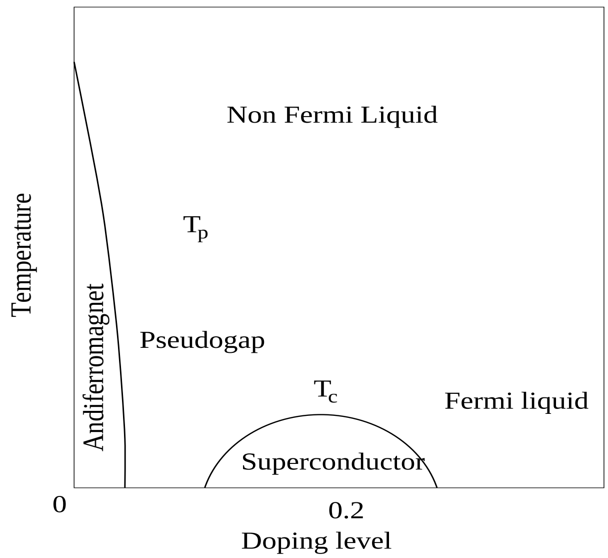

Figure 1.2: Plot of temperature versus the doping level in cuprate superconductors

1.3 BCS theory and unconventional pairing

In 1956 Cooper proved that the normal Fermi sea is unstable in the presence of two electrons interacting via an attractive potential. In low temperature superconductors the crystal lattice vibrations allow the electrons to overcome their mutual electrostatic repulsion and to form Cooper pairs, occupying states with equal and opposite momentum and spin. In 1957 Bardeen, Cooper and Schrieffer studied a reduced Hamiltonian [13, 96]

$$H_{red} = \sum_{ks} \epsilon_k n_{ks} + \sum_{kk'} V_{kk'} b_k^\dagger b_k, \tag{1.1}$$

where $b_k^\dagger$ creates an electron pair in $(k_\uparrow, -k_\downarrow)$ and ϵ_k is the normal state quasiparticle energy. The particle number operator n_{ks} is defined by $n_{ks} = c_{ks}^\dagger c_{ks}$, which has an eigenvalue of unity when operating on an occupied state and gives zero when operating on an empty state, and $c_{ks}^\dagger(c_{ks})$ is the electron creation (annihilation) operator. They proposed a variational wave function of the form

$$\Phi = \prod_k (u_k + v_k b_k^\dagger)|0>, \tag{1.2}$$

with $u_k^2 + v_k^2 = 1$. This form implies that the probability of the pair $(k_\uparrow, -k_\downarrow)$ being occupied is v_k^2, while the probability that it is unoccupied is $u_k^2 = 1 - v_k^2$. The minimization of the energy with respect to v_k leads to the self consistent solution for the gap function

$$\Delta_k = -\sum_{k'} V_{kk'} \frac{\Delta_{k'}}{2E_{k'}}, \tag{1.3}$$

with

$$v_k^2 = \frac{1}{2}(1 - \frac{\epsilon_k}{E_k}), \tag{1.4}$$

and

$$E_k = \sqrt{\epsilon_k^2 + \Delta_k^2}. \tag{1.5}$$

One of the predictions of the BCS theory is the existence of the energy gap $\Delta(T)$ between the ground state and the quasiparticle excitations of the system. A minimum energy $E_g = 2\Delta(T)$ should be required to break a pair, and create two particle excitations. At zero temperature

$$E_g(0) = 2\Delta(0) = 3.52 k_B T_c. \tag{1.6}$$

The spatial extension of the Cooper pairs or the coherence length is defined by

$$\xi = \frac{\hbar v_F}{\pi \Delta(0)}, \tag{1.7}$$

where v_F is the Fermi velocity. In s-wave superconductors ξ is quit large of the order of $10^3 - 10^4 A^\circ$.

In s-wave superconductors Δ_k is independent on k. This means that the Cooper pairs have zero orbital angular momentum. In anisotropic material like YBCO Δ_k is a function of k and has the same symmetry as the crystal lattice. The physical mechanism for the high-T_c is not yet clear. It is clear that a two electron pairing is involved but the nature of the pairing remains controversial, although there is evidence indicating that the Cooper pairs have $d_{x^2-y^2}$-wave symmetry. Possibly the mechanism is purely electronic and is based on the exchange of antiferromagnetic spin fluctuations among quasiparticles. Furthermore in cuprates due to the large value of the gap and the low Fermi velocity stemming from the low electron density, the Cooper pairs have little overlap and the coherence length ξ is small of the order of $10A$.

1.4 Order parameter and symmetry breaking in superconductors

BCS microscopic theory is valid when the gap is constant in space. In situations where the order parameter is inhomogeneous e.g. in type II superconductors, a more macroscopic theory is needed i.e. the Ginzburg-Landau theory (GL). In the GL theory the superconducting state is described by a complex order parameter

$$\Psi(\mathbf{r}) = |\Psi(\mathbf{r})|e^{\phi(\mathbf{r})}, \tag{1.8}$$

where $|\Psi(\mathbf{r})|$ is the modulus and $\phi(\mathbf{r})$ is the phase. The superfluid density is given by

$$\rho_s(\mathbf{r}) = |\Psi(\mathbf{r})|^2. \tag{1.9}$$

If $\Psi(\mathbf{r})$ is small, the Free energy density can be expanded in a series of the form

$$f_s = f_n + a|\Psi(\mathbf{r})|^2 + \frac{1}{2}\beta|\Psi(\mathbf{r})|^4 + \frac{1}{2m^*}|(\frac{\hbar}{i}\nabla - \frac{e^*}{c}\mathbf{A})\Psi(\mathbf{r})|^2 + h^2/8\pi. \tag{1.10}$$

In the absence of field and gradients only the first two terms are retained. β must be positive. For $a > 0$ the minimum of the Free energy occurs at $|\Psi|^2 = 0$ (normal state) while for $a < 0$ the minimum occurs for $|\Psi|^2 = -a/\beta$. Then $f_s - f_n = -a^2/2\beta$. A minimization of the volume integral of Eq. (1.10) with respect to variations in $\Psi(\mathbf{r})$ and $A(\mathbf{r})$ leads to the GL equations

$$a\Psi(\mathbf{r}) + \frac{1}{2}\beta|\Psi(\mathbf{r})|^2\Psi(\mathbf{r}) + \frac{1}{2m^*}(\frac{\hbar}{i}\nabla - \frac{e^*}{c}\mathbf{A})^2\Psi(\mathbf{r}) = 0, \tag{1.11}$$

$$\mathbf{J} = \frac{e^*}{m^*}|\Psi(\mathbf{r})|^2(\hbar\nabla\phi - \frac{e^*}{c}\mathbf{A}) = e^*|\Psi(\mathbf{r})|^2\mathbf{v_s}. \tag{1.12}$$

Equation (1.11) has the form of the Schroedinger equation for particles with energy eigenvalue $-a$ apart from the nonlinear term. This term acts like a repulsive potential of $\Psi(\mathbf{r})$ on itself tending to favor wavefunctions $\Psi(r)$ which are spread out as uniformly as possible in space. The current expression (1.12) has exactly the form of the usual quantum mechanical expression for particles of mass m^*, charge e^* and wave function $\Psi(\mathbf{r})$. We define

$$\xi(T) = \frac{\hbar^2}{2m^*|a(T)|}, \tag{1.13}$$

as the characteristic length over-which a small disturbance of $\Psi(\mathbf{r})$ from $\Psi_\infty(\mathbf{r})$ will decay to zero. Near T_c $\xi(T)$ diverges as $(T_c - T)^{-1/2}$ since a vanishes as $(T - T_c)$. Also the relation

$$\kappa = \frac{\lambda_{eff}(T)}{\xi(T)}, \tag{1.14}$$

where $\lambda_{eff}(T)$ is the effective penetration depth defines the GL parameter. In pure s-wave superconductors $\kappa << 1$ since $\lambda \approx 500A^\circ$, and $\xi \approx 3000A^\circ$, while in dirty superconductors or in the high T_c superconductors κ may be much greater than 1. The value $\kappa = 1/\sqrt{2}$ separates superconductors of type I and II. Abrikosov showed that for materials with $\kappa > 1/\sqrt{2}$, (called type II superconductors), instead of a discontinuous breakdown of superconductivity at the critical field H_c, there was a continuous increase in flux penetration starting at a lower critical field H_{c1} and reaching $B = H$ at an upper critical field $H_{c2} > H_{c1}$ [3]. In the mixed state between H_{c1} and H_{c2} the flux penetrates forming a triangular array of flux tubes as confirmed by scanning tunneling microscope measurements for the superconductor $NbSe_2$[44]. H_{c2} is equal to $10T$ for s-wave superconductors, while H_{c2} is approximately $100T$ for cuprates.

In 1959 Gor'kov showed that the GL theory is a limiting form of the microscopic BCS theory, valid near T_c where $\Psi(\mathbf{r}) \sim \Delta$ [38].

The non-zero expectation value of the two-particle density matrix

$$\rho(\mathbf{r}, \mathbf{r}') =< \Psi_\downarrow^\dagger(\mathbf{r})\Psi_\uparrow^\dagger(\mathbf{r}) >< \Psi_\downarrow(\mathbf{r}')\Psi_\uparrow(\mathbf{r}') >, \tag{1.15}$$

explains the existence of certain particle correlations. The order parameter is a measure of the amount of symmetry breaking in the ordered

Table 1.1: Even parity irreducible representations of D_{4h} along with examples of basis functions for Δ_k

Irreducible representations	Basis functions for Δ_k
A_{1g}	$1, \cos k_x + \cos k_y$
A_{2g}	$\sin k_x \sin k_y(\cos k_x - \cos k_y)$
B_{1g}	$(\cos k_x - \cos k_y)$
B_{2g}	$\sin k_x \sin k_y$
$E_g(1,i)$	$\sin k_x \sin k_z$, $\sin k_y \sin k_z$

state. The symmetry group H describing the superconducting state must be a subgroup of the full symmetry group G in the normal state

$$G = \begin{array}{c} X \times R \times U(1) \times T \text{ for } T > T_c \\ H \text{ for } T < T_c \end{array} , \tag{1.16}$$

where X is the symmetry group of the crystal lattice, R is the symmetry group of the spin rotation, $U(1)$ is the one-dimensional global gauge symmetry, and T is the time reversal symmetry. In BCS superconductors $U(1)$ is broken due to the existence of long range order in the superconducting state. In unconventional superconductors one or more symmetries are broken at T_c.

1.5 Possible pairing states

In cuprates the physics occurs in the CuO_2 planes while the intermediate layers act as charge reservoirs to exchange electrons with the planes. So the symmetry of the order parameter should be related to the lattice structure of the planes which is square like. In a tetragonal lattice with D_{4h} symmetry there exist five even parity irreducible representations, since the pairing state is singlet. Their basis functions correspond to candidates gap functions for high T_c cuprates as listed in table 1.1 [83]. The k-space representation of the allowed basis functions for the D_{4h} symmetry is seen in Fig. 1.3. The d-wave $\Delta_{d_{x^2-y^2}}(k) = \Delta_0(\cos k_x - \cos k_y)$ is the basis state for B_{1g}, while $\Delta_{d_{xy}}(k) = \Delta_0(\sin k_x \sin k_y)$ is the basis state for B_{2g}

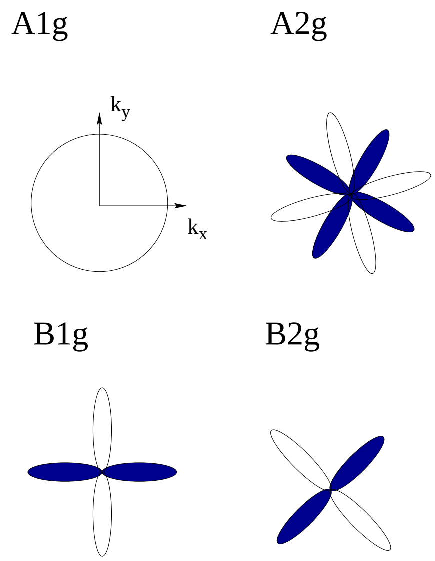

Figure 1.3: Schematic representation of $\Delta(k)$ in the Brillouin zone, for the allowed symmetry basis functions for the D_{4h} symmetry appropriate for the CuO_2 planes in the high-T_c superconductors.

The cuprate superconductors have a slight orthorhombic distortion and the point group of interest is of lower symmetry orthorhombic D_{2h} where some degrees of freedom like 90° rotation and $x = \pm y$ reflection are removed. In D_{2h} group the $d_{x^2-y^2}$ also belongs in the A_{1g} and based on symmetry arguments only, it can not be distinguished from the s-wave or the extended s-wave. So any combination of s, extended s, $d_{x^2-y^2}$ is possible, including the state $d_{x^2-y^2} + is$ with gap function $\Delta = \Delta_0(\epsilon(\cos k_x - \cos k_y) + i(1-\epsilon))$ and $d_{x^2-y^2} + id_{xy}$ with gap function $\Delta = \Delta_0((1-\epsilon)(\cos k_x - \cos k_y) + i\epsilon 2 \sin k_x \sin k_y)$ where the order parameter is complex breaking the time reversal symmetry.

1.6 How would we know the pairing symmetry

The problem to identify the pairing symmetry in cuprates has not found a satisfactory solution yet. The order parameter can not be probed directly, i.e. it is not a macroscopic observable. Hence one tries to infer the type of the order parameter from its influence on various thermodynamic quantities and transport properties. A number of experiments have been proposed that allow to distinguish between the possible candidate pairing states. In a spin singlet state the spin susceptibility is suppressed in the superconducting state. The Knight shift goes smoothly to zero at $T = 0$ and is consistent with singlet pairing state, as in conventional s-wave superconductors [95]. In s-wave superconductors where the magnitude of the gap does not vanish, the density of states and the various thermodynamic and transport properties decrease exponentially. If the gap has nodes as in $d_{x^2-y^2}$-wave then $N(\epsilon)$ varies linearly with ϵ and the various quantities vary as power laws.

1.6.1 Non-Phase Sensitive Techniques

Penetration depth

The penetration depth $\lambda(T)$ in the usual BCS theory is given by

$$\rho_s = (\frac{\lambda(0)}{\lambda(T)})^2 = 1 - 2\beta \int_0^\infty d\epsilon \frac{N(\epsilon)}{N(0)} f(\epsilon)(1 - f(\epsilon)), \tag{1.17}$$

where $\beta = 1/k_B T$, $f(\epsilon)$ is the Fermi function

$$f(\epsilon) = \frac{1}{1 + e^{\beta\epsilon}}. \tag{1.18}$$

For the s-wave state the BCS form of the density of states is assumed

$$N(\epsilon)/N_0 = Re \frac{\epsilon}{\sqrt{\epsilon^2 - \Delta^2}}, \tag{1.19}$$

while for the d-wave

$$N(\epsilon)/N_0 = \epsilon/\Delta_0. \tag{1.20}$$

For s-wave the result for the penetration depth is

$$\frac{\lambda(T) - \lambda(0)}{\lambda(0)} = \sqrt{\frac{2\pi\Delta}{T}} e^{-\Delta_0/k_B T}, \tag{1.21}$$

while for $d_{x^2-y^2}$-wave the result is

$$\frac{\lambda(T)-\lambda(0)}{\lambda(0)} = ln(2)\frac{k_B T}{\Delta_0}, \tag{1.22}$$

where Δ_0 is the zero temperature value of the gap. So in a $d_{x^2-y^2}$-wave superconductor the penetration depth varies linearly with T, while in an s-wave superconductor it varies exponential with T. This theoretical prediction is confirmed experimentally for the YBCO [41]. The value of λ is of the order of $(10^3 - 10^4 A^\circ)$ in cuprates, while in low T_c superconductors, $\lambda \approx 500A^\circ$, due to the smaller value of the phenomenological parameter ρ_s in cuprates. At low T the linear variation of $\lambda(T)$ is also consistent with an extended s-wave symmetry and hence the penetration depth measurements can not distinguish between these pairing states.

NMR measurements

In conventional s-wave superconductors the nuclear relaxation rate $1/T_1$ shows a peak just below T_c before an exponential drop-off to zero with the freeze out of quasiparticles at lower temperatures [43]. This is explained with the BCS theory with the assumption of the coherence factors. The absence of the Hebel-Slichter peak in the nuclear relaxation rate $1/T_1$ for both Cu and O in in-plane sites observed in NMR studies in high T_c materials suggests a breakdown or a modification of the BCS coherence factors. Also at low temperature the absence of exponential freeze out of $1/T_1$ as replaced by a power law variation suggests a $d_{x^2-y^2}$-wave pairing state. A convenient review of this field was given by Pennington and Slichter in [76].

ARPES

Angle resolved photoemission spectroscopy (ARPES) data provide information about the position of the gap nodes in momentum space. The developments of this technique for studying pairing symmetry in the cuprates has been hampered by its sensitivity to surface conditions and by its relative poor energy resolution comparable to the size of the energy gap. ARPES data for $Bi_2Sr_2CaCu_2O_{8+x}$, (B2212) seen in

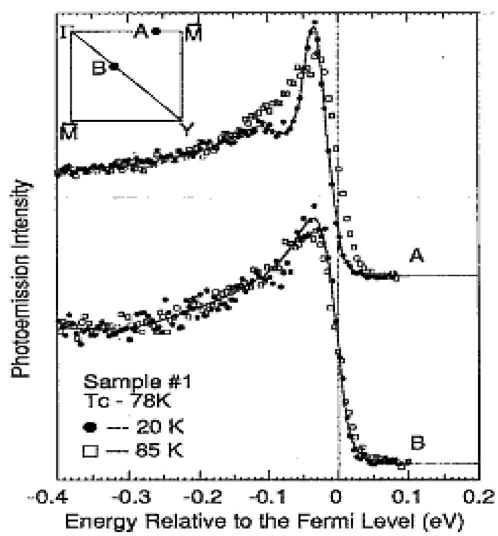

Figure 1.4: High resolution photoemission spectra from Ref. [81] recorded at locations A and B, of sample 1 as illustrated in the inset. The spectra at B were measured before those at A. The spectral changes above and below T_c are caused by the opening of the superconducting gap. The change at A is quite visible, yielding a larger gap. The change at B is hardly visible, suggesting a very small or null gap.

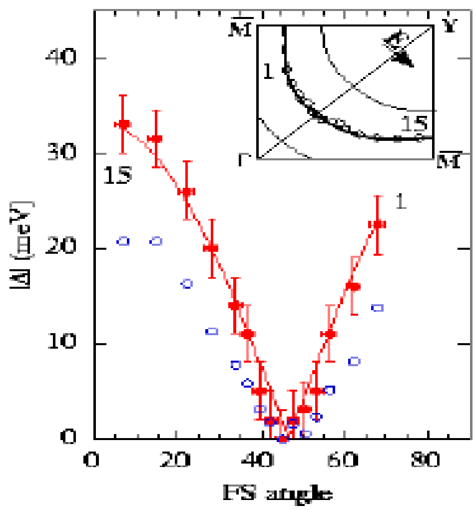

Figure 1.5: Energy gap in Bi-2212, measured with ARPES as a function of angle on the Fermi surface, solid curve which fits to the data using a d-wave order parameter. Inset indicates the locations of the data points in the Brillouin zone. Data are from [30]

Fig. 1.4, above and below T_c for Fermi wave vector along the direction parallel to the a or b crystallographic axes shows a shift in the leading edge of the spectral weight indicating a gap. [81] The absence of shift along the diagonal direction ΓY (the diagonal direction between the a and b) indicates a large gap anisotropy consistent with the $d_{x^2-y^2}$-wave gap. Also the energy gap measured with ARPES, as a function of the angle on the Fermi surface seen in Fig 1.5 is consistent with a $d_{x^2-y^2}$-wave model. These results rule out the B_{2g}, A_{2g}, and A_{1g} pairing states. However these experiments probe the magnitude of the gap and hence cannot discriminate between a highly anisotropic s-wave and a $d_{x^2-y^2}$-wave gap.

1.6.2 Half-integer flux quantization

Josephson tunneling

Josephson first predicted in 1962 [48] that it is possible for Cooper pairs to flow through an insulating barrier between two superconductors. If two superconductors (i, j) are brought into contact with an oxide layer between them, their order parameters n_i and n_j are no longer independent. When there is a phase difference between them supercurrent will flow. This is the Josephson effect. The Josephson current is

$$I = I_0 i(n_i^* n_j - n_i n_j^*) = I_c^{ij} \sin \phi_{ij}, \tag{1.23}$$

where $\phi_{ij} = \phi_j - \phi_i$, ϕ_i, ϕ_j are the corresponding phases and

$$I_c^{ij} = 2I_0 |n_i||n_j|, \tag{1.24}$$

is the Josephson critical current. Under a finite dc voltage V the time dependence of ϕ is given by the Josephson relation

$$d\phi/dt = 2eV/\hbar, \tag{1.25}$$

and the junction will carry an ac supercurrent at frequency $2eV/\hbar$. It can be detected by its resonance frequency with a superimposed ac field (Shapiro steps). The Josephson effect was verified by experiment in 1963 [5]. First the Josephson effect can be used to determine the parity of the superconductor, since it is found that the Josephson current vanishes up to second order in tunnel junctions between singlet and triplet superconductors [75]. The Josephson tunneling also includes other weak-link structures such us Superconductor / Normal metal /Superconductor with a different current phase relation.

The Josephson effect provides a powerful means to study the phase of the superconducting order parameter. In Josephson junctions between d-wave superconductors the critical current is given by

$$I_c^{ij} = A_s \cos(2\theta_i)\cos(2\theta_j), \tag{1.26}$$

and θ_i, θ_j are the angles of the crystallographic axes with respect to the interface [84]. So depending on the orientation angles θ_i, θ_j, the Josephson critical current can be negative. A negative critical current I_c^{ij} can be thought of as a phase shift of π at the Josephson interface. Also such phase shift can originate from the spin flip scattering by magnetic impurities at the interface. [19]

Flux quantization in a superconducting ring

The single valuedness of the phase ϕ requires that $\phi(r)$ return to itself (modulo 2π) on going once around a superconducting ring on any path. The magnetic flux in a superconducting ring made from conventional s-wave superconductors is quantized in integer multiplies of the flux quantum (zero ring). A superconducting ring containing an odd number of π shifts (π ring) will generate spontaneous flux with half of the conventional flux quantum $\Phi_0 = hc/2e = 2.07 \times 10^{-7} G - cm^2$. The flux quantization condition reads

$$\Phi_a + I_s L + \frac{\Phi_0}{2\pi}\sum_{ij}\phi_{ij} = n\Phi_0, \tag{1.27}$$

where the supercurrent is given by

$$I_s = I_c^{ij}(\theta_i, \theta_j)\sin\phi_{ij}, \tag{1.28}$$

where L is the self-inductance of the ring, Φ_a is the externally applied flux and ϕ_{ij} is the phase difference between the superconducting electrodes i, j which is defined in the previous subsection. $I_c^{ij}(\theta_i, \theta_j)$ is the critical current of the junction between superconducting electrodes i, j

and θ_i, θ_j are the corresponding angles of the crystallographic axis with respect to the junction interface. The ground state of such a ring is obtained from the minimization of the junction's free energy with respect to the flux Φ and is achieved only when $\Phi = (n + 1/2)\Phi_0$, for $n\Phi_0 < \Phi < (n+1)\Phi_0$.

Paramagnetic Meissner effect

The presence of the spontaneous flux has been proposed as an explanation of the paramagnetic Meissner effect observed in Josephson junction circuits [84]. If $2\pi L I_c^{ij}/\Phi_0 < 1$, a zero ring has an induced flux with opposite sign as the applied flux, while in a π ring the induced flux has the same sign as the applied flux (paramagnetic shielding).

1.6.3 Phase sensitive tests of the pairing symmetry

Squid interferometry

If YBCO is a $d_{x^2-y^2}$-wave superconductor, there should be a π phase shift between weak links on adjacent faces of the crystal. If the self-inductances are small, or if the self-inductances are symmetric then the SQUID critical current versus the magnetic field is symmetric with a maximum at $\Phi = 0$ for a zero-ring and a minimum for a π ring. This has been used by Wollman et. al. [103] to probe the $d_{x^2-y^2}$-wave pairing state in cuprates. However the interpretation of these experiments was not easy due to a number of complicating factors such as the twinning effects, the linear interpolation of the I_c vs Φ curves, the flux trapping, and the sample geometry.

Also high-T_c SQUIDS made from 45° asymmetric biepitaxial grain boundaries studied by Mannhard et. al. [65] shows anomalous I_c vs H pattern and can be interpreted as arising from a $d_{x^2-y^2}$-wave order parameter.

Corner junction experiments

The symmetry of the gap can be probed by measuring the magnetic flux modulation of the critical current for a corner junction. We consider

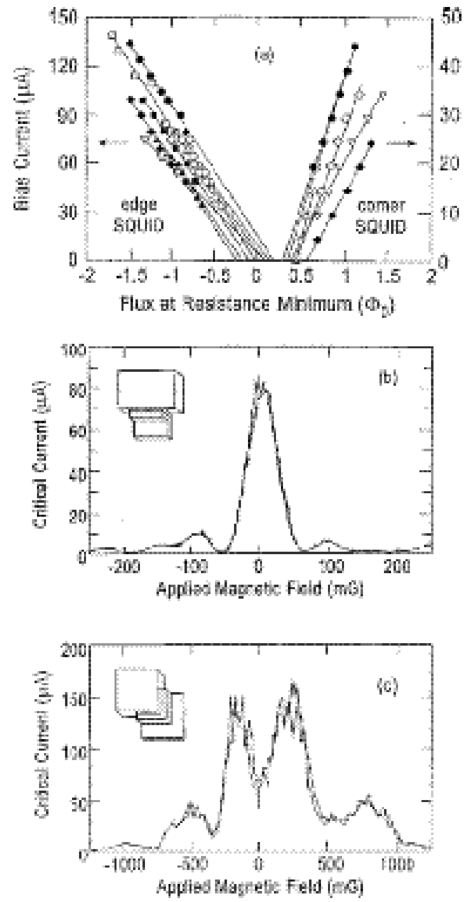

Figure 1.6: Summary of the experimental results of Wollman et. al [103] (a) Bias current for a corner SQUID and an edge SQUID vs flux. (b) Critical current vs applied magnetic field for an edge junction (c) The same as in b but for a corner junction.

the Josephson junction between YBCO and Pb where the a and b faces of YBCO are at right angles to the junction edges [103]. If YBCO is a $d_{x^2-y^2}$-wave superconductor, the Josephson critical current is equal to $I_c \approx \cos(2\theta)$, where θ is the angle of the crystal axes and the junction interface. The Josephson critical current changes sign as we move from one edge of the junction to the other introducing an intrinsic phase shift of π to the Josephson coupling. In the $d_{x^2-y^2}$-wave case the magnetic interference pattern is

$$I_c(\Phi) = 2I_0 \sin^2(\pi\Phi/2\Phi_0)/(|\pi\Phi/\Phi_0|), \tag{1.29}$$

and has a dip at $\Phi = 0$, $\Phi = HA_{eff}$ where H is the external field. A_{eff} is given by the product of the length perpendicular to the field times the quantity $d + \lambda_1 + \lambda_2$ where d is the thickness of the junction and λ_1, λ_2 are the London penetration depths of the two bulk superconductors.

The usual Fraunhofer form of the pure s-wave superconductor junction or the edge junction between a $d_{x^2-y^2}$-wave superconductor and an s-wave superconductor is of the form

$$I_c(\Phi) = 2I_0|\sin(\pi\Phi/\Phi_0)/(\pi\Phi/\Phi_0)|, \tag{1.30}$$

and shows a maximum at $\Phi = 0$. The proof of Eq. (1.30) is given in chapter 2. The experimental result of Wollman et. al. [103] for the critical current vs magnetic field, presented in Fig. 1.6(b),(c), for the edge (corner) junction with a maximum(minimum) at $H = 0$ is consistent with the assumption of $d_{x^2-y^2}$-wave pairing symmetry in cuprate superconductors.

Also Miller, Ying et. al. [49] used frustrated thin film tricrystal samples to probe the pairing symmetry in YBCO. They measured the critical current versus the magnetic field and found a "dip" at zero field for the short junction limit as expected for $d_{x^2-y^2}$-wave superconductors.

Tricrystal ring experiments

In tricrystal ring experiments grain boundary Josephson junctions are formed between three YBCO films, as shown in Fig. 1.7 . [97] The YBCO films grows with their a and b axis oriented along the (100) and

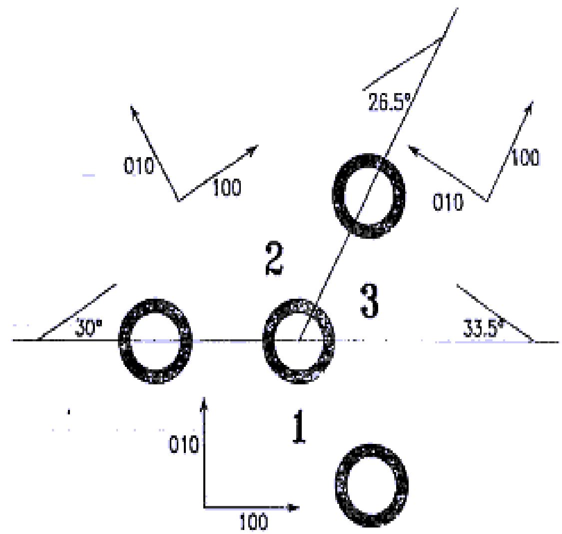

Figure 1.7: Schematic diagram for the tricrystal (100) $SrTiO_3$ substrate, with four epitaxial YBCO rings, from Ref. [97].

(010) axis of the $SrTiO_3$ substrate. The orientation of the a, b axis in each film is such that in the grain boundary between 1 and 3 there is an internal phase shift of π. Then rings are patterned such that one ring has no grain boundaries, one has one grain boundary, and the ring in the center has three grain boundaries. Tuei et. al. [97] using a SQUID measured the magnetic flux and found that the three outer rings have no magnetic flux trapped in them while he observed half integer flux for the three junction ring which is consistent with the $d_{x^2-y^2}$-wave pairing symmetry. We conclude that as discussed in chapter 4 for a similar geometry where between grains $2, 3$ we assume that a twin boundary exists, the magnetic flux quantization on a tricrystal junction experiment give information about the pairing state and also on a subdominant order parameter.

1.6.4 Implications of the d-wave pairing symmetry

Time reversal symmetry broken states

For bulk properties the phase sensitive symmetry tests have ruled out time-reversal symmetry broken state (TRSB). However it is possible the TRSB state to appear wherever the order parameter varies spatially, e.g. near the surface, interfaces, impurities. Then the $d_{x^2-y^2}$-wave pairing state is unstable against the formation of a two component order parameter at low temperatures.

Phase sensitive experiments can be useful to discriminate between time reversal symmetry broken states as we will see in Chapter 5. The intrinsic shift a determines the minimum of the junction energy $E_{J,a}(\phi) \sim \cos(\phi - a)$. If we apply the time reversal operation $n_{i,j} \to n^{\star}_{i,j}$, then $\phi \to -\phi$ and $a \to -a$. For $a = 0, \pi$ the lowest energy is the same under time reversal operation apart from 2π multiplies, while for $a \neq 0, \pi$ the lowest energy state is not unique but changes under time reversal. The $a \neq 0, \pi$ case results only when a two component complex order parameter is considered, such as $d_{x^2-y^2} + is$ or $d_{x^2-y^2} + id_{xy}$. In this case the gap is nodeless. Also the deviations on the current-phase relation from the standard sinusoidal current-phase relation observed by 45°-missoriented YBCO grain boundary junctions at low temperatures is attributed to TRSB states. [46] Consequences are the fractional flux quanta observed near grain boundaries as opposed to the half flux quanta which indicate $d_{x^2-y^2}$-wave pairing. [51]

Tunneling experiments

The fundamental process in the tunneling experiments between normal metals and superconductors is Andreev reflection. In Andreev reflection process an electron incident in the barrier with an energy less than Δ_0 can not drain off into the superconductor. It is instead reflected as a hole and a Cooper pair is transfered in the superconductor. In the case of conventional s-wave superconductors a gaped region appears in the tunneling spectra. In anisotropic high T_c superconductors the transmitted quasiparticles feel different sign of the pair potential. This results in the formation of bound states. These Andreev bound states give rise to a peak in the quasiparticle density of states at the

Fermi energy and should result in a zero-bias conductance peak in the quasiparticle tunneling spectra of superconductor - normal metal tunnel junctions. [27] The presence of an imaginary component breaking the time reversal symmetry shifts the peak to the amplitude of the secondary component.

1.7 Pinning effect

In high T_c superconductors there are several types of defects. They include localized defects, such as departures from stoichiometry at the atomic scale, or more extended defects such as dislocations, grain boundaries, inclusions of second phases, twin planes etc.

The measurement of the maximum current vs the magnetic field of the material will give information on the spatial distribution of the defects, and would be useful to improve the properties of the material such as the critical current or the critical magnetic field, melting line. Information on the defect distribution can also be obtained from the $I-V$ characteristics where steps are introduced when the junction is irradiated with microwaves.

In chapter 3 we calculate the I_c vs H in a Josephson junction with spatial inhomogeneous Josephson defect critical current density and perform the linear stability analysis to study the influence of the inhomogeneity in the critical current and the magnetic field. Simple arguments are derived that could help the sample characterization. Due to fluxon trapping from the defect additional stable states are introduced in a large interval of the magnetic field and the critical current increases as compared to the perfect junction. This modified I_c vs H diagram as compared to the experimental one could help to extract information about the position of defects, the defect Josephson critical current density, and the type of defect, in order to improve the material properties.

Chapter 2

Stability analysis of static solutions in a Josephson junction

2.1 Introduction

In this chapter we describe the static properties of a pure s-wave superconductor Josephson junction by solving numerically the sine-Gordon equation. [14] We calculate the maximum tunneling current I_{max} as a function of the external field H, and compare the results with the existing experimental data. We also study both analytically in terms of elliptic functions and numerically the stability of the solutions.

The motivation of this study is

- to explain the hysteritic behavior seen in Josephson junctions.

- to express the static solutions in a way that will allow us to examine their stability and follow their evolution with length and the magnetic field H.

- To develop a numerical simulation in order to study more complicated problems like inhomogeneities, dynamics, π-junctions, and also the two-dimensional window Josephson junctions. Some of them are studied in the subsequent chapters.

The static and dynamic stability of fluxons has been analyzed using the sine-Gordon equation [20, 28, 34, 18] both theoretically and numerically, in case where no external current is applied. The numerical procedure we follow here is based on iteration methods and requires an initial guess that is close to the desired solution.

The rest of the chapter is organized as following. In section 2.2 we derive the basic Josephson equations. In section 2.3 we present the RCSJ model. In section 2.4 we present the effect of the magnetic field in the Josephson junction. In section 2.5 we present the special case of junctions with negligible screening. In section 2.6 we present the electrodynamics of the Josephson junction. In section 2.7 we discuss the $I-V$ characteristic of a Josephson junction. In section 2.8 we discuss a special solution of the sine-Gordon equation i.e. the soliton. In section 2.9 we present the inline boundary conditions, give the explicit analytical solutions using elliptic functions for the sine Gordon equation and sketch the stability analysis. In section 2.10 we outline the numerical procedure we follow. In section 2.11 we study the solutions in the particular case of zero magnetic field $H=0$, and in section 2.12 the analytic solutions for zero current $I=0$. We study both theoretically and numerically their stability in section 2.13 and we calculate the maximum tunneling current. In section 2.14 we briefly propose an experimental procedure which utilizes our numerical procedure. We summarize our results in the last section.

2.2 Basic Josephson relations

The Josephson effect arises when two superconductors are weakly coupled. Here we present a derivation of the Josephson relations for a certain configuration, where two superconductors separated by an insulating barrier. The derivation and notation follow that of Barone and Paterno. [14] For the derivation we will be bringing two superconductors together, from the left(L) and the right(R), Fig. 2.1 The quantum mechanical treatment of superconductors tells us that the electrons in an isolated superconductor can be described by a single macroscopic

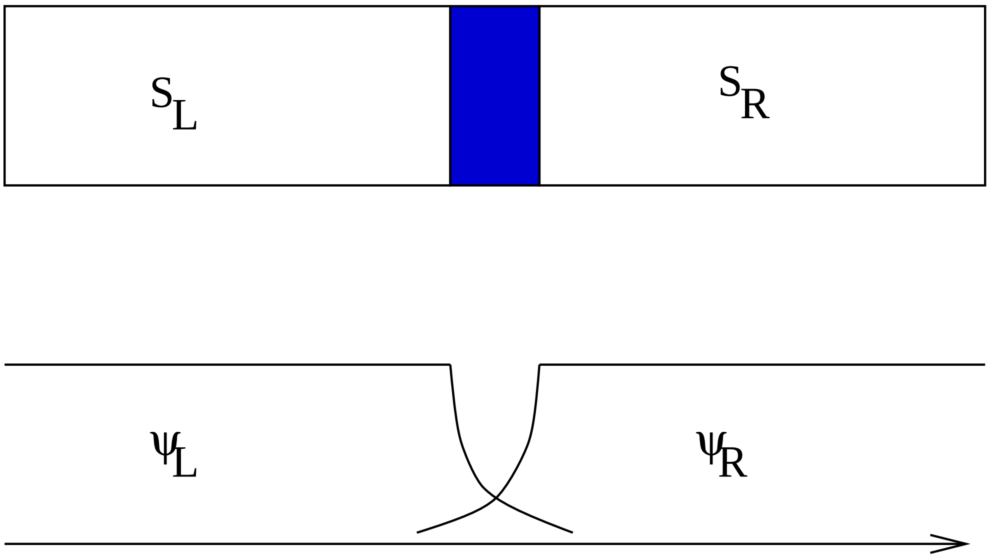

Figure 2.1: Schematic diagram of the left and the right superconductors, with their wave-functions.

quantum state. The Schroedinger equation

$$i\hbar\frac{\partial|\psi>}{\partial t} = \hat{H}|\psi>, \tag{2.1}$$

where $\hat{H}$ is the Hamiltonian of the system, yields

$$i\hbar\frac{\partial\psi_R}{\partial t} = \hat{H}_R\psi_R = E_R\psi_R, \tag{2.2}$$

$$i\hbar\frac{\partial\psi_L}{\partial t} = \hat{H}_L\psi_L = E_L\psi_L, \tag{2.3}$$

where E_R and E_L are the energies of the two wave functions. The two superconductors become weakly coupled as they are brought together, changing (2.2), and (2.3) to

$$i\hbar\frac{\partial\psi_R}{\partial t} = E_R\psi_R + K\psi_L, \tag{2.4}$$

$$i\hbar\frac{\partial\psi_L}{\partial t} = E_L\psi_L + K\psi_R, \tag{2.5}$$

where K is a small coupling constant. For two isolated superconductors the energies are the two chemical potentials. For a dc voltage difference between the two superconductors, the energy difference is $E_L - E_R = 2eV$. Choosing the potential energy to be zero halfway between the value on the right and the left, we can rewrite (2.4), and (2.5) as

$$i\hbar \frac{\partial \psi_R}{\partial t} = -eV\psi_R + K\psi_L, \tag{2.6}$$

$$i\hbar \frac{\partial \psi_L}{\partial t} = eV\psi_L + K\psi_R. \tag{2.7}$$

The wavefunctions ψ_L and ψ_R have the form $\psi_L = \sqrt{\rho_L} e^{i\phi_L}$, and $\psi_R = \sqrt{\rho_R} e^{i\phi_R}$, where ρ is the electron pair density in a superconductor. Defining $\phi = \phi_L - \phi_R$ and equating the real and imaginary terms of 2.6, and 2.7 we have

$$\frac{\partial \rho_L}{\partial t} = \frac{2K}{\hbar}\sqrt{\rho_L \rho_R} \sin\phi, \tag{2.8}$$

$$\frac{\partial \rho_R}{\partial t} = -\frac{2K}{\hbar}\sqrt{\rho_L \rho_R} \sin\phi, \tag{2.9}$$

$$\frac{\partial \phi_L}{\partial t} = \frac{K}{\hbar}\sqrt{\frac{\rho_L}{\rho_R}} \cos\phi + \frac{eV}{\hbar}, \tag{2.10}$$

$$\frac{\partial \phi_R}{\partial t} = \frac{K}{\hbar}\sqrt{\frac{\rho_L}{\rho_R}} \cos\phi - \frac{eV}{\hbar}. \tag{2.11}$$

The pair current density can be defined as

$$J \equiv \frac{\partial \rho_L}{\partial t} = -\frac{\partial \rho_R}{\partial t}. \tag{2.12}$$

Therefore, by (2.8, 2.9) we have

$$J = \sqrt{\rho_L \rho_R} \sin\phi. \tag{2.13}$$

If we assume the superconductors have equal and constant pair densities, $\rho_L = \rho_R = \rho_1$, where ρ_1 is a constant we can rewrite (2.13) as

$$J = J_c \sin\phi, \tag{2.14}$$

where $J_c = 2K\rho_1/\hbar$. It appears that we are assuming that the constant pair densities have nonzero time derivatives. However, we assume that the superconductors are connected to a circuit, allowing the electron pairs to dissipate or be replaced. Inclusion of this additional current would not change the final results. From the other two equations (2.10, 2.11) we have

$$\frac{\partial \phi}{\partial t} = \frac{2eV}{\hbar}. \tag{2.15}$$

Equations (2.14, 2.15) are called the Josephson relations and are the basis for most studies of the Josephson effect. The dc Josephson effect arises when $V = 0$. By Eq. (2.15) the phase difference is constant, but it is not necessarily zero. By Eq. (2.14) this means a zero potential can exist even for a nonzero current density. For this reason J_c is often called the critical current density, which is the largest current density the junction can sustain without developing a voltage.

The ac Josephson effect arises when V is a nonzero constant. By integrating Eq. (2.15) we find $\phi = \phi_0 + 2e/\hbar Vt$, so the current density is

$$J = J_c \sin(\phi_0 + \frac{2eVt}{\hbar}). \tag{2.16}$$

From this equation we see that a constant nonzero voltage produces an alternating current.

2.3 The RCSJ model

The resistively and capacitively shunted junction (RCSJ) model is used to describe the Josephson junction properties for finite voltage. We model the physical Josephson junction by the ideal one plus a resistance R and a capacitance C, as seen in Fig. 2.2. The resistance introduces dissipation while C reflects the geometric capacitance between the two electrodes. The current I is equal to the total junction current from the three parallel channels, as follows

$$I = I_{c0} \sin\phi + \frac{V}{R} + C\frac{dV}{dt}. \tag{2.17}$$

The usual notation for the critical current is I_c which denotes an observable critical current which may be less than I_{c0}. Using the Josephson

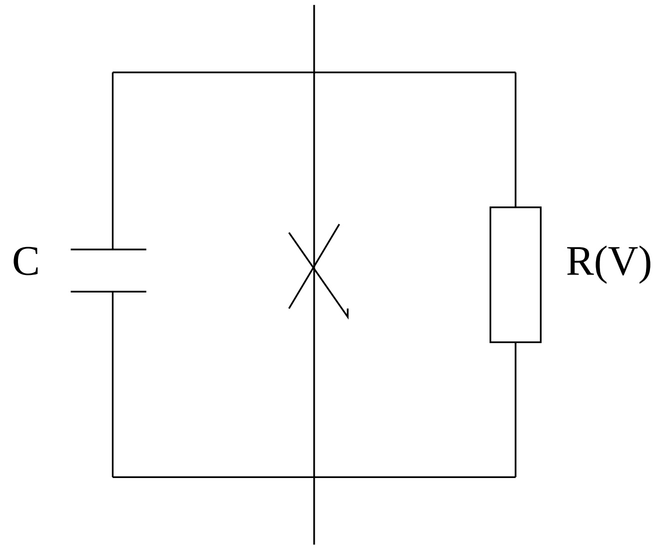

Figure 2.2: Circuit diagram.

relation for V Eq. (2.15) we obtain the second order differential equation

$$\frac{d^2\phi}{d\tau^2} + Q^{-1}\frac{d\phi}{d\tau} + \sin\phi = \frac{I}{I_{c0}}, \tag{2.18}$$

where τ is in units of $(\omega_p)^{-1}$ where $\omega_p = (\frac{2eI_{c0}}{\hbar c})^{1/2}$ is the plasma frequency, and $Q = \omega_p RC$ is the quality factor.

2.3.1 Overdamped junctions

If C is small so that $Q << 1$ Eq. (2.18) reduces to a first order differential equation which is

$$\frac{d\phi}{d\tau} = \frac{2eI_{c0}R}{\hbar}(\frac{I}{I_{c0}} - \sin\phi). \tag{2.19}$$

The time average voltage is obtained by integrating this equation for time T required by ϕ to advance by 2π, and using $2eV/\hbar = 2\pi/T$ the resulting equation for the voltage is

$$V = R(I^2 - I_{c0}^2)^{1/2}, \tag{2.20}$$

and is equal to zero for $I < I_{c0}$, while $V = IR$ for $I > I_{c0}$.

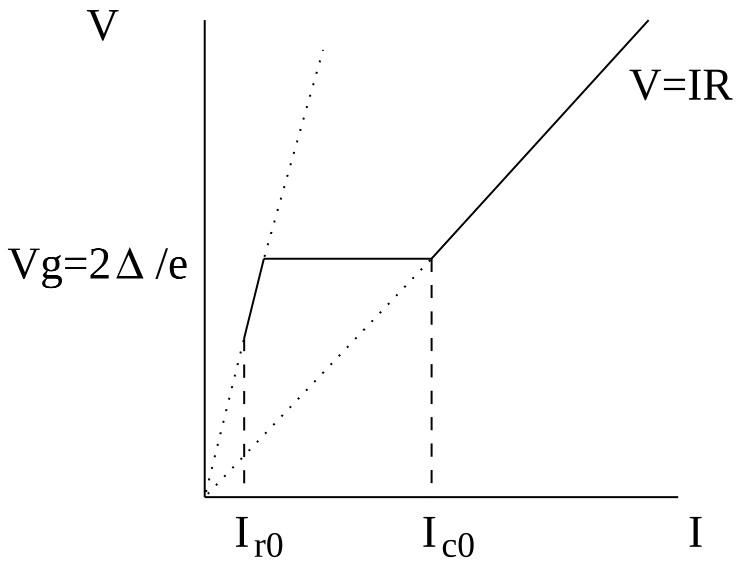

Figure 2.3: I-V diagram for underdamped junction.

2.3.2 Underdamped junctions

When C is large $Q > 1$ the $I-V$ curve becomes hysteretic. For $V = 0$ I is increasing until I_{c0} where it jumps discontinuously to a finite voltage $V_g = \frac{2\Delta}{e}$ equal to the energy gap voltage, as seen in Fig. 2.3. If I is reduced below I_{c0}, V does not drop back to zero until a "retrapping current" $I_{r0} = 4I_{c0}/\pi Q$ is reached.

2.4 The Josephson effect in the presence of magnetic field

We consider the junction shown in Fig. 2.4 between superconductors S_L, S_R. We choose a coordinate system such that the electrode surfaces are parallel to the xy-plane and the tunneling current is along the z direction. We will examine the effect of the magnetic field H applied in the y direction which is small compared to λ_J. The magnetic field penetrates into the superconductors a distance equal to the London penetration depth $\lambda_{L,R}$ respectively (shaded area in Fig. 2.4). From

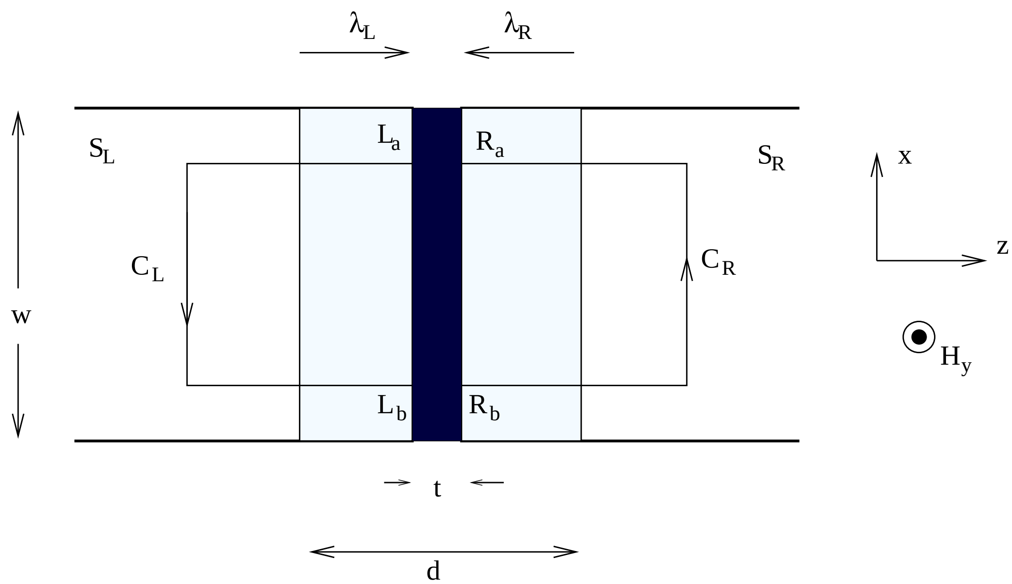

Figure 2.4: Plot of the junction geometry of length w. The magnetic field is applied in the y direction.

equation (1.12) the phases ϕ_L, ϕ_R in each superconductor satisfy

$$\bigtriangledown\phi_{L,R} = \frac{e^*}{\hbar c}(\frac{m^*c}{e^{*2}\rho_s}\mathbf{J} + \mathbf{A}), \tag{2.21}$$

where $\mathbf{A}$ is the vector potential. We integrate along the curves C_L, C_R as follows

$$\phi_{Ra}(x) - \phi_{Rb}(x+dx) = \frac{e^*}{\hbar c}\int_{C_R}(\mathbf{A} + \frac{m^*c}{e^{*2}\rho_s}\mathbf{J})\cdot\mathbf{dl}, \tag{2.22}$$

$$\phi_{Lb}(x+dx) - \phi_{La}(x) = \frac{e^*}{\hbar c}\int_{C_L}(\mathbf{A} + \frac{m^*c}{e^{*2}\rho_s}\mathbf{J})\cdot\mathbf{dl}, \tag{2.23}$$

where the paths $C_{L,R}$ are extended in the bulk where no current exists, and $\mathbf{dl}$ is at right angles to $\mathbf{J}$ for the path within the area where the magnetic field penetrates. Adding (2.22), and (2.23) we have

$$\phi(x+dx) - \phi(x) = [\phi_{Lb}(x+dx) - \phi_{Rb}(x+dx)] - [\phi_{La}(x) - \phi_{Ra}(x)] =$$

$$\frac{e^*}{\hbar c}[\int_{C_L}\mathbf{A}\cdot\mathbf{dl} + \int_{C_R}\mathbf{A}\cdot\mathbf{dl}], \tag{2.24}$$

$$\phi(x+dx)-\phi(x)=\frac{e^*}{\hbar c}\oint \mathbf{A}\cdot\mathbf{dl}=\frac{e^*}{\hbar c}H_y(\lambda_R+\lambda_L+t)dx=\frac{e^*}{\hbar c}H_y d dx, \tag{2.25}$$

or

$$\frac{d\phi}{dx}=\frac{e^*}{\hbar c}dH_y, \tag{2.26}$$

where d is the sum of the penetration depths in two superconductors plus the thickness of the insulating barrier. Equation (2.26) is a local relation. This means that the gradient of the phase ϕ depends on the local value of the field. However in some cases it can be generalized in a way that the gradient of the phase ϕ depends on the field in neighboring points and the relation becomes non local.

2.5 Junctions with negligible screening

When the junction length w is small the externally applied field becomes equal to the self field and Eq. (2.26) becomes $\phi(x)=\phi_0+kx$ where $k=2\pi Hd/\Phi_0$, ϕ_0 is the phase at the origin $x=0$. The supercurrent through the junction is then given by

$$I_s=\int\int J_c(x,y)\sin\phi(x)dxdy, \tag{2.27}$$

where the integration is over the junction area. After integration on y, we can rewrite (2.27) as

$$I_s=\int J_c(x)\sin(\phi_0+kx)dx, \tag{2.28}$$

where $J_c(x)=\int J_c(x,y)dy$ is the critical current density per unit length along x.

If we choose a rectangular junction with dimensions $X\times Y$ then $J_c(x)=J_cY$. We perform the integration in (2.28) and choose ϕ_0 in order to maximize the current. The result is

$$I_{max}=\frac{\sin\pi\frac{\Phi}{\Phi_0}}{\pi\frac{\Phi}{\Phi_0}}, \tag{2.29}$$

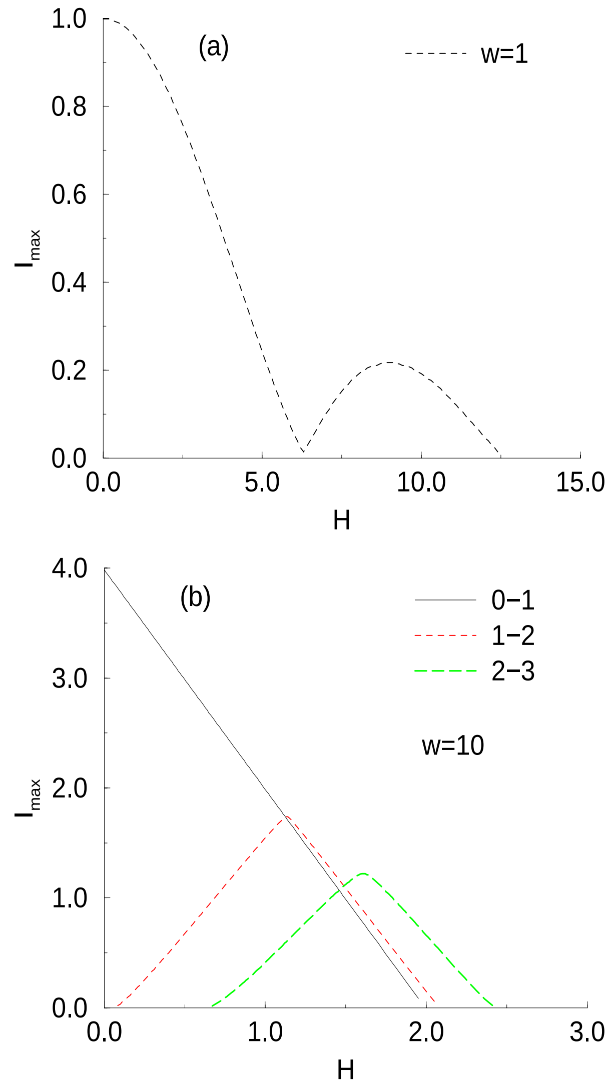

Figure 2.5: Plot of the maximum tunneling current as a function of applied magnetic field for a short junction with: (a) $w = 1.0$ and (b) $w = 10$.

where $\Phi = Hwd$ is the applied flux, $\Phi_0 = \frac{hc}{2e}$ the flux quantum [14]. In Fig. 2.5a we present the maximum tunneling current as a function of applied magnetic field for a short junction with $w = 1.0$. This pattern is often called Fraunhofer diffraction pattern by analogy to the case of light passing through a narrow rectangular slit. Each of the lobes in the diagram can be labeled by the pair of integers $(n, n+1)$ where at one end the magnetic field corresponds to exactly n fluxons (i.e. flux= $n\Phi_0$) and at the other end $n+1$ fluxons. For the case of a long junction the problem was solved by Owen and Scalapino [74], and there, the different lobes overlap (as shown in Fig. 2.5b for $w = 10$).

2.6 The electrodynamics of the Josephson junction

We will examine the effect of the Josephson currents on the time dependent electromagnetic fields in the barrier. We use the Maxwell equation

$$\nabla \times \mathbf{H} = \frac{4\pi}{c}\mathbf{J} + \frac{1}{c}\frac{\partial \mathbf{D}}{\partial t}, \tag{2.30}$$

which in the z-direction is written as

$$\frac{\partial H_y}{\partial x} - \frac{\partial H_x}{\partial y} = \frac{4\pi}{c}J_z + \frac{1}{c}\frac{\partial D_z}{\partial t}. \tag{2.31}$$

We use the equation (2.26) and a similar equation in the y direction

$$\frac{d\phi}{dy} = -\frac{e^*}{\hbar c}dH_x, \tag{2.32}$$

to rewrite the Maxwell equation (2.30) as

$$\frac{\hbar c^2}{8\pi ed}\left(\frac{\partial^2\phi}{\partial x^2} + \frac{\partial^2\phi}{\partial y^2}\right) = J_c \sin\phi + C\frac{\partial V}{\partial t}, \tag{2.33}$$

where

$$D_z = \epsilon E_z = \epsilon\frac{V}{t}, \tag{2.34}$$

ϵ is the dielectric constant of the barrier, t is the the oxide barrier height, E_z is the electric field across the barrier, and V is the voltage across the barrier.

$$C = \frac{\epsilon}{4\pi t}, \tag{2.35}$$

is the capacity of the junction per unit area, J_c is the Josephson critical current. Using the Josephson relation (2.15), Eq. (2.33) is transformed to the sine-Gordon equation

$$\frac{\partial^2\phi}{\partial x^2} + \frac{\partial^2\phi}{\partial y^2} - \frac{1}{\overline{c}^2}\frac{\partial^2\phi}{\partial t^2} = \frac{1}{\lambda_J^2}\sin\phi, \tag{2.36}$$

where the Josephson penetration depth given by

$$\lambda_J = \sqrt{\frac{\hbar c^2}{8\pi e d J_c}}, \tag{2.37}$$

is of the order of $2\mu m$, for $J_c = 10^8 A/m^2$ and depends both on material and geometry properties.

$$\overline{c} = c(\frac{1}{4\pi C d})^{1/2} = c(\frac{t}{\epsilon d})^{1/2}, \tag{2.38}$$

since $d \approx 15A^\circ$, $\epsilon = 6$ the velocity of the electromagnetic waves in the junction is $\overline{c} \approx c/20$.

For the static case, λ_J plays the role of a penetration depth if $\phi << 1$ since then (2.36) reduces to

$$\frac{d^2\phi}{dt^2} = \frac{\phi}{\lambda_J^2}. \tag{2.39}$$

The solutions of this equation are of the form $\phi \sim e^{\pm x/\lambda_J}$ where x is measured from the outside edge of the junction. When the external field is less than the critical field the phase ϕ exponentially decays to zero in the interior of the junction. It is often called as 'Meissner solution'. A junction is called small if its length and width are small compared to λ_J and long if its length $w >> \lambda_J$ and its width is much smaller than λ_J.

In the small junction limit Eq. (2.36) reduces to

$$\frac{d^2\phi}{dt^2} + \omega_p^2 \sin\phi = 0, \tag{2.40}$$

where $\omega_p^2 = \frac{\bar{c}^2}{\lambda_J^2}$. This equation has the same form as the one found from the RCSJ approximation with no damping and no external current. The s-G equation must be generalized like the RCSJ model by the introduction of a damping term proportional to $\partial\phi/\partial t$.

2.7 The $I - V$ characteristics, for small junctions

The current-voltage ($I-V$) curve for a superconductor insulator superconductor ($S - I - S$) junction consists of two branches above $\frac{2\Delta}{e}$ and bellow $-\frac{2\Delta}{e}$ which represent the normal electron tunneling. We must break a Cooper pair so that electrons can tunnel through the insulating region. As a result the minimum voltage appears at the energy $\frac{2\Delta}{e}$.

The current at zero voltage is a direct result of the Cooper pair tunneling and is known as Josephson current. However there is a limit to the amount of current that the Cooper pairs can carry and if too much current is applied the Josephson effect is lost and the current is carried by the normal electrons. The maximum dc current that can be passed through the junction at zero voltage is known as Josephson current density J_c.

2.8 Solitons in long junctions

An interesting type of solution for the long junction geometry is the soliton which has the form

$$\phi(x,t) = 4\tan^{-1}(\exp[\pm\frac{x - x_0 - ut}{\sqrt{1-u^2}}]), \tag{2.41}$$

where x is in units of λ_J and the velocity u is in units of $\bar{c}$. This solution goes from 0 to 2π as $(x - (x_0 + ut))$ goes from $-\infty$ to $+\infty$ for the upper sign solution. It also maintains the value $\phi = \pi$ at the moving point $x = x_0 + ut$. There is a positive Josephson current localized at a distance λ_J to the left of $x_0 + ut$ and a similar negative Josephson current to the right of $x_0 + ut$. Other exact solutions are the multi-fluxon solutions, fluxon-antifluxon solutions, plasma waves, etc. When the propagating fluxon reaches the end of the junction it is reflected buck as an antifluxon. This motion is periodic with period $T = \frac{2w}{u\overline{c}}$. The phase changes by 4π. Thus in the relativistic limit $u \approx 1$ the dc voltage will be $V = \frac{h\overline{c}}{we^*}$. This constant value is called first zero field step (ZFS).

2.9 Inline geometry and stability of static solutions

The main subject of this chapter is to describe the static solutions of the sine-Gordon equation. The case of inline geometry is a one dimensional problem, even for a wide junction, and one can obtain analytic solutions [74]. Furthermore one can easily check their stability by using linear perturbations. The particular cases of zero external magnetic field and inline bias current also reduce the overlap boundary conditions to inline ones.

In the one-dimensional case we have to solve the following problem

$$-\frac{d^2\phi(x,t)}{dt^2} + \frac{d^2\phi(x,t)}{dx^2} = \sin\phi(x,t), \tag{2.42}$$

x is in units of λ_J, H is in units of $\frac{4\pi}{c}\lambda_J J_c$, and I is measured in units of $\lambda_J J_c$.

Two boundary conditions for the $s-G$ equation are obtained from the continuity of the magnetic field H across the junction edges. Using dimensionless units we have

$$H(\pm w/2) = \frac{d\phi}{dx}|_{\pm\frac{w}{2}}, \tag{2.43}$$

where w is the normalized junction length. Also $H(\pm w/2)$ is related to the current line density I and H by Ampere's law

$$H(w/2) - H(-w/2) = \frac{d\phi}{dx}|_{\frac{w}{2}} - \frac{d\phi}{dx}|_{-\frac{w}{2}} = I, \tag{2.44}$$

$$H(w/2) + H(-w/2) = \frac{\partial\phi}{\partial x}|_{\frac{w}{2}} + \frac{\partial\phi}{\partial x}|_{-\frac{w}{2}} = 2H, \tag{2.45}$$

from (2.44,2.45) we obtain the following inline boundary conditions

$$\frac{d\phi}{dx}\Big|_{x=\pm w/2} = \pm\frac{I}{2} + H \equiv \gamma_{\pm}. \tag{2.46}$$

Eq. (2.42) has a static solution $\Phi_0(x)$, implicitly expressed using elliptic functions [2] as

$$\sin\Phi_0(x) = -2\sqrt{m}\ sn\,(x + x_0|m)\ \ dn\,(x + x_0|m)\,, \tag{2.47}$$

$$\cos\Phi_0(x) = 2m\ sn^2\,(x + x_0|m) - 1, \tag{2.48}$$

$$\frac{d\Phi_0}{dx} = 2\sqrt{m}\ cn\,(x + x_0|m)\,, \tag{2.49}$$

where the modulus m determines the period of the cn elliptic function (equal to $4K(m)$) and the arbitrary constant x_0 the phase at the center of the junction. They are determined by the boundary conditions (2.46). Introducing (2.49) into (2.46) we get

$$2\sqrt{m}\ cn(x_0 + \frac{w}{2}|m) = \gamma_+, \tag{2.50}$$

$$2\sqrt{m}\ cn(x_0 - \frac{w}{2}|m) = \gamma_-. \tag{2.51}$$

A useful quantity to classify the solutions is the fluxon content or the magnetic flux in units of the quantum of flux, defined by

$$N_f = \frac{1}{2\pi}\left\{\Phi(\frac{w}{2}) - \Phi(-\frac{w}{2})\right\}.$$

At specific values of H, N_f takes integer values, so that the flux is that of an integer number of fluxons.

To check the stability of the static solution (2.47)-(2.49) we consider small perturbations on the static solution $\Phi_0(x)$ in the form

$$\Phi(x,t) = \Phi_0(x) + U(x,t) \tag{2.52}$$

and linearize Eq. (2.42) with respect to $U(x,t)$, to obtain

$$-U_{tt} + U_{xx} = \cos\Phi_0(x)\cdot U. \tag{2.53}$$

There is no loss of generality if we consider specific perturbations in the form

$$U(x,t) = X(x)e^{st}. \tag{2.54}$$

This way we obtain from Eq. (2.53) the eigenvalue equation

$$-X'' + \cos\Phi_0(x)\cdot X = \lambda\cdot X, \tag{2.55}$$

under the boundary conditions

$$X'|_{x=\pm w/2} = 0. \tag{2.56}$$

In Eq. (2.55) $\lambda = -s^2$. It is seen from Eq. (2.54) that if the eigenvalue problem (2.55)-(2.56) has a negative eigenvalue the static solution $\Phi_0(x)$ is unstable. If all the eigenvalues are positive $\Phi_0(x)$ is stable, while the case $\lambda = 0$ corresponds to neutral stability and defines the boundary of stability. In the following we consider the two special cases $\gamma_+ = \gamma_-$ ($I = 0$) and $\gamma_+ = -\gamma_-$ ($H = 0$) separately, since the associated boundary conditions are easy to handle and the stability analysis is simplified.

To get a feeling concerning the possible solutions, we plot from the boundary conditions (2.46) and (2.50,2.51) the constant H and I contours in the plane of the m and x_0 parameters, for $w = 3\pi/2$ in Fig. 2.6. We give different plots for $m < 1$ and $m > 1$. The lines labeled with "0" correspond to $H = 0$ (or $I = 0$ for I contours) and in both cases their network encloses areas with a single maximum (denoted by "+") or minimum ("−") inside. Notice that there are two types of curves on which $H = 0$ (or $I = 0$) as summarized in Table 2.1.

The curved lines in Fig. 2.6 correspond to the solutions of the first line in the table which we call fixed x_0 solutions, in the sense that the shift is a fixed fraction of the period. From (2.50,2.51) we see that the physical quantities I and H are periodic functions of x_0 with period $4K(m)$. There are also solutions that have a fixed $m = m^\star$ and arbitrary x_0, and correspond to the vertical lines in Fig. 2.6 (remark that contour fitting can be distorted when two equicurrent lines cross). Similar results hold for the constant I contours. For $m > 1$ at the vertical $I = 0$ curves we have an integer number of fluxons in the junction. Thus on the lines through c (a) we have $N_f = 1$ (2) correspondingly.

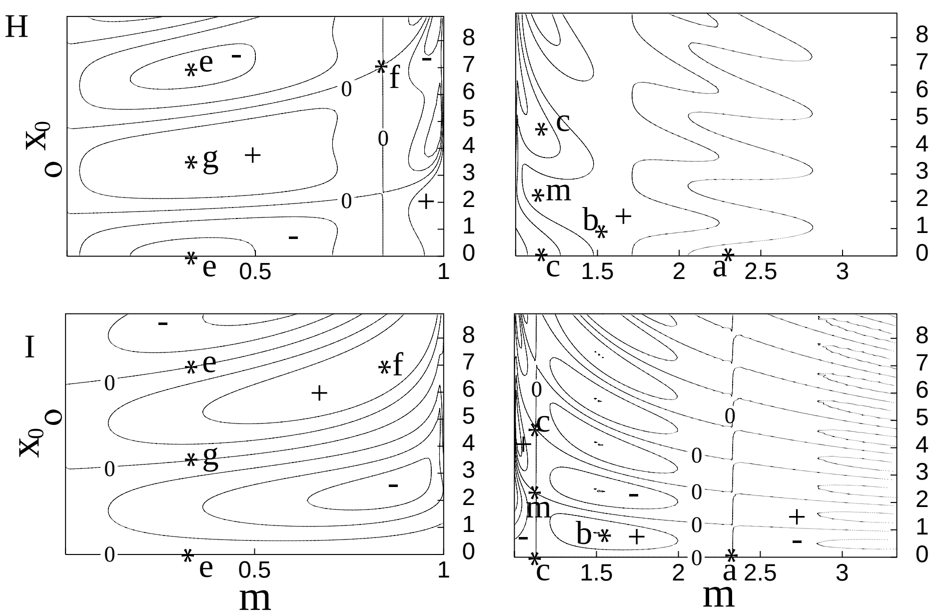

Figure 2.6: Constant H (a) and I (b) contours in the $(m,\, x_0)$ plane. The curves with the symbol O are for $H = 0$ in (a) and $I = 0$ in (b). The signs " + " or " − " give the sign of I and H. The letter symbols signify the same points in the I and H contours.

Table 2.1: Different types of curves due to various selections of m and x_0.

	m	x_0 (periodic)
$H=0$	$0<m<1$	$\pm(2n+1)K(m), n=0,1,\ldots$
	$m=m^*, n=0,1,\ldots n_{max}$ $\frac{w}{2}=(2n+1)K(m^*)$ if $w>\pi$	$-\infty<x_0<\infty$
I=0	$0<m<1$	$x_0=\pm 2nK(m)$, n=0,1,...
	$1<m<\infty$	$x_0=\pm\frac{1}{\sqrt{m}}2nK(\frac{1}{m})$
	$m=m^*<1$ $\frac{w}{2}=2nK(m^*), w>2\pi$ $n=0,1,\ldots,n_{max}$	$-\infty<x_0<\infty$
	$m=m^*>1$ $\frac{w}{2}=\frac{1}{\sqrt{m^*}}nK(\frac{1}{m^*})$ $n=0,1,\ldots$	$-\infty<x_0<\infty$

In the current contours the points f and b correspond to peaks in the I_{max} (see section 4.4). In the following we will focus our attention on the solutions where either H or I .

2.10 Numerical procedure to obtain the I_{max} vs H diagram

For the static solutions, the differential equation (2.42) turns into a difference equation on a grid of size Δx

$$\frac{\phi_{n+1}-2\phi_n+\phi_{n-1}}{(\Delta x)^2}=\sin(\phi_n). \tag{2.57}$$

The boundary conditions are then described as difference equations,

$$\frac{\phi_{n_j}-\phi_{n_j-1}}{(\Delta x)}=I/2+H, \tag{2.58}$$

$$\frac{\phi_2-\phi_1}{(\Delta x)}=-I/2+H, \tag{2.59}$$

where $n_j = \frac{w}{\Delta x}$ is the total number of junctions, and we set $n_j = 50$. These coupled differential equations are solved using a relaxation method to find $\phi(x)$. An initial solution is assumed for $\phi(x)$ that is close to the desired solution. The magnetic field H is fixed and the current is set to $I = 0$. For given I, H, the solution is iterated for a maximum of $N_{max} = 500$ times. The convergence criterion is then

$$\sum_{n=1}^{n_j} (\phi_n^2 - \overline{\phi}_n^2)^{1/2} < \epsilon, \tag{2.60}$$

where ϕ_n, and $\overline{\phi}_n$ define values of the phase at two successive iteration steps, and $\epsilon = 0.001$. If this criterion has not been satisfied after N_{max} iterations the iteration procedure is said to diverge for that value of I, H parameters. If this criterion is satisfied for $N < N_{max}$ then the solution converges. Then the current I is increased while the convergence criterion is satisfied. The value of current for which the iteration procedure diverges defines the critical current I_{max} for a given magnetic field. The process is continued by increasing the magnetic field H for $I = 0$ using as initial condition the phase $\phi(x)$ at the previous value of H and repeat the same procedure to find I_{max} for the new value of the magnetic field H. This is repeated until the critical value of the magnetic field where the mode terminates is reached.

2.11 No magnetic field case (H=0)

In the absence of external magnetic field we have $\gamma_+ = -\gamma_- = \frac{I}{2}$ and Eqs. (2.50,2.51) reduce to

$$2\sqrt{m}cn\left(x_0 + \frac{w}{2}|m\right) = \frac{I}{2}, \tag{2.61}$$

$$\sqrt{m}cn\left(x_0 - \frac{w}{2}|m\right) = -\frac{I}{2}, \tag{2.62}$$

which determine the parameters m and x_0 that characterize the periodicity and phase shift of the static solutions. There are two different classes of solutions due to the antisymmetry of the boundary conditions, which can be satisfied for different I either by fixing x_0 or m.

2.11.1 Fixed x_0 solutions

It is seen from Eqs. (2.61,2.62) and the symmetry of the elliptic functions that for positive I one choice for x_0 in (2.61,2.62) is $x_0 = -K(m)$ ($K(m)$ is the elliptic integral of the first kind), so that x_0 is fixed to $\frac{1}{4}$ of the period of the elliptic function. It is in that sense that we call them fixed x_0 solutions. Strictly x_0 is not a constant independent of m since $K(m)$ is a function of m. Thus we have (see [2])

$$\frac{I}{2} = 2\sqrt{m(1-m)}\,\frac{sn(\frac{w}{2}|m)}{dn(\frac{w}{2}|m)}, \quad 0 \leq m < 1, \tag{2.63}$$

$$\cos\Phi_0(x) = 2\ m\ \frac{cn^2(x|m)}{dn^2(x|m)} - 1, \quad 0 \leq m < 1, \tag{2.64}$$

$$\sin\Phi_0(x) = 2\ \sqrt{m\ (1-m)}\frac{cn(x|m)}{dn^2(x|m)}, \quad 0 \leq m < 1. \tag{2.65}$$

Another possibility is $x_0 = K(m)$ (x_0 is shifted by half of a period) for the case that $2K(m) < \frac{w}{2} < 4K(m)$, or more generally when $sn(\frac{w}{2}|m) < 0$, since we are limiting ourselves to $I > 0$. This means that every time w increases by 2π we introduce two extra solutions. To put it in other words the function $I(m)$, in (2.63), is highly oscillating for large w. We do not need to consider the case that $m > 1$ since in that case we cannot satisfy the antisymmetric boundary conditions for the external current.

In Fig. 2.7a we present three plots of I vs m for $w = \frac{2\pi}{3},\ \frac{3\pi}{2},\ \frac{5\pi}{2}$. We see that for small $w < 2\pi$ there is, as expected, only one lobe for $x_0 = -K(m)$, and as we will see later only the part to the right of the maximum will correspond to stable solutions, while the peak corresponds to the maximum current for zero magnetic field. For $w = \frac{5\pi}{2}$ we have an extra lobe, with the left one at $x_0 = K(m)$ and the right at $x_0 = -K(m)$. For $w = 10$ (dashed line in Fig. 2.7b) the right lobe has a maximum within 10^{-3} of $m = 1$ and corresponds to $x_0 = K(m)$, while the left to $x_0 = -K(m)$. The jump in path along two different curves is necessary because of the restriction of positive current I. Of course the curve is symmetric about the $I = 0$ line. The right lobe for $w = 10$ is shown in the inset of Fig. 2.7b in expanded form (solid line) with a different scale for m. The part that is of experimental interest

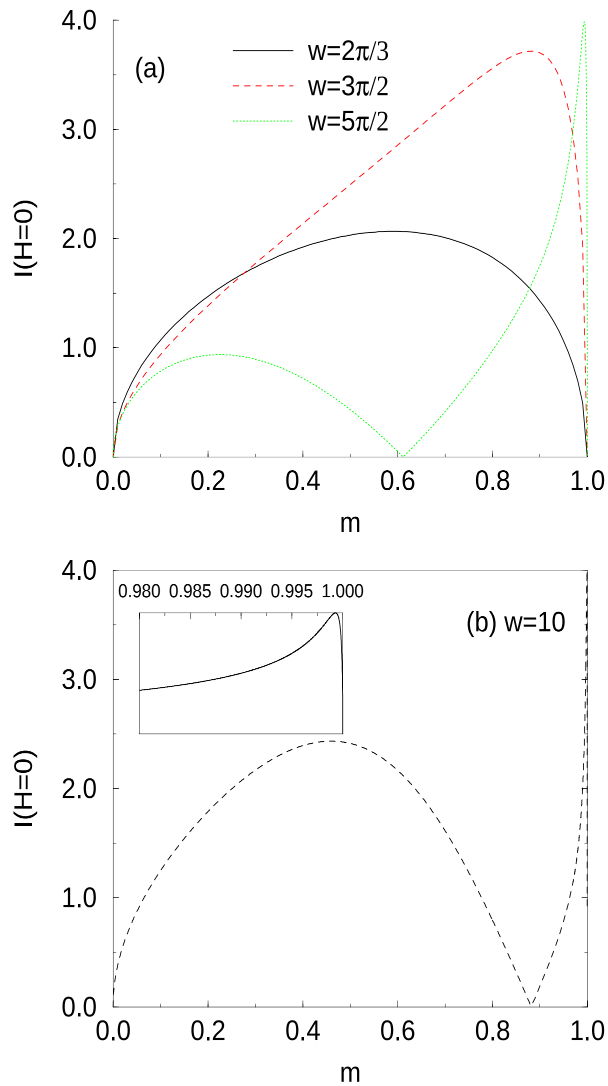

Figure 2.7: (a) Plot of $I(m)$ (using Eq. (13)) with $x_0 = -K(m)$ or $K(m)$ and three values of w: (i) $w = 2\pi/3$, (ii) $w = 3\pi/2$ and (iii) $w = 5\pi/2$. (b) Same as (a) with $w = 10$ (dashed line). The right lobe in (b) is also shown in an expanded scale for m (solid line). The small m scale is shown at the top of the figure.

is the last lobe near $m = 1$ to the right of the maximum. The two extremal m values correspond to trivial solutions $\Phi_0(x) = \pi$ $(m = 0)$ and $\Phi_0(x) = 0$ $(m = 1)$, the first of which is clearly unstable (pendulum analogy) and the second is stable. For currents above zero at $w = 10$ there are four possible solutions for a given $I < I^\star$, where $I^\star$ is the maximum of the lowest lobe.

Because the last lobe for large w is very steep it is useful to give some analytic formulas valid near $m = 1$ and for the maximum point. By using asymptotic formulas and assuming that $m_1 \equiv 1 - m \approx \epsilon^2$, where ϵ is a small parameter, we obtain the value of m_1 where I is a maximum as

$$m_1^{max} = \frac{4}{\sinh^2 \frac{w}{2}}.$$

The result is consistent with our scaling assumption with

$$\frac{1}{\sinh \frac{w}{2}} \sin \epsilon.$$

Thus care is required when simplifying the analytic formulas in [2] (see p. 574). The corresponding maximum current is

$$I = 4 - \frac{8}{\sinh^2 \frac{w}{2}}, \tag{2.66}$$

so that for large junction length w it approaches exponentially the infinite length limit. To the right of the maximum the relation between $I(m_1)$ is

$$I = 4 - m_1^{3/2} \frac{\tanh \frac{w}{2}}{\mathrm{sech} \frac{w}{2}}.$$

From the previous discussion we see that as we increase the junction length w we obtain more solutions. In Fig. 2.8a we give as a function of w the range of m values for each type of solution and the separating lines. These values were determined by solving (2.50,2.51) numerically. We remark that consecutive pairs of regions of solutions correspond to different x_0 (i.e. different lobes of Fig. 2.7). We see that when w increases by 2π a new pair of solutions is introduced. Thus near $w = 10$ we have four solutions labeled u, al, ar and a_0, the first two

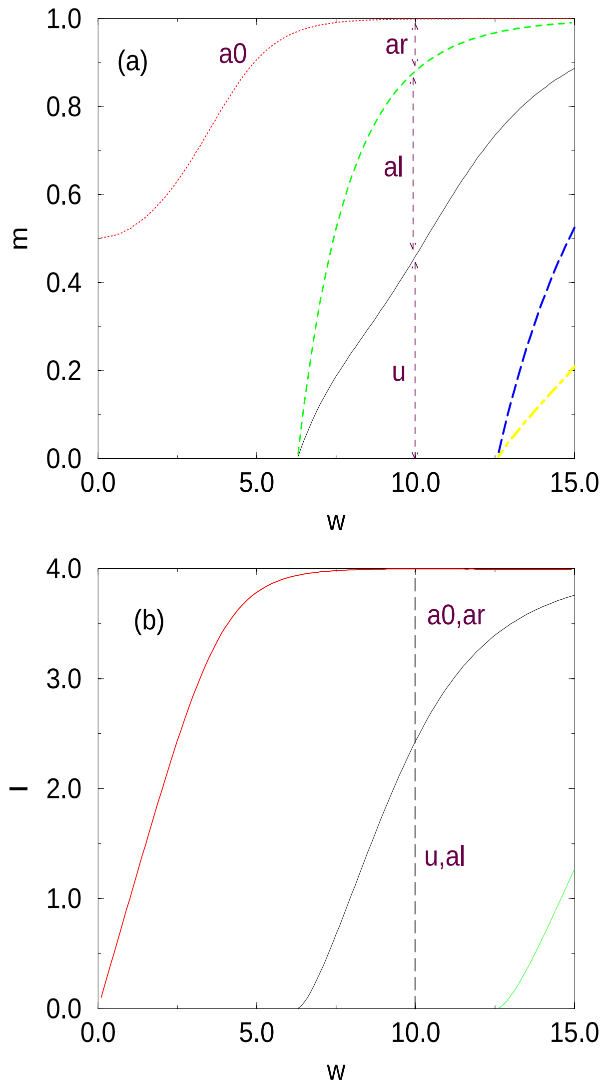

Figure 2.8: (a) A diagram of the different solutions in the space of parameter w and m with $x_0 = \pm K(m)$ for the solutions in equations (13)-(15). (b) The same as (a) but presented in the space of w and I (instead of m).

corresponding to $x_0 = K(m)$ and the last two to $x_0 = -K(m)$. For $w \to \infty$ there is an infinite number of solutions and many of the dividing lines coalesce at $m = 1$. The stability is checked by looking at the eigenvalues of the linearized problem in (2.55). We see that already for $w = 10$ only a small range near $m = 1$ gives stable solutions, while for $w = 14$ it is of the order 10^{-7}, which is extremely small and not visible on the scale of the plot. In Fig. 2.8b we give the same information but in a diagram of current vs w. The lines correspond to the maximum current for each lobe and below each line there are two solutions. Thus the solutions a_0 and ar have the same maximum current (starting from zero current) and correspond to the right lobe of Fig. 2.7b, while u and al to the left one. In order to make sure that we get all solutions we scan over m (with a uniform and fine grid), and the current is obtained from (2.63). As expected the maximum current for large w is accurately estimated by (2.66) down to $w = 4$, while for small w it varies linearly.

2.11.2 Fixed m solutions

Another possibility exists if $w > \pi$, so that we can fit in the length exactly an odd number of half periods. This automatically satisfies the antisymmetric boundary conditions due to the current. Then, there exists a fixed (sometimes more than one depending on the length) $m = m^*$ for which $w = 2K(m^*)$. In fact every time w increases by 2π there is an extra solution arising. Thus for $\pi(2n+1) < w < \pi(2n+3)$, we have solutions at $w = 2K(m), \cdots, 2(2n+1)K(m)$ with n-different values of m^*. By shifting x_0 we can obtain a range of possible currents I while always satisfying the boundary conditions at zero magnetic field. In Fig. 2.9a we plot the current as a function of x_0, for $w = 10$, where we expect two solutions of this type. The corresponding values of m^* are $m^* = 0.999272$ (from $w = 2K(m^*)$, see curves $1l$ and $1r$ in Fig. 2.9a) and $m^* = 0.213839$ ($w = 6K(m^*)$, see curves $0l$, $0r$ in Fig. 2.9a), with the maximum currents being $I_0 \approx 4$ (at $x_0 = -\frac{w}{2}$) and $I_1 = 1.8$ (at $x_0 = \frac{w}{6}$) correspondingly. These also coincide with the maximum currents obtained by fixing $x_0 = -K(m)$, $K(m)$ and varying m. It should be remarked, though that they correspond to different solutions as we increase the current ($I < I_{max}$). This can be seen by the different fluxon content of these solutions in Fig. 2.9b. At

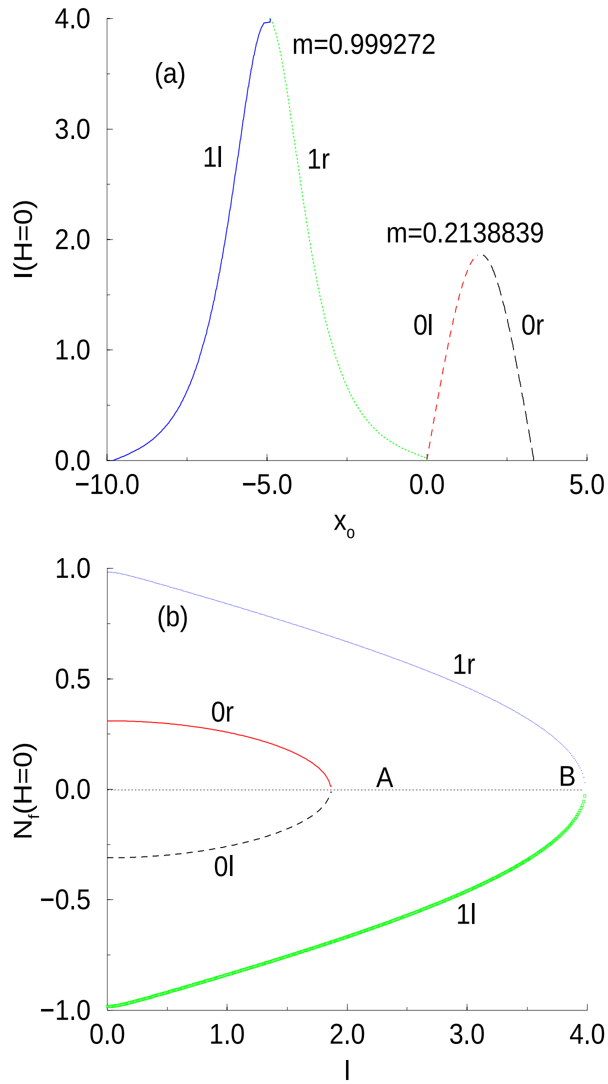

Figure 2.9: (a) Plot of $I(x_o)$ for $H = 0$, $w = 10$ and fixed m with (i) $m^* = 0.999272$ (curves $1l$ and $1r$) from $w = 2K(m^*)$, (ii) $m^* = 0.213839$ (curves $0l$ and $0r$) from $w = 6K(m^*)$. (b) Fluxon content N_f as a function of the bias current I for the different solutions with fixed m: (i) m=0.999272 with one half period of the elliptic function ($1r$ and $1l$). (ii) m=0.213839 with three half periods of the elliptic function ($0l$ and $0r$).

the maximum current value though they coincide. In comparison, the solutions in the previous subsection correspond to zero fluxon content $N_f = 0$.

2.11.3 Solutions for $w = 10$

We will present in more detail the calculations for $w = 10$ since this is a common length in experimental design of long junctions and one can clearly see the multiplicity of solutions. In Fig. 2.10 we present all the solutions (for constant x_0 and constant m) for $H = 0$ at three different currents in order to follow their evolution. The branch with a half period solution for $w = 2K(m)$ (see $1r$ and $1l$ in Fig. 2.10g-i) has a maximum current $I = 4$ which is the same as the maximum current in Fig. 2.7b. In fact at the maximum current (Fig. 2.10i) we have the coalescence of four different solutions. In the third column of Fig. 2.10 (i.e. g, h, i) we see the four solutions being different at $I = 0$ (see g) but converging to the same solution (modulo 2π) as I approaches the $I \approx 4$ (see i) value which is the maximum current for all four solutions. The four solutions come in pairs: two from the pair with $w = 2K(m)$ discussed earlier (i.e. $1r$, $1l$) and two from the right lobe of Fig. 2.7b, i.e. ar and $a0$ in Fig. 2.10g-i, discussed in the previous subsection. The other pair of solutions with 3 half periods when $w = 6K(m)$, i.e $0l$, $0r$ in Fig. 2.10a-c have a maximum current near $I = 1.8$. For higher currents (above the value at c) it jumps branch and converges to the solutions of the left lobe of Fig. 2.7b since the two pairs of solutions are quite close as can be seen from the plots in Fig. 2.10c and 2.10f. Notice that the currents are different for the two plots. We should also point out (to be discussed in the next section) that by slightly increasing the magnetic field the $w = 6K(m)$ solutions show an interesting bifurcating behavior with a jump in the maximum tunneling current. All solutions as seen in Fig. 2.9b come in pairs with opposite fluxon content. Thus on the line $N_f = 0$ (zero flux) we also have two pairs of solutions up to $I = 2.4$ (point A in Fig. 2.9b, where only the point at the maximum current is shown). One pair is the curves u, al in Fig. 2.10d, e, f. A second pair goes up to $I = 4.0$ (point B), i.e. the curves $a0$, ar in Fig. 2.10g-i. The solutions of each pair are different as can be seen in Fig. 2.10a, d, g or Fig. 2.10b, e, h and only coincide at the maximum

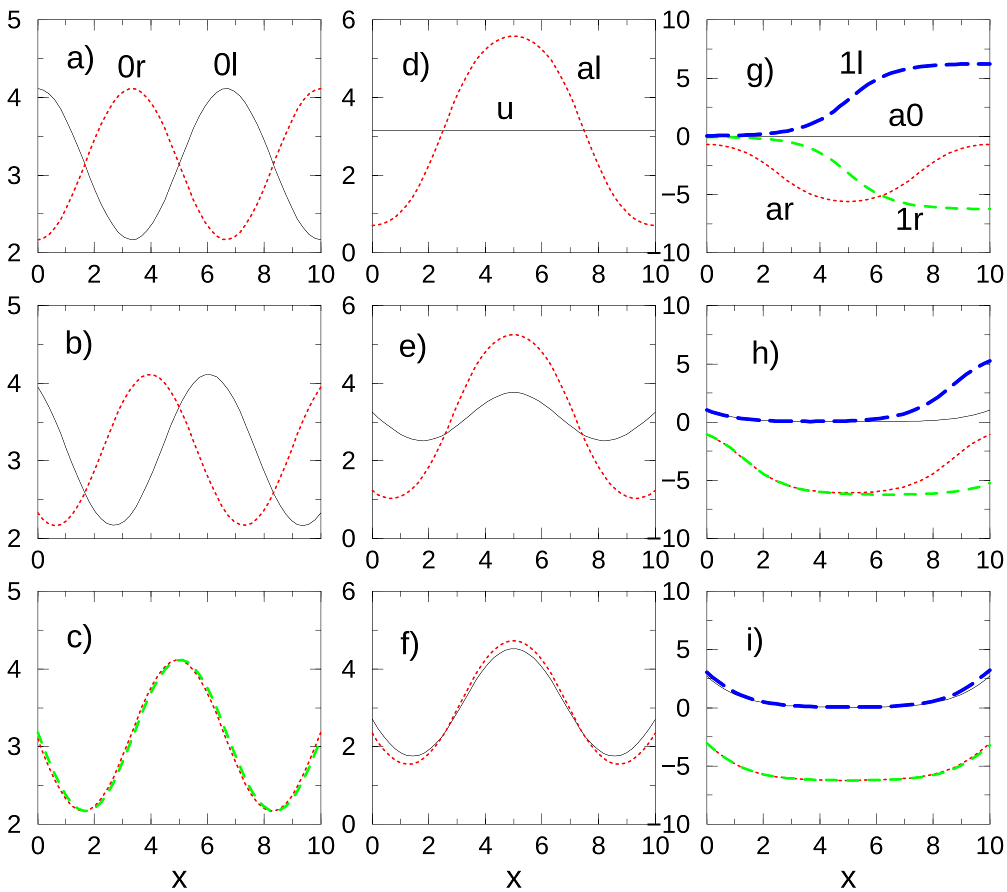

Figure 2.10: Plot of the phase distribution $\Phi(x)$ for all the solutions at $H = 0$ and three values of the current (different for each line). $(a,\ d,\ g)$ $I = 0$, $(b,\ e,\ h)$ $I = I_{max}/2$, $(c,\ f,\ i)$ $I = I_{max}$ (where I_{max} is different for each case). The three columns correspond to: $(a,\ b,\ c)$ the two solutions $(0l,\ 0r)$ with $m^* = 0.213839$. $(d,\ e,$ f) the two solutions $(u,$ $al)$ from the left lobe of Fig. 3b and $(g,\ h,\ i)$ the two solutions $(1r,\ 1l)$ for $m^* = 0.999272$ and the two solutions from the left lobe of Fig 5a (i.e. $a0,\ ar$)

current. Notice that u and $a0$ are simply displaced by π, while al and ar have opposite signs. With increasing current, though, they evolve very differently.

2.12 No current case ($I = 0$)

In the absence of external current Eqs. (2.50,2.51) reduce to the following

$$2\sqrt{m} cn \left(x_0 + \frac{w}{2} | m \right) = H, \tag{2.67}$$

$$2\sqrt{m} cn \left(x_0 - \frac{w}{2} | m \right) = H, \tag{2.68}$$

which determine the parameters m and x_0 that characterize the periodicity and phase shift of the static solutions. This is seen from Eqs. (2.67,2.68) and the periodicities of the elliptic functions. Notice that these are the only three possibilities leading to three branches, if we consider solutions, where only m varies and x_0 is fixed to $x_0 = 0$ or $x_0 = 2K(m)$. Here we need $x_0 = 2K(m)$, and not $x_0 = -K(m)$ as in the zero field solution, due to the symmetric boundary conditions for the magnetic field. At the same time we also have solutions where m is fixed and x_0 is varied continuously with the current.

2.12.1 Fixed x_0 solutions

We start by giving the three branches.

Branch I: An obvious choice in (2.67,2.68) is $x_0 = 0$, so that for $m \leq 1$

$$H = 2\sqrt{m}\ cn(\frac{w}{2} | m), \quad 0 \leq m < 1, \tag{2.69}$$

$$\cos \Phi_0(x) = 2\ m\ sn^2(x|m) - 1, \quad 0 \leq m < 1, \tag{2.70}$$

$$\sin \Phi_0(x) = -2\ \sqrt{m}\ sn(x|m) dn(x|m), \quad 0 \leq m < 1. \tag{2.71}$$

Another possibility is $x_0 = 2K(m)$ for the case that $K(m) < \frac{w}{2} < 3K(m)$, or more generally when $cn(\frac{w}{2}|m) < 0$, since we are limiting ourselves to $H > 0$. This means that every time w increases by 2π we introduce two extra solutions. To put it in other words the function $H(m)$ in (2.69) is highly oscillating for large w.

Branch II: For $x_0 = 0$ and $m > 1$ we use the notation $\bar{m} = 1/m$ and the transformation rules of elliptic functions [2] to obtain

$$H = \frac{2}{\sqrt{\bar{m}}}\ dn\left(\frac{w}{2}\frac{1}{\sqrt{\bar{m}}}|\bar{m}\right), \quad 0 \leq \bar{m} < 1, \tag{2.72}$$

$$\cos\Phi_0(x) = 2\ sn^2\left(x\frac{1}{\sqrt{\bar{m}}}|\bar{m}\right) - 1, \quad 0 \leq \bar{m} < 1, \tag{2.73}$$

$$\sin\Phi_0(x) = -2\ sn\left(x\frac{1}{\sqrt{\bar{m}}}|\bar{m}\right)\ cn\left(x\frac{1}{\sqrt{\bar{m}}}|\bar{m}\right), \quad 0 \leq \bar{m} < 1. \tag{2.74}$$

Branch III: Taking into account the period and symmetry of the nd elliptic function we can also put in Eqs. (2.67,2.68) $x_0 = \frac{1}{\sqrt{m}}K(\frac{1}{m})$ with $m > 1$ (it cannot be satisfied for $m < 1$) to obtain

$$H = 2\sqrt{\frac{1-\overline{m}}{\overline{m}}}\ nd\left(\frac{w}{2}\frac{1}{\sqrt{\bar{m}}}|\bar{m}\right), \quad \bar{m} < 1, \tag{2.75}$$

$$\cos\Phi_0(x) = 2\ cd^2\left(x\frac{1}{\sqrt{\bar{m}}}|\bar{m}\right) - 1, \tag{2.76}$$

$$\sin\Phi_0(x) = 2\ \sqrt{1-\bar{m}}\ cd\left(x\frac{1}{\sqrt{\bar{m}}}|\bar{m}\right)\ sd\left(x\frac{1}{\sqrt{\bar{m}}}|\bar{m}\right). \tag{2.77}$$

The branches II and III were obtained from Eqs. (2.67,2.68) by assuming that the modulus $m > 1$ and putting $\bar{m} = \frac{1}{m}$. The expressions (2.69) and (2.72) can both be written in the form

$$H = 2\sqrt{m}\ cn(\frac{w}{2}|m), \quad 0 \leq m < \infty. \tag{2.78}$$

In this case branch II is described by Eq. (2.78) at $m \geq 1$ which reduces to (2.73) by using the transformation formulas (see Ref. [2]) when the modulus is greater than unity. Again for large w, $H(m)$ is strongly oscillating, even though it remains always positive.

In Fig. 2.11 we plot the fluxon content N_f, at $I = 0$ for three lengths, that show different patterns and evolution and the introduction of multiple solutions with length. In the first row we plot the magnetic field (H vs m) and we see that for the same H we have different flux.

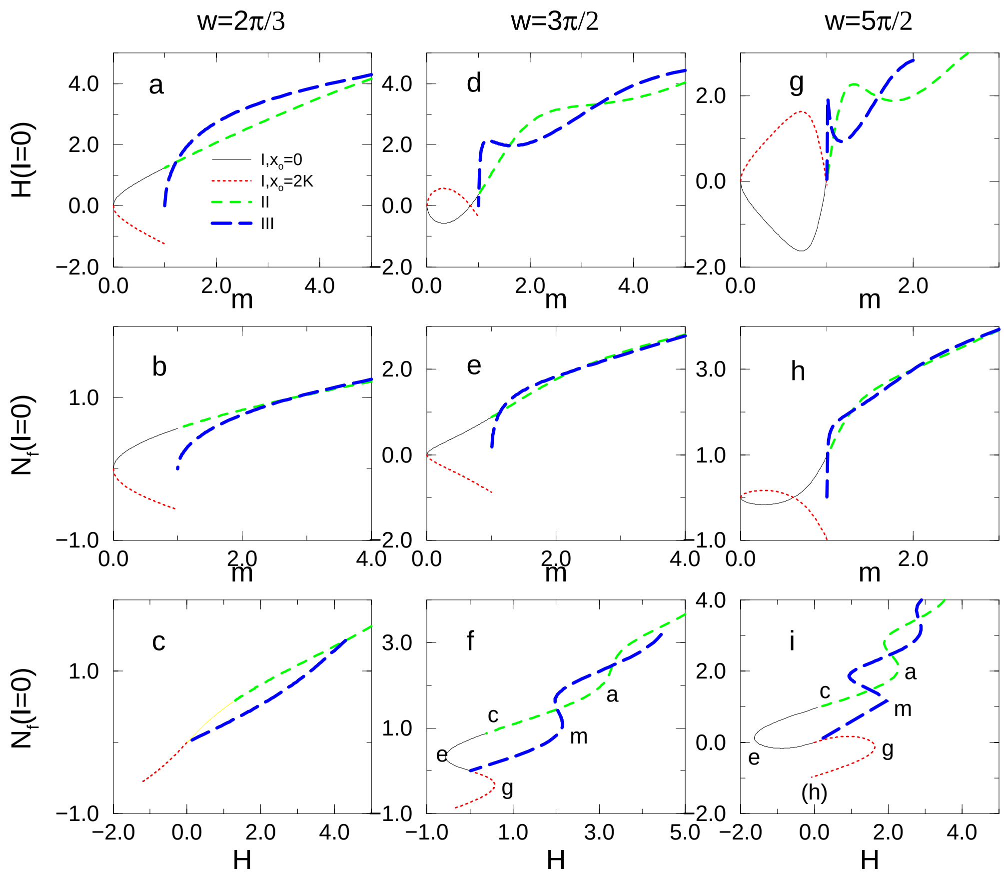

Figure 2.11: Plots of H vs m (top figures) and of the fluxon content N_f for $I = 0$ as a function of m (middle figures) and H (bottom figures), for a junction of length $w = \frac{2\pi}{3}$, (a),(b),(c), $\frac{3\pi}{2}$, (d),(e),(f), $\frac{5\pi}{2}$, (g),(h),(i).

This means that they correspond to different solutions with different screening currents. Comparing the second and the third rows we see that the modulus m (at zero current) is a much better parameter than the magnetic field H to characterize the solutions, since the flux in this case is unique except for a symmetry multiplicity. Also notice that the curves should be symmetric about the horizontal at the zero level (two x_0 values), but the plot is not completed to keep the vertical scale shorter and avoid optical complexity to the eye. Only for branch I we show both curves (for $x_0 = 0$ and $x_0 = 2K$). On the other hand the magnetic field plots exhibit some interesting changes of slope which for very long junctions alternatively correspond to stable and unstable regions of solutions. The change of slope is especially apparent for $w = \frac{5\pi}{2}$ but the alternation of stable and unstable regions also exists for small lengths as will be discussed later.

Notice that at the points of slope change the fluxon content is an integer for both branches II (light dashed) and III (dark dashed). Actually for stronger H the curves in Fig. 2.11i will look just like in 2.11c. Notice also that the symmetry in figures (b),(e),(h) will correspond to an antisymmetric form in the plot of flux (N_f) with H. The oscillatory form of flux vs H is understood by looking at the relation of H and m as plotted in (a),(d) and (g) for the three lengths. Notice the evolution with the creation of lobes for small m, whose number will increase with w as discussed. In the $w = \frac{5\pi}{2}$ case we also have extra solutions with m fixed which are not shown in the plot, but will be discussed in what follows. Also for higher w the N_f plot becomes more complex and as a particular case we discuss the $w = 10$ length in the next subsection.

2.12.2 Magnetic flux for $w = 10$

In Fig. 2.12 we plot the fluxon content N_f, for a junction length $w = 10$, at zero current as a function of, the magnetic field H in (a) and equivalently the modulus m in (b). We see that the plot in (b) is essentially single valued, while the two curves correspond to the choices $x_0 = 0$ and $x_0 = 2K(m)$ (of branch I), which give solutions with opposite flux. The corresponding plot with H is quite deformed (due to the periodic relation between H and the modulus m). In the plots the lines are the results of the analytic solutions and the symbols the numerical simula-

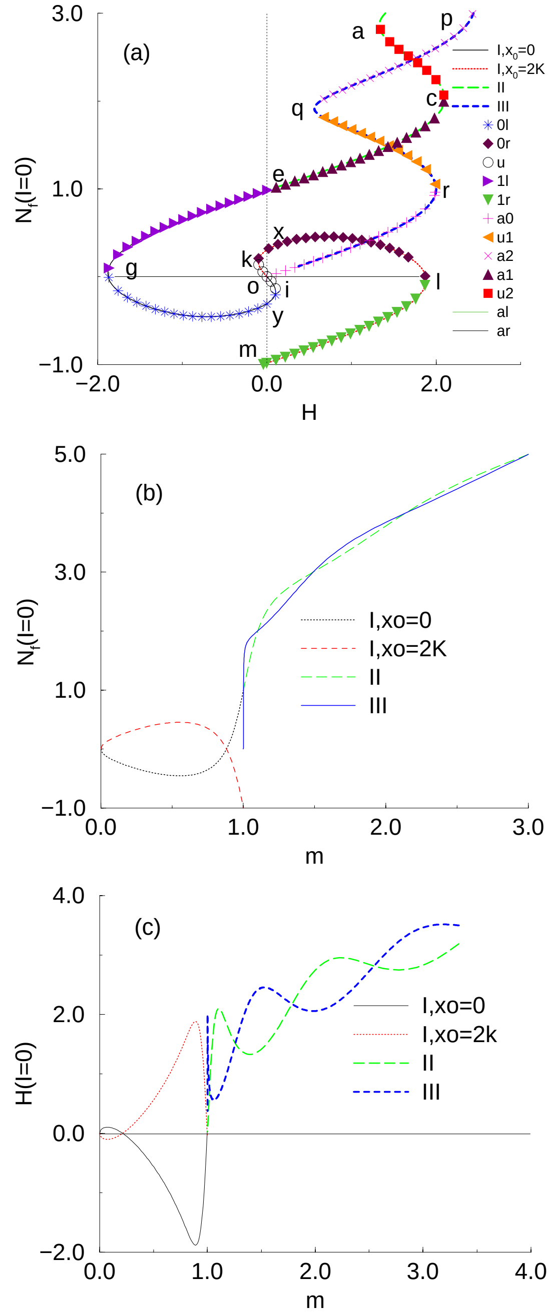

Figure 2.12: Plot of the fluxon content N_f for $I = 0$ and $w = 10$ as a function of (a) H and (b) m. In (c) we give $H(m)$.

tion results. In the second case we have to try different runs to complete the curve. As we see the plot of N_f vs m can be continuously traced by varying the modulus m in the analytic solutions. Then one can obtain the magnetic field H from m using analytic expressions (shown in Fig. 2.12c) and also trace the curve in (a). When, however you do numerical simulations, using the magnetic field as a varying parameter, you can trace only the part of the curve with the same slope. When you reach an extremum in the magnetic field (see points g, l, i, k, r, q, $\cdots$ in Fig. 2.12a), where the slope becomes infinite, the iteration procedure for the branch continuation with increase of H does not converge. Then you must decrease the value for H to trace the negative slope curve. Thus one needs five tracings back and forth in H to obtain all the solutions of branch I, i.e. the curves $0l$, $0r$, u, $1l$, $1r$ in Fig. 2.12a.

In Fig. 2.12 we show all three branches : branch I as given by the curves $o - i - g - e$ for $x_0 = 0$ (solid line) and $o - k - l - m$) for $x_0 = 2K(m)$ (dotted line); branch II is given by the line $e - c - a - \cdots$ (long dashed line); and branch III is given by the line $o - r - q - p \cdots$ (dashed line). Near H=0 for I=0 we have several solutions four of which have the same fluxon content $N_f = 0$, i.e. al, ar, $a0$, u, and four with different N_f at points e, m, x and y, i.e. $1l$, $1r$, $0l$, $0r$. Notice that the point e is slightly to the right of the N_f axis. This is because, for the particular value of $w = 10$ near $m = 1$, the $cn(\frac{w}{2}, 1)$ elliptic function behaves like $\mathrm{sech}(\frac{w}{2})$ so that for large w it is small and positive.

When we increase the current I and fix $H = 0$, the points x, y of Fig. 2.12, will give us the curves $0r$ and $0l$ in Fig. 2.9b for the flux. The corresponding points in the neighborhood of e and m will give us the curves $1l$ and $1r$ in Fig. 2.12. At the point o there are two solutions with constant m, i.e. al, ar in Fig. 2.12a (which for $H = 0$ are part of the curve $N_f = 0$). With increasing current one of them (i.e. al) reaches the maximum current at point A in Fig. 2.9b with $I = 2.5$. The other (i.e. ar) goes to B in Fig. 2.9b with $I \approx 4.0$. These solutions have $m = 0.88299$ where $cn(w|m)$ for the given w vanishes. They have opposite flux because they correspond to the two possible values of $x_0 = -K(m), K(m)$. They are equivalent to the solutions in the middle point with $I = 0$ in Fig. 2.7b. In the point o there are two more solutions from which one belongs to the stable branch $o - r$ (i.e. $a0$) and the other to the unstable branch $i - o - k$ (i.e. u) in Fig. 2.12a.

2.12.3 Fixed m solutions

The first branch (I) has also solutions with fixed $m = m^* = 0.88299$ if $w > 2\pi$. The value of m^* is obtained from the condition $\frac{w}{2} = 2K(m^*)$, so that we have an integer number of periods $(4K(m))$ for the elliptic function in the junction length w. This automatically satisfies the symmetry requirement for the boundary conditions. The magnetic field is determined from the position phase parameter x_o (with H a periodic function of x_o with period $4K(m^*) = w$). It is given by

$$H = 2\sqrt{m^*}cn(x_o + 2K(m^*)|m^*)$$

and is presented in Fig. 2.13 for $w = 10$. The maximum value of H for this branch is $H = 1.8$ at $x_o = \pm 2K(m^*)$. The two signs correspond to the al and ar curves. Notice that these solutions at zero current have zero fluxon content ($N_f = 0$) over the whole extent of the magnetic field for which they exist. These solutions also exist for $w = \frac{5}{2}\pi$, but are not shown in Fig. 2.11h, i. For larger w we expect more pairs of solutions, i.e. a pair for each increase of w by 2π. Thus for $4\pi < w < 6\pi$ there are two pairs of solutions.

2.12.4 Maximum tunneling current

In Fig. 2.14 we plot the maximum tunneling current as a function of the magnetic field for the three different lengths. We see that for $w = \frac{2\pi}{3}$ there are two curves (like a_0 and u_0 in (a)) for the maximum current, one of which is stable and the other unstable. There are, however, abrupt variations of the maximum current. Thus at the end of the stable (0-1) branch (line $a - b$) there is an unstable (1-2) branch (line c-d), which however has a discontinuity at about $H = 3.3$ in I_{max} (see vertical arrow). The same happens at the left of the stable (1,2) branch $d - n - c - m$ where its continuation has a discontinuity of 0.4 in I_{max}, at about $H = 2.6$. We see that at the I_{max} there are two curves superimposed with the same I_{max} but they start from different solutions at $I = 0$. Thus one has to be very careful when tracing numerically the I_{max} vs H curve. For intermediate current values ($I < I_{max}$ at a fixed H) you must check to the right of c which solution branch you follow. Thus if we trace for the I_{max} the stable branch at $I = 0$ from $H = 0$

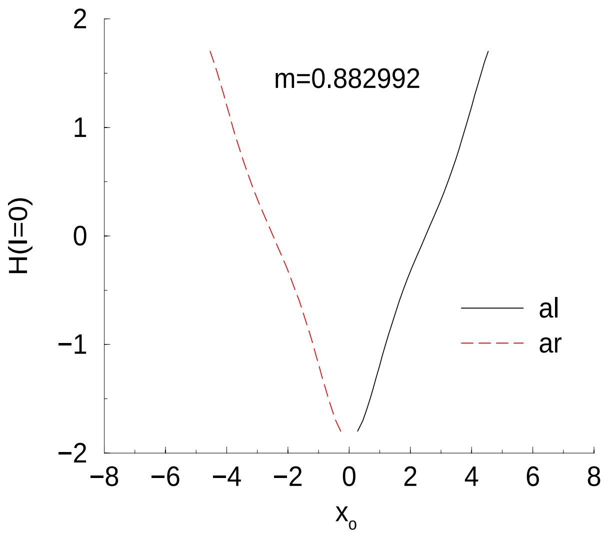

Figure 2.13: Magnetic field $H(x_0)$ at $I = 0$ for the constant $m = 0.882992$ solution.

(i.e. $\Phi_0(x) = 0$) to the right we follow the curve $a-p-b-c-n-d\ \cdots$, while if we start from the unstable branch at $H = 0$ (i.e. $\Phi_0(x) = \pi$) we follow the curve $a - p - m - c - n - d \cdots$.

The plot for $w = \frac{3\pi}{2}$ (Fig. 2.14b) is a bit more complicated. This to some extend is caused by the loops in Fig. 2.11d. Thus when we trace from $H = 3.0$ to the left, we follow the curve $a - b - c$ with a jump to d then $d - f - e - f - g - f - h$, followed by a jump to a point symmetric to c and from then on following a symmetric path which is not shown in the figure. The corresponding path for $w = \frac{5\pi}{2}$ (Fig. 2.14c) is $a - b - c$ with a jump to d then $e - f - g$, to h and from there on a symmetric curve. Notice that in this case, the extra branch $e - f - g$ has a lower peak current from the previous cases.

In the above I_{max} diagrams the existence of jumps as we scan the magnetic field and increasing the I value (at fixed H) implies a dependence of the final solution at I_{max} on the initial condition and the path of approaching it. This becomes clear if we connect it with the morphology of the I and H contours in Fig. 2.6 for the case $w = 3\pi/2$.

As we see there are four paths to reach the point f (notice corre-

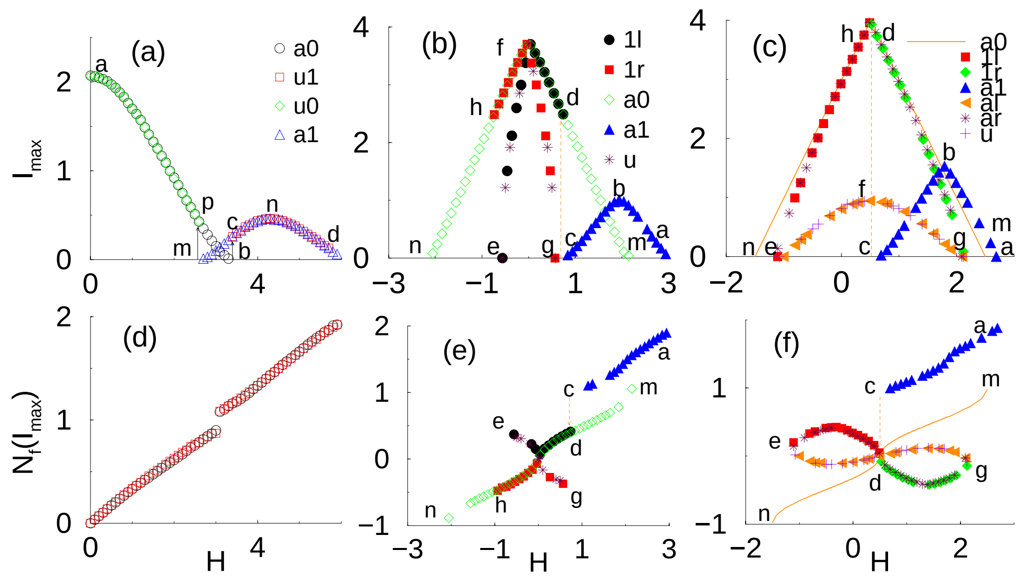

Figure 2.14: Maximum tunneling current as a function of H for three different lengths (a) $w = \frac{2\pi}{3}$, (b) $w = \frac{3\pi}{2}$, (c) $w = \frac{5\pi}{2}$ and N_f vs H at the maximum current (d),(e),(f) correspondingly for the three lengths.

sponding points in both Figs. 2.6 and 2.14b) if we fix $H = 0$ while increasing the current. These paths are along the curves $x_0 = 3K(m)$ (which is equivalent to $-K(m)$) and the vertical line $m = m^* = 0.84$. From these only the one from the right of f along $x_0 = 3K(m)$ (up to $m = 1$) is stable. This corresponds to the solution a_0. The other three paths will give solutions u, $1l$, and $1r$. The last two are along the vertical line and u along $x_0 = 3K(m)$ from O to f. Notice that the whole vertical axis (i.e. $m = 0$) corresponds to the single point ($H = 0$, $I = 0$) in the I-H diagram.

From the contours of H around the points e and g it is clear that at these points we have extrema of H which also fall on the curves $x_0 = 4K(m)$ and $x_0 = 2K(m)$ where $I = 0$. Let us take another look in Fig. 2.14b. If we start from the point a (with $N_f = 2$) by decreasing H at $I = 0$ we reach the point c (with $N_f = 1$) along the line $x_0 = 0$ (i.e. branch II) in Fig. 2.6. The continuation of branch II through $m < 1$ is branch I which goes up to point e in Fig. 2.14b. In the rest of the curve, i.e. when m goes from e to O, the magnetic field is reversed from -0.6 (at e) to zero. The range in H from c to m corresponds to two different paths in the $x_0 - m$ diagram. From the topology it is clear that they end up in different maximum current as H is kept constant. The path mc (above m) has its maximum current to the left of the line, while the path cm (i.e. below m) has its maximum current to its right. Notice that in Fig. 2.14b, in going from a to c (along branch II) you cross the H value at m. The corresponding point in the x_0-m diagram is a different one (m') on the m-axis between a and c. Finally the point b can be reached from several paths. A similar analysis can be given in all cases, but we chose a single length as a point of illustration.

Below each case in Fig. 2.14 we plot the corresponding flux vs H at the maximum current. These curves resemble the ones at zero current in Fig. 2.11(c, f, i). One remark is that while at $I = 0$ the N_f vs H is a continuous curve, at I_{max} the flux shows discontinuities the same way that the maximum current was discontinuous. Comparing Figs. 2.11f and 2.11e we see that the branches om (o being the origin) and ca are only slightly modified. The branch though $e - c$ (in Fig. 2.11f) is folded onto $e - o - d$ (in Fig 2.14e). The same happens for $w = \frac{5\pi}{2}$ between Figs. 2.11i and 10f. In the plot for the flux we have not plotted all the branches. For a more complete plot of the branch II and III solutions see the case $w = 10$ in Fig 2.15 since they have the same approximate structure.

In Fig. 2.15a we show the maximum tunneling current and the flux (at I_{max}) as a function of the magnetic field, for $w = 10$. At this length we are already at the limit of long length branches. In this case when going from right to left we trace the I_{max} through the points $a-b-c-d-e$, jump to $f-g-h-i-j-k-l-m$ with a symmetric continuation. The flux (Fig. 2.15b) also shows a similar folding as for the case $w = \frac{5\pi}{2}$. The letters correspond to the ones in I_{max} vs H plot.

2.13 Analytical stability analysis

Next we obtain some analytic estimates for the stability regions for the zero current solution. The observations obtained by these estimates will verify and extend our results by solving numerically the stability eigenvalue problem in (2.55). Substituting Eq. (2.48) into Eq. (2.55) we obtain the Lamé eqn.

$$-X'' + \left[2m\ sn^2(x + x_0|m) - 1\right] X = \lambda\ X. \tag{2.79}$$

Numerical solution of (2.79) with the boundary conditions in (2.56) gives us all the eigenvalues and we can check the stability of the static solution. One can gain some insight into a necessary bound for stability from the following analytic considerations, which we also compare with the numerical results.

Let us remark that for three values of $\lambda = m-1, 0, m$ we can give an explicit analytic form for the corresponding solutions of (2.79), which are

$$X_0 = dn(x + x_0|m),\ \ \lambda_0 = m - 1, \tag{2.80}$$

$$X_1 = cn(x + x_0|m),\ \ \lambda_1 = 0, \tag{2.81}$$

$$X_2 = sn(x + x_0|m),\ \ \lambda_2 = m, \tag{2.82}$$

while other eigenfunctions of Eq. (2.79) have much more complicated forms. It is worth stressing that the functions in (2.80,2.81,2.82) cannot be called eigenfunctions of our problem in (2.55)-(2.56), because they do not satisfy the boundary conditions (2.56). Taking now into account

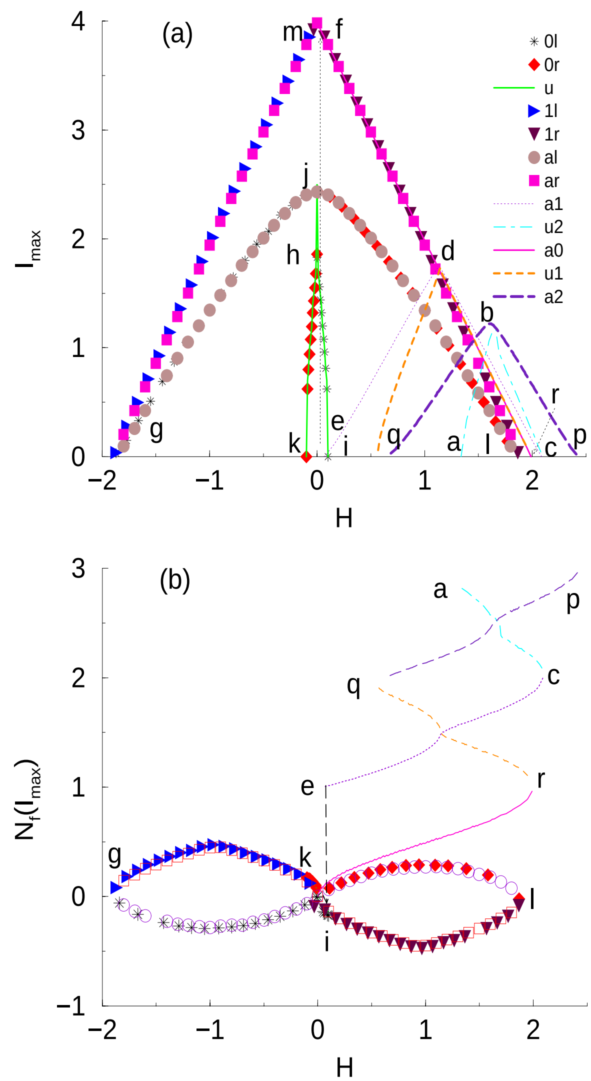

Figure 2.15: The same as Fig. 10 for $w = 10$. (a) $I_{max}(H)$, (b) $N_f(H)$ at $I = I_{max}$.

Eq. (2.56) we can find the curves of neutral stability, i.e. the critical relationship between parameters (w and H or I in our case) when the problem (2.55)-(2.56) has an eigenvalue $\lambda = 0$.

In the following we shall examine the implications of the above three analytic eigenfunctions on the stability of the static solution. We must bear in mind though that it is not sufficient that one of the three above eigenvalues is zero or negative, but on top we must satisfy the boundary conditions. Even in that case we can prove instability but not the reverse, which can only be done by numerical solution of the eigenvalue problem. We will see, however that some of the conclusions will be very useful. We will examine the situation for each of the three branches separately.

Ist branch: In this case it is not easy to get analytical estimates. We do not have an extra neutral stability since $m < 1$ and in any case it can be considered as a continuation of branch II.

IInd branch: In this case the three eigenfunctions of interest are

$$X_0 = cn\left[\sqrt{m}\ x|\frac{1}{m}\right],\ \ \lambda_0 = m - 1\ >\ 0, \tag{2.83}$$

$$X_1 = dn\left[\sqrt{m}\ x\ |\frac{1}{m}\right] = dn\left[\frac{x}{\sqrt{\bar{m}}}|\bar{m}\right],\ \ \lambda_1 = 0, \tag{2.84}$$

$$X_2 = sn\left[\sqrt{m}x|\frac{1}{m}\right],\ \ \lambda_2 = m > 0. \tag{2.85}$$

Again, since $m > 1$ only X_1 is of interest. It is an eigenfunction of the linearized problem if

$$sn\left(\frac{w}{\sqrt{\bar{m}}}|\bar{m}\right) = 0 \tag{2.86}$$

or equivalently if

$$\frac{w}{\sqrt{\bar{m}}} = 2\ j\ K(\bar{m}),\quad j = 1, 2, \cdots. \tag{2.87}$$

Substituting (2.87) into (2.72) we get two families of curves of neutral stability, where again we can distinguish two cases for even ($j = 2n$) and odd ($j = 2n + 1$) values of j. For even j we have $N_f = 2n + 1$ and for odd $N_f = 2n$, i.e. odd and even number of fluxons correspondingly. The respective values of w are given by

$$w = \frac{8}{H} n K \left(\frac{4}{H^2}\right), \ N_f = 2n \quad , \text{ with } n = 0, 1, \cdots \tag{2.88}$$

$$w = \frac{2(2n+1)}{\sqrt{1+\frac{H^2}{4}}} K \left(\frac{1}{1+\frac{H^2}{4}}\right), \quad N_f = 2n+1 \quad , \text{ with } n = 0, 1, \cdots . \tag{2.89}$$

IIIrd branch: In this case $m > 1$ and we can write the eigenfunctions in the following form

$$X_0 = cn \left[\sqrt{m}(x+x_0)|\frac{1}{m}\right], \ \lambda_0 = m - 1 > 0,$$

$$X_1 = dn \left[\sqrt{m}(x+x_0)|\frac{1}{m}\right] = \frac{\sqrt{1-\frac{1}{m}}}{dn\left[\sqrt{m}\ x|\frac{1}{m}\right]} = \frac{\sqrt{1-\bar{m}}}{dn\left[\frac{x}{\sqrt{\bar{m}}}|\bar{m}\right]}, \ \lambda_1 = 0, \tag{2.90}$$

$$X_2 = sn \left[\sqrt{m}(x+x_0)|\frac{1}{m}\right], \ \lambda_2 = m > 0$$

In (2.90) we used a standard transformation of elliptic functions so that their modulus is less than unity, and then substituted $x_0 = \sqrt{\frac{1}{m}} K(\frac{1}{m})$. We also used the notation $\bar{m} = \frac{1}{m}$. Since λ_0 and λ_2 are always positive we only need to consider X_1. For X_1 in (2.90) to be an eigenfunction of (2.55)-(2.56) we must have again the condition (2.86) or the equivalent (2.87). Here we can distinguish two cases for even ($j = 2n$) and odd ($j = 2n+1$) values of j. It can easily be verified again that for even j we have $N_f = 2n$ and for odd $N_f = 2n+1$, i.e. even and odd number of fluxons correspondingly.

Substituting Eq. (2.87) into Eq. (2.75) we obtain two families of curves of neutral stability in H, with the values of w given for $n = 1, 2, \cdots$ by

$$w = \frac{4n}{\sqrt{1+\frac{H^2}{4}}} K \left(\frac{1}{1+\frac{H^2}{4}}\right), \quad N = 2n - 1 \tag{2.91}$$

and

$$w = \frac{4}{H}(2n-1)K\left(\frac{4}{H^2}\right), \ N = 2n. \tag{2.92}$$

Eq. (2.91) is valid for any $H \geq 0$ but (2.92) only for $H \geq 2$. As we will see in the section of the numerical evaluation of stability the above families of curves will in fact compare very well giving the boundaries of stability.

2.13.1 Numerical stability results

To check the stability of the solutions discussed and examine the validity of the analytical stability results we have calculated the eigenvalue spectrum for small oscillations around the solution $\Phi_0(x)$. In Fig. 2.16 we plot the four lowest eigenvalues of Eq. (2.55) for $w = 10$ and $I = 0$ as a function of the parameter m for the I and II (Fig. 2.16a) and the III branch (Fig. 2.16b) correspondingly. Stability requires all eigenvalues to be positive while an increasing number of negative eigenvalues denotes a higher degree of instability.

The regions in m with all positive eigenvalues correspond to the stable fluxon solutions and are separated by regions in m with unstable solutions. Often stable solutions correspond (in the plot of N_f with H) to the branches with positive slope, line ec, etc in branch II of Fig. 2.12 or qp, etc in branch III. This is not the case though of small w (see Fig. 2.11) or strong magnetic fields. All the solutions in branch I ($m < 1$) are unstable, with several eigenvalues being negative. In all cases as expected the lowest mode has no nodes and is symmetric. It can have however several lobes, reflecting the number of fluxons that show in the unperturbed solution $\Phi_0(x)$. Also when a higher mode eigenvalue vanishes the lowest mode reflects this and reforms by creating more lobes, and this effect can be strong when eigenvalues cross each other. In comparing Figs. 2.16a and b we see that the regions of stable solutions in m for branch II are regions of unstable solutions for branch III, while the bounding values of m are the same in both cases. This is consistent with the analytic expressions (26) and (28). Of course they correspond to different solutions due to different x_0. In branches II and III there are at most two negative eigenvalues, while in branch I [$m < 1$ in (2.82)] there is a region with four negative eigenvalues.

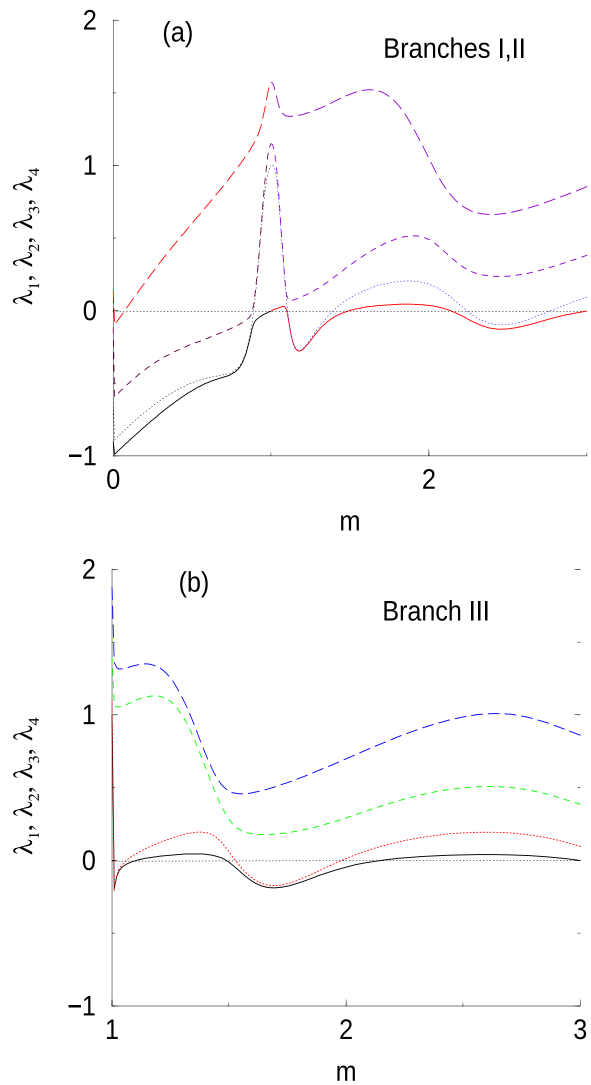

Figure 2.16: Plot of four lowest eigenvalues as a function of m for (a) branches I and II and (b) branch III.

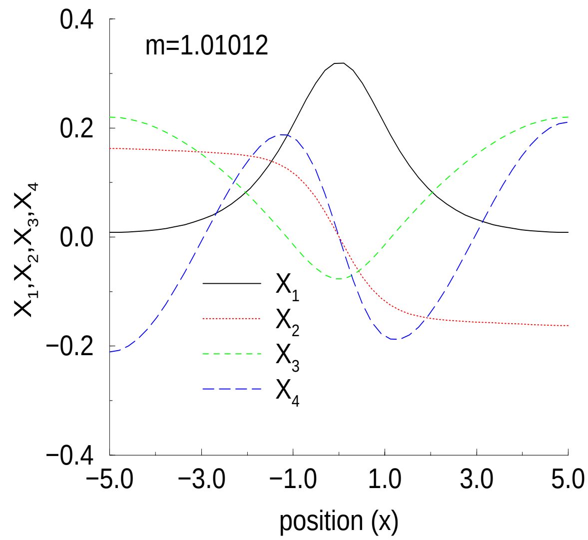

Figure 2.17: Plot of four lowest eigenmodes for $m = 1.01012$ of branch II.

The analytic formulas for stability are entirely consistent for the points in m where instability sets in. In fact in Fig. 2.17 we show the four lowest eigenvectors for $m = 1.01012$ where $\lambda_1 = 0$. The corresponding eigenvector is fitted with equation (25) and as expected for $m \approx 1$ the dn function behaves like a sech$(\sqrt{m}x)$. The same is true for the branch III, where the lowest mode can be fitted well with (31).

In Fig. 2.18 we plot in the m vs w diagram the lines from conditions (2.87), so that each line corresponds to solutions with an integer fluxon number. Thus the range of m values between two lines for a given w corresponds to the $(j, j+1)$ branch of both II and III cases. In Fig. 2.19 we plot the same information but in an H vs w plot for II (Fig. 2.19a) and III (Fig. 2.19b). Due to the oscillatory relation of H and m the extrema of the magnetic field at $I = 0$ for each branch do not exactly coincide with the stability boundary lines. This means that the branch ends on these lines but in the intermediate it might reach H values slightly outside this range. If viewed as a function of w for a fixed m (or $\bar{m}$) then the corresponding magnetic field varies periodically, with a period in w equal to $4\sqrt{\bar{m}}K(\bar{m})$, i.e. for each m it covers the $w-$values

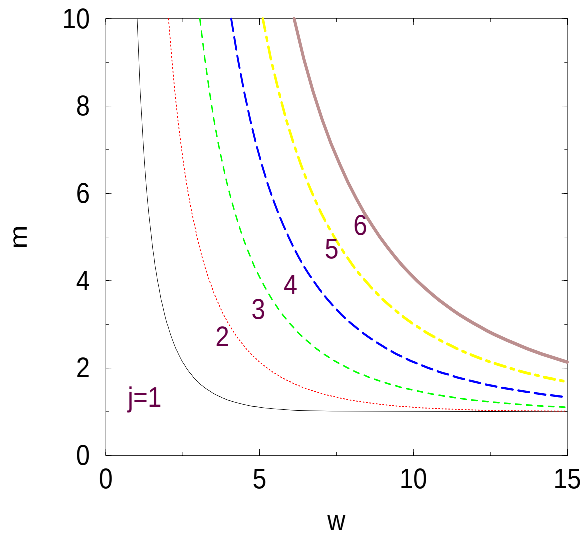

Figure 2.18: Plot of the neutral stability lines of integer N_f in an m vs w diagram.

between every other curve ($\Delta j = 2$). We also notice from Fig. 2.19 that the width in H of the (0,1) branch is almost independent of w for large w, while for $w \to \infty$ many branches tend to coalesce in the same interval of H for both II and III. One can understand this case by using the pendulum analogy and realize that for large w the solutions correspond to trajectories that pass near the separatrix points. This can also be seen from (2.75). In order to satisfy the boundary condition for $w \to \infty$, the important values of $\bar{m}$ are quite close to $\bar{m} \approx 1$, since in that case $K(\bar{m}) \to \infty$. On the other hand for high magnetic fields $H \to \infty$ the corresponding values of $\bar{m}$ are near zero.

2.14 Experimental Relevance

In this section we relate some of our theoretical and numerical results to the experimental techniques and data. Since the behavior of the maximum tunnel current is of importance for junction characterization, we start by plotting in Fig. 2.20 the numerically estimated (using the iteration procedure described in section 4.2) values of I_{max} for three

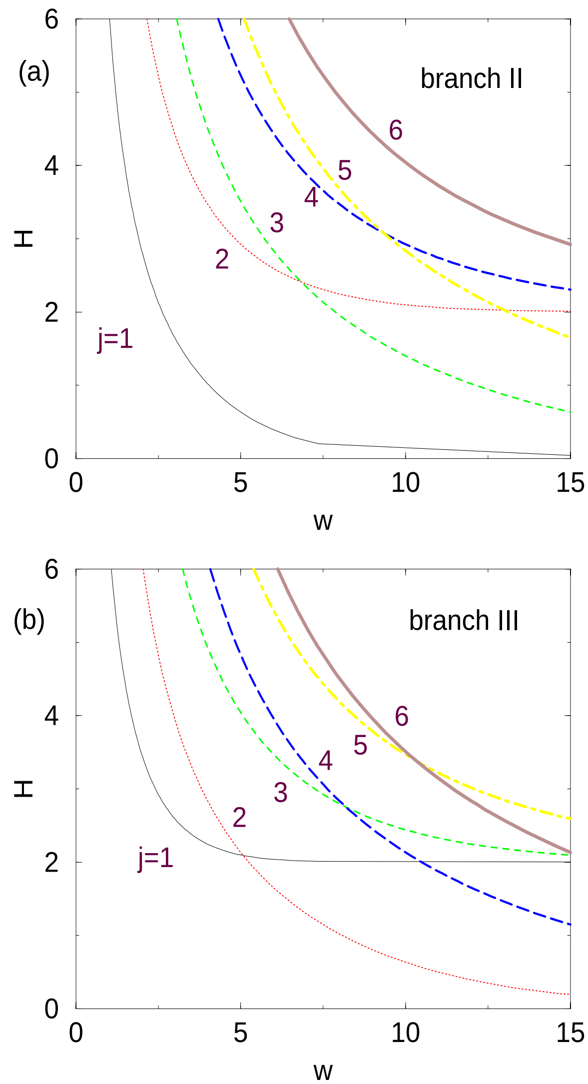

Figure 2.19: Same as Fig. 14 in an H vs w plot. (a) branch I and II and (b) branch III.

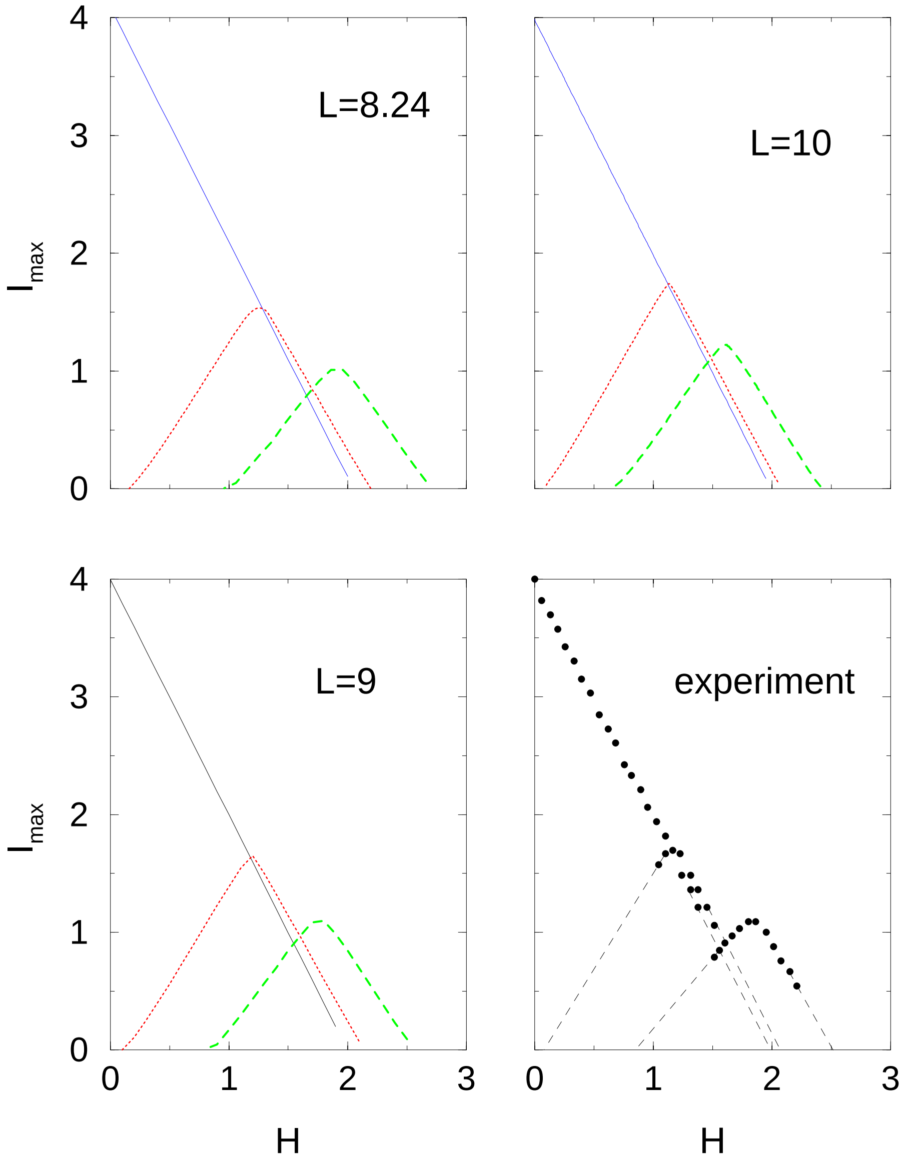

Figure 2.20: Numerical results for I_{max} vs H for $L = 8.24$, $L = 9$ and $L = 10$ and the experimental data from [14]. In the experimental data the dots (.) are the measured points and the dashed lines should only be considered as a guide for the eye.

different lengths (8.24, 9 and 10) and the associated experimental data extracted from figure 5.10 in [14]. The best fitting seems to be for $L = 9.0$, i.e. slightly different from $L = 8.24$, as was determined by analysis of the experimental data. The discrepancy is due to the fact that the critical current density is not homogeneous in the experimental sample and the analysis used in the experiment it would be valid for a larger length junction. An exact knowledge of the inhomogeneity can give a more accurate profile.

Besides the relatively good agreement of the maximum current I_{max} value for each H, that verifies our numerical and theoretical analysis we can also make the following observations: The experimental data for I_{max} seems to try to follow the stable branches. After crossing of I_{max} lines it seems to approach some "bifurcation" points where it becomes easy to fall in another branch, but a careful experimental quasistatic scanning of the magnetic field and current (as was done in the numerical simulations used to obtain the displayed data), will enable to successfully trace the whole stable branch experimentally. Then one can pass over these 'fuzzy' bifurcation points and be able to select the appropriate continuation branch. To work within a given branch with low I_{max} is of interest for low energy (or current) devices. The quasistatic scanning will also help to elucidate the physical nature and the practical consequences of such bifurcation points.

There is a close relation between the experimental and the computer simulation methodologies for determining the whole I_{max} line of a device. One of these methodologies is described (as a numerical scheme) in [24, 23]. It is based on the failure of the convergence of the associated iteration method when the bias current exceeds the maximum valued. We should mark that in this case one has to solve a large set of PDE problems associated with continuation points on the I_{max} line through fine tuning of I and H along the boundary line. This requires significant amounts of computer power since it is prone to the effect of hysteresis. A similar approach is used in experiments. In this case tracing I_{max} corresponds in configuring the device on the border line of the branch. Specifically slightly higher bias currents switch the device from the pair tunneling to quasiparticle mode. A similar approach (used here) is to configure the device so it corresponds to a point on the H-axis (I=0) and slightly increase the current until the above mode switch will be detected. It is possible but not easy to realize such "initial configuration". For both cases one has to introduce some initial flux configuration.

The main difficulty that arises from the hysteretic behavior can be avoided if one looks at Fig. 2.21 where we replot Fig. 2.6 but with a rescaling of the vertical axis by $K(m)$, so that the curves $x_0 = K(m)$ now become horizontal lines. As we mentioned earlier the parameters x_0 and m define uniquely the fluxon distribution of the solutions. So the area enclosed by the curve through the points a, b, and c (with upper half $I > 0$ and lower half $I < 0$) is the stable region corresponding to the $(1-2)$ branch in the $I_{max}(H)$ diagram (see the corresponding a, b and c points). It is actually separated from the other stable regions. One can go however from one stable region to the next, by moving quasistatically along the $x_0 = K$ line.

Then it is clear that for an experiment one might select the starting configuration of his choice and follow an appropriate path quasistatically to another stable region and to the maximum current so that the whole procedure is convenient. Note that keeping H (or I) constant corresponds on walking on a particular contour line.

For the procedure described above where the H is increased or decreased monotonically the scanning in the $I - H$ plane suffers from strong hysteretic phenomena that are apparent in both the computer simulations and the actual experiments. Based on the analysis presented in this chapter an alternative way free of such phenomena can be very naturally proposed. Specifically, as seen in Section 2.12.2 (see in particular Figs. 8a-c) one might consider searching for the I_{max} on the $I - N_f$ plane where it is mostly singled valued. The search methodology will remain the same as before and therefore it can be easily done on computer simulations by making simple modification on the existing software. Nevertheless it is not clear how this can be done experimentally since it requires a manipulation of both the current and the external field. Another way to keep the flux constant and this can be done by applying a non-constant magnetic field that varies trying to keep the distance between the fluxons constant. It remains to be seen how easily this can be done in practice.

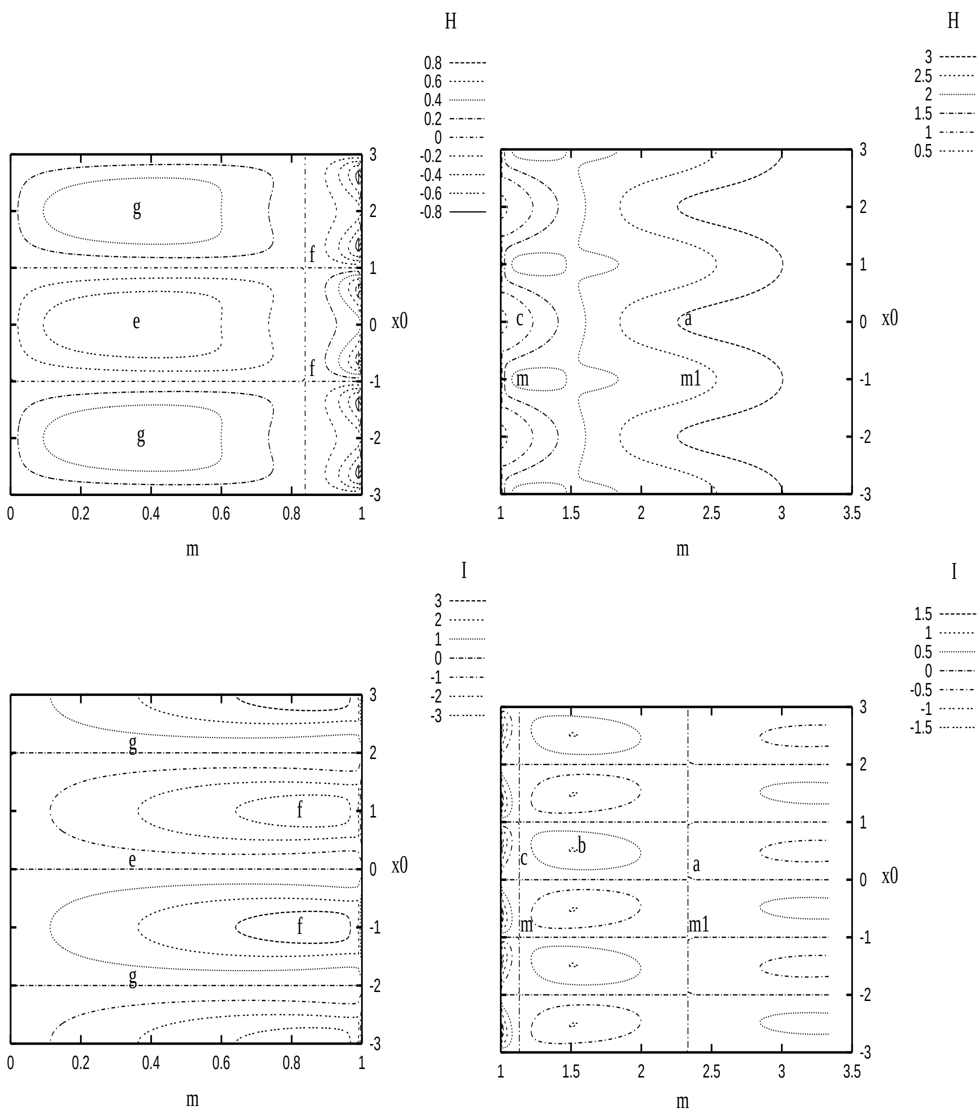

Figure 2.21: Constant H and I contours in the $(m,\, x_0/K(m))$ plane.

2.15 Discussion

In the preceding sections we have presented a theoretical, numerical and experimental study of the various static solutions of 1-D Josephson junctions. Our basic approach was the use of elliptic functions to analytically express the solutions of the associated sine–Gordon equation. The two parameters involved in the elliptic functions (m and x_0) were properly selected based on the particular form of the boundary conditions. This let us obtain useful analytic expressions for these solutions in particular for the cases of zero magnetic field $H = 0$ or zero current $I = 0$. Their importance lays in the fact that one can easily study their stability by using simple linear perturbations. This simplicity in the stability analysis let us exploit the role of the geometric (w) and physical parameters (H, I, N_f) involved. A significant outcome of our study is the fact that the module (m) of the elliptic functions is a good characterization parameter that greatly simplifies the general qualitative and quantitative pictures of the various solutions. The use of m as a characterization parameter also leads to more stable, accurate and efficient numerical algorithms used to study various aspects of Josephson junctions.

The analysis presented above is particularly useful to understand the sometimes complicated behavior when we try to follow numerically the different branches. In fact, this was one of the motivations behind this work. Some the most common, annoying problems encountered (even in the case where no defects are present) are the following: Considering bifurcation points as regular point and vice versa, missing bifurcation points, viewing certain turning or bifurcation points as limiting points and improper branch switching (e.g. 2π jumps). The present study gives several hints to help us overcome these difficulties.

Our original goal was the study of the influence of the critical current density ($J_c \rightarrow J_c(x)$) inhomogeneities on the tunneling current I_{max}. Two observations, however, made necessary to study the perfect junction:

(a) We noticed that when studying window junctions, even for zero magnetic field, the maximum current starting with different initial conditions, was not always the same i.e. at $I_{max} = 4.0$. Several times it stopped at lower values.

(b) Both numerical and experimental results show strong hysteresis phenomena with jumps between different branches when varying the external magnetic field. Related to this, the question arises whether there exists a way of analytic continuation between different branches? Or in more physical terms whether there is a physical parameter (in the place of H) whose smooth variation shows no hysteresis in I_{max}.

With respect to point (a), it is clear now that the second value belongs to one of the unstable branches we discussed for $w = 10$. If, however, there are defects in the junction the unstable solutions might also become stable and therefore are of interest [4]. Another way to stabilize solutions is by high frequency fluctuations (of small amplitude) in a way similar to the Kapitza inverse pendulum problem [61]. This can also be achieved by small wavelength spatial variation of the critical current density [55]. For remark (b) in the undefected $1-d$ junction one has the advantage that the analytic solution is known and the choice of m and x_o, pin uniquely the proper solution. Thus one can follow, smoothly the solution if we look at I_{max} as a function of the magnetic flux. This way we can avoid hysteresis by choosing a proper initial condition at $I = 0$ and increase I to I_{max}.

If, however, one uses the magnetic field as an input parameter, strong hysteretic phenomena are observed, due to the non uniqueness of the relation between H and m for large w. The multiple solutions (for fixed x_o due to symmetry) correspond to different fluxon content. This non-uniqueness will disappear for large H where in fact the junction behaves as if it is a short one and you recover the diffraction like pattern. Also an increase of the temperature makes the junction to behave as a short one, with non-overlapping branches.

Chapter 3

Critical currents in Josephson junctions with macroscopic defects

3.1 Introduction

The interaction of localized magnetic flux (fluxons) with defects (natural or artificial) or impurities in superconductors or junctions has an important effect in the properties of bulk superconductors or the behavior of Josephson junctions correspondingly [1]. The flux trapping from defects which is of major importance in Josephson junctions [14] can modify the properties of polycrystalline materials with physical dislocations, for example grain boundary junctions [29]. In this category one can also consider grain boundary junctions in $YBa_2Cu_3O_7$ [79] where the tunneling current is a strongly varying function along the boundary. This strong inhomogeneity makes them good candidates for SQUID type structures [40]. Phenomenologically the current-voltage characteristics of grain boundary junctions are well described [39] by the resistively shunted junction model [67]. The grain boundary lines often tend to curve, while the junction is very inhomogeneous and contains nonsuperconducting impurities and facets of different length scales[69, 8]. The linear increase of the critical current with length in grain boundary junctions with high-T_c superconductors, which is a different behavior from the saturation in the inline geometry of a perfect junction, can be explained by the presence of impurities[32]. Therefore it is interesting to study flux trapping in impurities especially when it can be controlled. Modern fabrication techniques can with relative ease engineer any defect configuration in an extremely controlled way.

In bulk materials are several types of defects that can influence the critical current in high temperature superconductors like $YBa_2Cu_3O_x$ materials. They include 3d inclusions, 2d grain boundaries and twin boundaries, and point defects like dopants substitutions, oxygen vacancies[1]. For example the homogeneous precipitation of fine Y_2BaCuO_5 non-superconducting particles in the melt processing of $YBa_2Cu_3O_x$ leads to high J_c values due to the particle pinning centers[72]. Similar behavior is observed in $NdBa_2Cu_3O_x$ bulk crystals with $Nd_4Ba_2Cu_2O_{10}$ particles[94]. Of interest is also the case of the peak effect in twin-free $Y123$ with oxygen deficiency. In this case, one sees a linear increase (peak effect) of the critical current at small magnetic fields, when growth is under oxygen reduction[102]. For the fully oxidized crystal one expects a decrease. The peak effect is attributed to flux trapping. Information on the defect density and activation energies can also be obtained from the I-V characteristics, as was the case for several types of defects which were also compared to Au^+ irradiated samples with artificial columnar defects[21]. These columnar defects also act to trap flux lines in an YBCO film which is considered as a network of intergrain Josephson junctions modulated by the defects. In this case assuming a distribution of contact lengths one finds a plateau in the critical current density vs. the logarithm of the field[68].

The study of long size of impurities is going to give information beyond theories which concern small amplitude of inhomogeneities [100]. Also it is possible for a direct comparison of the numerical results with experiments in long junctions obtained with electron beam lithography [59]. This is a powerful technique which allows the preparation and control of arrays of pinning centers. Another method is the ionic irradiation which produces a particular kind of disordered arrays, consisting of nanosized columnar defects [21, 98]. The variation of the critical current density can also occur due to temperature gradients [58].

The activity in the area of high critical current densities in the presence of a magnetic field is hampered by defects due to the difficulty of having a high quality junction with a very thin intermediate layer. Thus significant activity has been devoted, since for example the energy resolution of the SQUID [50] and the maximum operating frequency of the single flux quantum logic circuit [63], to name a few applications, depend inversely and directly respectively on the plasma frequency ω_p, with $\omega_p \sim J_c^{1/2}$. The fundamental response frequency of Josephson devices, the Josephson frequency ω_J, also depends on the critical current density. On the other hand, a drawback is that high critical current densities lead to large subgap leakage currents [56] and junction characteristics degrade rapidly with increasing J_c.

Variations in the critical current density also influence the $I-V$ characteristics introducing steps under the influence of both a static bias current and the irradiation with microwaves [77]. In that case the variation is quite smooth (of *sech* type), so that the fluxon and its motion could be described by a small number of collective coordinates. Interesting behavior is also seen in both the static and dynamic properties for the case of a spatially modulated J_c with the existence of "supersoliton" excitations [71, 62] and the case of columnar defects [47, 12] or disordered defects [32].

The trapping of fluxons can be seen in the $I_{max}(H)$ curves where we also expect important hysteresis phenomena when scanning the external magnetic field. The hysteresis can be due to two reasons: (i) One is due to the non-monotonic relation between flux and external magnetic field [22] arising from the induced internal currents, and (ii) from the trapping or detrapping of fluxons by defects. The effect of a defect on a fluxon and the strength of the depinning field depends strongly in the size of the defect, the type of defect and the position of the defect. Here we will consider case where the widths of the defects is of the order of the Josephson penetration depth. In this range we expect the strongest coupling between fluxons and defects. We will also consider the case of a few defects in the low magnetic field region where pinning and coercive effects are important.

The organization of the chapter is as follows. In Sec. 3.2 the sine-Gordon model for a Josephson junction is presented. In Sec. 3.3 we present the results of the critical current I_{max} versus the magnetic field of a junction with an asymmetrically positioned defect. The variation of

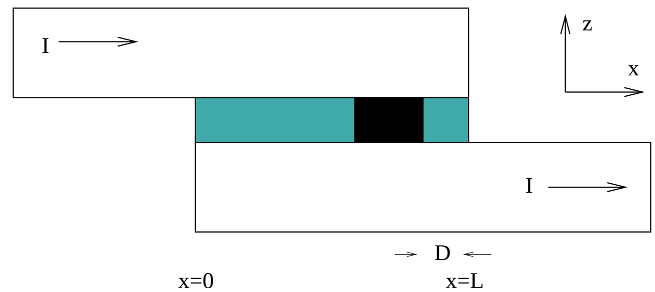

Figure 3.1: The geometry of the junction. The dark shaded region marks the defect in the intermediate layer. ℓ is the junction length and D the separation between the left edges of the defect and the junction.

the I_{max} and the flux content N_f with the defect critical current density and the position are presented in sections 3.4 and 3.5 respectively. The effect of multiple pinning centers is examined in sections 3.6 and 3.7. In Sec. 3.8 we examine a defect with a smooth variation of the critical current density. In the last section we summarize our results.

3.2 The junction geometry

The electrodynamics of a long Josephson junction is characterized from the phase difference $\phi(x)$ of the order parameter in the two superconducting regions. The spatial variation of $\phi(x)$ induces a local magnetic field given by the expression

$$\mathcal{H}(x) = \frac{d\phi(x)}{dx}. \quad , \tag{3.1}$$

in units of $H_0 = \frac{\Phi_0}{2\pi d\lambda_J}$, where Φ_0 is the quantum of flux, d is the magnetic thickness and λ_J is the Josephson penetration depth. The magnetic thickness is given by $d = 2\lambda_L + t$ where λ_L is the London penetration depth in the two superconductors and t is the oxide layer thickness. The λ_J is also taken as the unit of length. The current transport across the junction is taken to be along the z direction. We describe a 1-D junction shown in Fig. 3.1 with width w (normalized to λ_J) in the y direction, small compared to unity. The normalized length in the $x-$direction is ℓ. The superconducting phase difference $\phi(x)$ across the defected junction is then the solution of the sine-Gordon equation

$$\frac{d^2\phi(x)}{dx^2} = \widetilde{J}_c(x)\sin[\phi(x)], \tag{3.2}$$

with the inline boundary condition

$$\frac{d\phi}{dx}\Big|_{x=\pm\frac{\ell}{2}} = \pm\frac{I}{2} + H, \tag{3.3}$$

where I and H are the normalized bias current and external magnetic field. $\widetilde{J}_c(x)$ is the local critical current density which is $\widetilde{J}_c = 1$ in the homogeneous part of the junction and $\widetilde{J}_c = j_d$ in the defect. Thus the spatially varying critical current density is normalized to its value in the undefected part of the junction J_0 and the λ_J used above is given by

$$\lambda_J = \sqrt{\frac{\Phi_0}{2\pi\mu_0 d J_0}},$$

where μ_0 is the free space magnetic permeability. One can also define a spatially dependent Josephson penetration depth by introducing $\widetilde{J}_c(x)$ instead of J_0. This is a more useful quantity in the case of weak distributed defects.

In the case of overlap boundary conditions Eqs. (3.2) and (3.3) are modified as

$$\frac{d^2\phi(x)}{dx^2} = \widetilde{J}_c(x)\sin[\phi(x)] - I, \tag{3.4}$$

and

$$\frac{d\phi}{dx}\Big|_{x=\pm\frac{\ell}{2}} = H. \tag{3.5}$$

We can classify the different solutions obtained from Eq. (3.2) with their magnetic flux content

$$N_f = \frac{1}{2\pi}(\phi_R - \phi_L), \tag{3.6}$$

in units of Φ_0, where $\phi_{R(L)}$ is the value of $\phi(x)$ at the right(left) edge of the junction. Knowing the magnetic flux one can also obtain the magnetization from

$$M = \frac{2\pi}{\ell}N_f - H. \tag{3.7}$$

For the perfect junction, a quantity of interest is the critical magnetic field for flux penetration from the edges, denoted by H_{c1}. For a long junction it is equal to 2 while for a short it depends on the junction length. Due to the existence of the defect this value can be modified since we have the possibility of trapping at the defects. For a short junction we have penetration of the external field in the junction length, so that the magnetization approaches zero. For a long junction it is a non-monotonic function of the external field H.

To check the stability we consider small perturbations $u(x,t) = v(x)e^{st}$ on the static solution $\phi(x)$, and linearize the time-dependent sine-Gordon equation to obtain:

$$\frac{d^2v(x)}{dx^2} - \widetilde{J}_c(x)\cos\phi(x)v(x) = \lambda v(x), \tag{3.8}$$

under the boundary conditions

$$\frac{dv(x)}{dx}|_{x=\pm\frac{\ell}{2}} = 0,$$

where $\lambda = -s^2$. It is seen that if the eigenvalue equation has a negative eigenvalue the static solution $\phi(x)$ is unstable. There is considerable eigenvalue crossing so that we must monitor several low eigenvalues. This is especially true near the onset of instabilities.

3.3 Asymmetric defect

In the following we will consider the variation of the maximum critical current as a function of the magnetic field for several defect structures. We start with a long ($L > \lambda_J$) junction of normalized length $\ell = 10$ with a defect of length $d = 2$ which is placed $D = 1.4$ from the right edge. Thus the defect is of the order of λ_J. We plot in Fig. 3.2a the maximum critical current I_{max} variation with the magnetic field. The different curves correspond to phase distributions for which we have a maximum current at a given value of the magnetic field H. The overlapping curves called modes have different flux content as seen in Fig. 3.2b where we plot the magnetic flux in units of Φ_0 for zero current

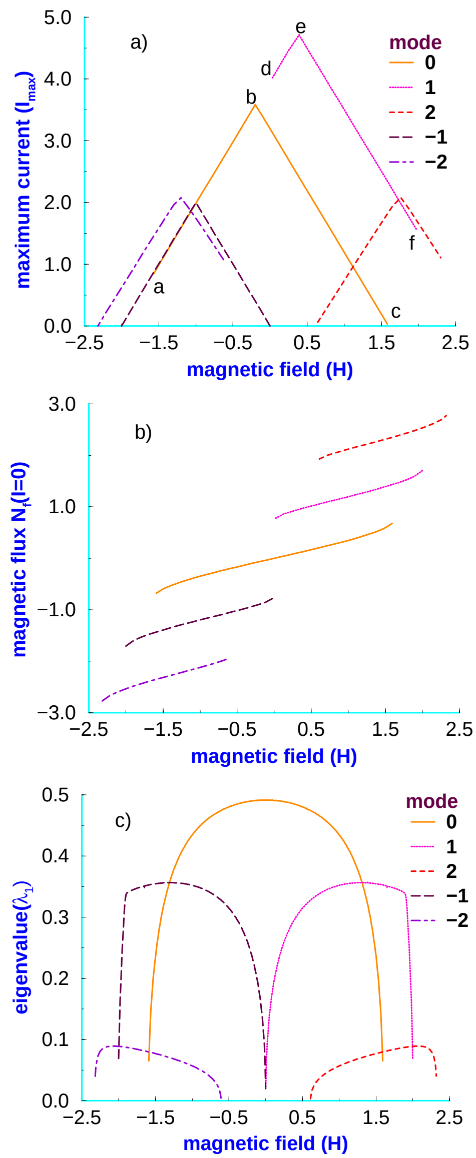

Figure 3.2: (a) Critical current I_{max} and (b) magnetic flux at zero current, versus the magnetic field H, for the different modes. $\ell = 10$ and $D = 1.4$. (c) The evolution of the lowest eigenvalue λ_1 with the external field for the different modes. At the extremes of each mode λ_1 vanishes.

versus the external field. The magnetic flux is only a weak function of the external current.

For the perfect junction there is no overlap in the magnetic flux between the different modes. In fact each mode has flux content between $n\Phi_0$ and $(n+1)\Phi_0$ and therefore is labelled the $(n, n+1)$ mode [22]. Here in the case of the defect the range (at zero current) of flux for each mode can be quite different and the labelling is with a single index $n = 0, 1, 2, ...$ corresponding in several cases to the $(0, 1)$, $(1, 2)$, $(2, 3)$,... modes of the perfect junction. There are in several cases several modes with similar flux. To distinguish them we add a letter following the index n.

The maximum I_{max} is obtained for mode 1 and the increase comes from the trapping of flux by the defect. We have to note that the (d, e) part of this mode is a continuation of the (a, b) part of mode 0. In both cases we have entrance of flux from the no defect part of the junction and the instability in the critical current occurs when $\phi(-\ell/2) = \pi$. Here and in the following we will take this to mean equal to π modulo 2π. For the maximum current (at $H < 0$) the equation is $H - I/2 = -2$. This can be understood from the pendulum phase diagram, where the $\phi_x = -2$ is the extremum slope, and thus the relation $I_{max} = 4 + 2H$ holds. For the (b, c) part of mode 0 the flux enters from the right where the defect is. This reduces the critical current compared to the perfect junction 0 mode [22]. Note that 0-mode has its critical current I_{max} peak slightly to the left of $H = 0$ in the I_{max} vs H diagram, and to the left of $N_f = 0$ in an I_{max} vs N_f diagram (see Fig. 3.11a). Also in the absence of current, reversing the direction of H only changes the sign of the slope $d\phi/dx$, but the phase difference (in absolute value) at the two ends will be the same. Thus the 0 mode at $I = 0$ extends for $-1.6 \le H \le 1.6$. This is not clearly seen due to curve overlapping in the left side. Comparing the I_{max} for the modes 1 and -1 we see that $I_{max}(1) > I_{max}(-1)$. In both cases a fluxon (or antifluxon) is trapped in the defect. The major difference in the I_{max} comes mainly from the phase distribution which in the mode 1 case leads to a large positive net current in the undefected side, while in the -1 mode the net current in the undefected side is very small.

For the mode 1, at $H \approx 0$ and zero current the instability happens due to the competition of the slope of the phase at the defect center and at the right edge, while at the other end at $H = 2$, the field at the defect center becomes equal to the external field applied at the boundaries and there is no such competition. In this case the instability sets in due to the critical value of the phase at the undefected boundary (i.e. $\phi_x(-\ell/2) = 2$). The situation is analogous for the mode -1. For $H \approx 0$ the instability sets in due to the depinning of the antifluxon while for $H = -2$ due to the critical value of the phase at the free defect part of the junction. For the mode 0 we have no fluxon trapping at the defect, even though the instability at the two extremes with $H = \pm 1.6$ at zero current is caused from the tendency to trap a fluxon or antifluxon correspondingly at the defect. At higher values of the magnetic field ($|H| > 1.6$) we have stability for a range of non-vanishing current values as will be discussed below. Thus this value can be considered as the minimum value for the introduction of fluxons in the junction. Let as remark that for the perfect junction, or a junction with a centered defect, the corresponding values for fluxon introduction would be equal to 2. Thus there is a decrease of the critical field as the defect moves away from the center. For the 0 mode a centered defect would have no influence on the solution.

The results for the maximum current are in agreement with the stability analysis. In Fig. 3.2c we present the lowest eigenvalue λ_1 for the different modes in zero external current $I = 0$ as a function of the magnetic field H. The sudden change in slope for the modes $-1, 1$ is because at that point a new eigenvalue becomes lower. The λ_1 is positive denoting stability and becomes zero at the critical value of the magnetic field, where a mode terminates. The symmetry about zero magnetic field is due to the symmetric boundary conditions for $I = 0$. Change of the sign of H changes the sign of the phase distribution, but the $\cos\phi$ in (3.8) remains unchanged. This symmetry is being lost when a finite current is also applied. Also there are solutions (not presented in the figure) for which the stability analysis gives negative eigenvalues i.e instability. These solutions may be stabilized when we insert multiple impurities.

In Fig. 3.3a we specifically draw only the 1 mode, to be discussed in more detail. Here we changed the procedure, in searching for the maximum current. Up to now we followed the standard experimental procedure, i.e. we scan the magnetic field and for each value of H

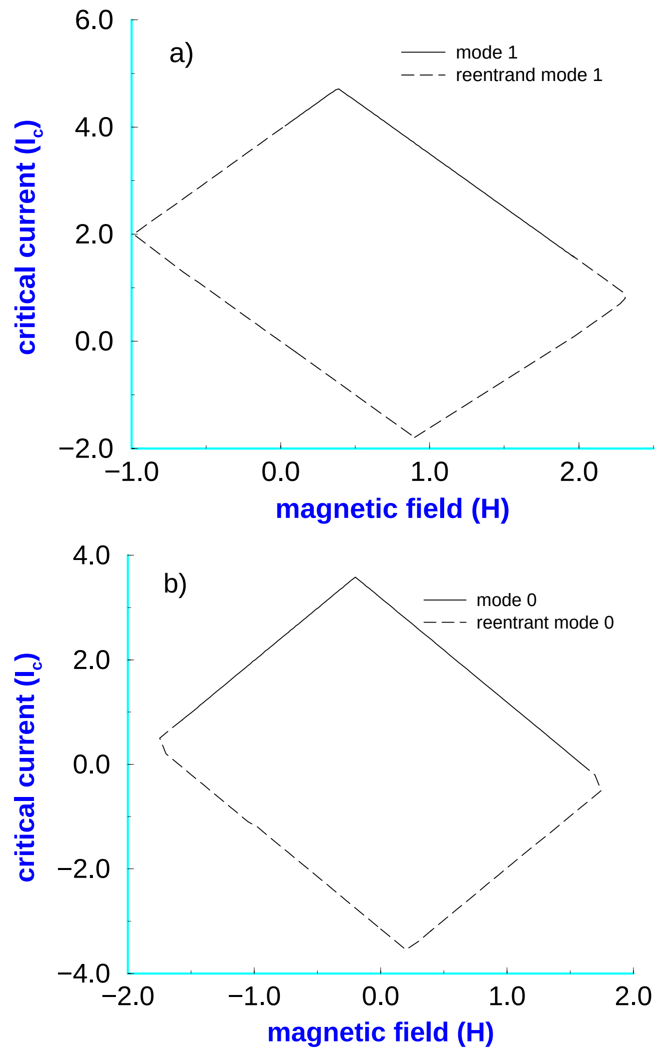

Figure 3.3: (a) Critical values of the bias current as a function of the magnetic field. The solid line is drawn for the mode 1 obtained with the usual procedure starting form zero current and increasing the current to the critical value, while the dashed line represents the values obtained with the reentrant procedure described in the text. (b) The same information as in (a), but for the mode 0.

we increase the current I, starting from $I = 0$, until we reach the maximum current. Here we consider the possibility that for $I > 0$ there is also a lower bound in the value of the current for some values of the magnetic field. This requires a search where we vary both H and I simultaneously. Thus we see that for $H < 0$ there is a lower bound given approximately by the line $H + I/2 \approx H_{cl}$, where $H_{cl} \approx 0$ is the critical value of H at $I = 0$, for which we have depinning of the trapped fluxon. Over this curve the slope ϕ_x at the right end (near defect) is kept constant and equal to H_{cl} and above this line the fluxon remains pinned and it should be stable. This line ends at $H = -1$, since in that case the extremum value $\phi_x = -2$ is reached in the left end. Increasing now in that range of H the bias current we find that also the I_{max} curve extends further to the left. The equation for this line is approximately given by $H - I/2 = -2$, with an extremum at $\phi_x(-\ell/2) = -2$. Thus the instability on this line arises from the left side (far from the defect). It extends up to $H = -1$ for a long junction and joins the other line $H + I/2 = H_{cl}$.

The above calculations were done for a long junction so that the fields at the two ends do not interfere. For shorter length however the two ends feel each other and in that case the two instabilities are not independent. This means that the tail of the defect free side field will compete with the slope of the trapped field. Then the two lines $H+I/2 = H_{cl}$, and $H-I/2 = -2$, end before they meet (at $H \approx -1$) at a cutoff magnetic field. Also for short junctions we expect the straight lines to have some curvature. A similar discussion holds for the right end of the 1 mode. Again there is a lower current (positive) bound given by $H - I/2 = 2$ due to instability at the left end ($\phi_x(-\frac{\ell}{2}) = 2$), and an upper bound given by $H + I/2 = H_{cr}$, where $H_{cr} \approx 2.8$, due to fluxon depinning. On the same diagram, we show the lower bound for negative currents. Thus we see that there is strong asymmetry for positive and negative currents. Remark that for negative currents the mode 1 is very similar to the mode (1,2) with no defect [22]. This is because the right boundary is determined by an instability at the undefected side. The left boundary is again very close because $H_{cl} \approx 0$. So an interesting effect of the defect is that we have this strong asymmetry for positive and negative currents.

We would get a similar picture if we considered the -1 mode. In

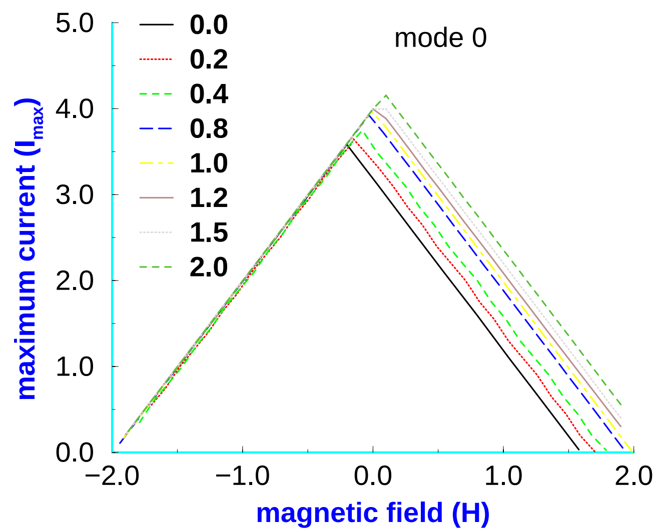

Figure 3.4: Critical current as a function of the magnetic field, for the mode 0, for different values of the defect critical current density j_d.

fact we get the same curves (as for mode 1) if we put $I \to -I$ and $H \to -H$. This is consistent with the -1 mode shown in Fig. 3.2a. The discussion can also be extended to the other modes. In Fig. 3.2b we show the result of a similar scan for the 0 mode, but for the sake of shortness we will not discuss the $-1, -2, 2$ modes. In any case when the number of fluxons increases one must rely on numerical calculations rather than simple arguments.

3.4 Variation with the defect critical current

In the previous section we considered the case of a microresistance defect. With present day masking techniques we can also consider any finite critical current (lower or higher) in the defect. This situation can also arise very often in junctions with high critical current densities, where small variations in the thickness can create strong critical current density variations. Thus for the previous asymmetric defect con-

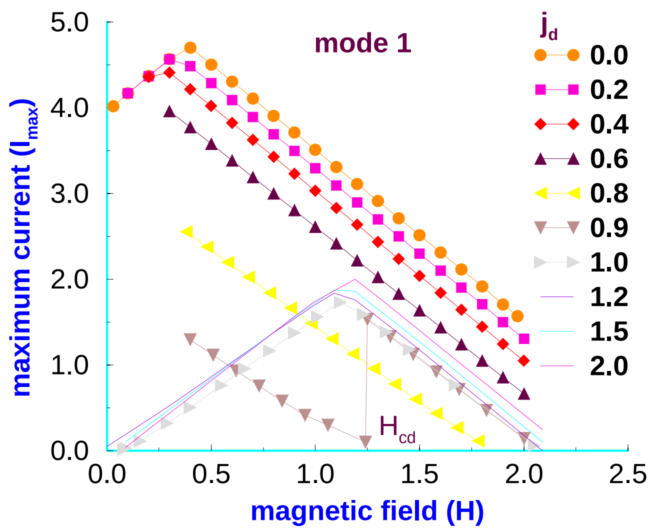

Figure 3.5: Same as in Fig. 3.4, but for the mode 1.

figurations we will study the effect of the defect critical current density in the magnetic interference pattern $I_{max}(H)$. We will concentrate on the 0 and 1 modes.

(i) mode 0:

In Fig. 3.4 we see the $I_{max}(H)$ variation for the mode 0 for decreasing values of the critical current density from $j_d = 2$, to $j_d = 0$. Let us discuss first the case for $j_d \leq 1$. For the perfect junction where $j_d = 1$ we have a symmetric distribution about $H = 0$. As we decrease j_d the flux content of this mode (and the extremum H) is symmetrically reduced (see Fig. 3.2b). It is not apparent from the drawing, due to the superposition of several curves on the left side of the diagram, but as expected the range of the magnetic field is symmetric about $H = 0$ at zero current. The corresponding $I_{max}(H)$ curves, however, are not symmetric. The right hand side of the curves is displaced towards smaller critical fields with decreasing j_d. This means that the critical field at $I = 0$ to introduce a fluxon from the ends is decreased due to the existence of the defect which acts with an attractive force on the fluxon. The curves are linear and can be approximated by the equation $I(H) = 4 - 2(H + \delta H_c)$, where δH_c is the decrease in the critical field

H_{c0} and depends on j_d. A similar decrease happens for negative magnetic fields where the defect tries to pin an antifluxon. Even for higher currents the right side critical field is determined by the tendency of the defect to attract a fluxon. The left hand side, however remains rigid (but is shifted along the line). This is due to the entrance of magnetic flux from that part of the junction where there is no defect. The instability in the critical current occurs when ($\phi(-\ell/2)=\pi$) for every value of j_d. From the pendulum phase diagram which is the classical analog of the Josephson junction, the extremum occurs at $\partial_x\phi(-\frac{\ell}{2})=-2$, or $H-I/2=-2$ which is the equation for this triangular side. At near zero current the critical field is influenced from the attractive action of the defect. At low currents and extreme negative magnetic field the I_{max} curve shows a re-entrance behavior so that it is not stable at low and high currents, but only for a finite intermediate range of current values. This way we reconcile the different origins of the instability mechanisms $\phi(-l/2)=\pi$ at high current and the defect influence discussed for the right hand side of the mode.

For $j_d>1$ we see an increase in the I_{max}, while the critical magnetic field at $I=0$ remains almost constant at about $H_{cr}\approx 1.9$. The instability at that point is due to the trapping of flux in the region between the positive defect and the right edge of the junction. The field for that is expected to be near $H=2$ if the right undefected part is of length of the order of Josephson length. Thus it is the same value for flux penetration from the perfect junction edges. It will vary weakly with j_d.

(ii) mode 1*:*

The mode 1 in the perfect junction has a full fluxon for magnetic field $H=0.07$. The phase distribution is about $\theta=\pi$ where the energy has a minimum. At the end of this mode at $H=2.07$ where two fluxons have entered the junction the phase changes from $\phi(-\ell/2)=-\pi$ to $\phi(\ell/2)=3\pi$. When the defect is inserted this mode is significantly modified due to the flux trapping in the defect.

In Fig. 3.5 we see the magnetic interference pattern for this mode for different values of the defect critical current density. For $0<j_d<0.7$ the I_{max} vs H curves are displaced downwards, and a fluxon is trapped in the defect. We notice that all the curves for $j_d<0.7$ have the same critical magnetic field $H=2$ for $I=0$. This is because at

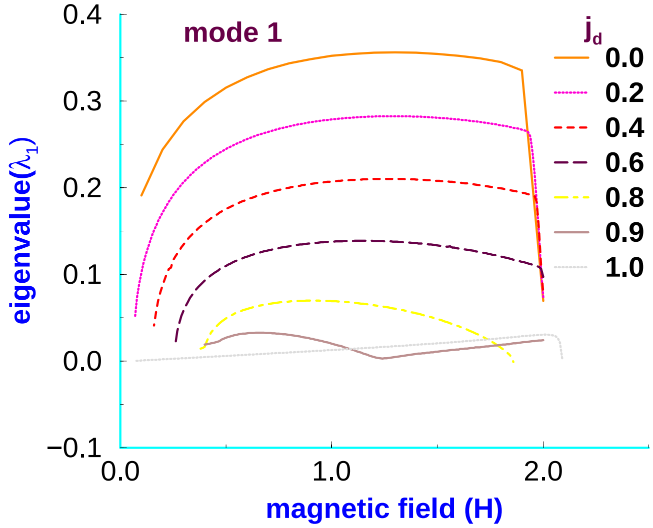

Figure 3.6: The lowest eigenvalue versus the magnetic field for the mode 1 for different values of the defect critical current density j_d.

this end of the mode, at $I = 0$ the instability arises at the side with no defect where the phase reaches the critical value $\phi = \pi$ (modulo 2π). Of course as discussed in the previous section we have a reentrant behavior above $H = 2$. At the other end for small magnetic field the instability is due to depinning of the trapped fluxon. For $0.7 < j_d \leq 1.0$ the defect can trap the flux only for $H < H_{cd}$, where the value of the H_{cd} depends on the defect critical current j_d and in Fig. 3.5 it is shown for $j_d = 0.9$. Notice that for this value of j_d the fluxon is very weakly trapped, and the untrapping process happens slowly over a range of magnetic field values. For $H > H_{cd}$ the fluxon has moved away from the defect, and for this weak defect the junction does not feel it. The critical current goes abruptly close to the curve for the perfect junction. We conclude that the behavior of the junction for values of j_d close to $j_d = 1$ is determined by the ability of the defect to trap one fluxon. This can be seen also from the change in the lowest eigenvalue variation with the external field H, at values of the critical density $j_d > 0.7$, in Fig. 3.6.

For $j_d > 1$ (thin lines in Fig. 3.5) the I_{max} vs H curve for mode 1 has a similar form as for $j_d = 1$, i.e. there is no fluxon trapping. Again,

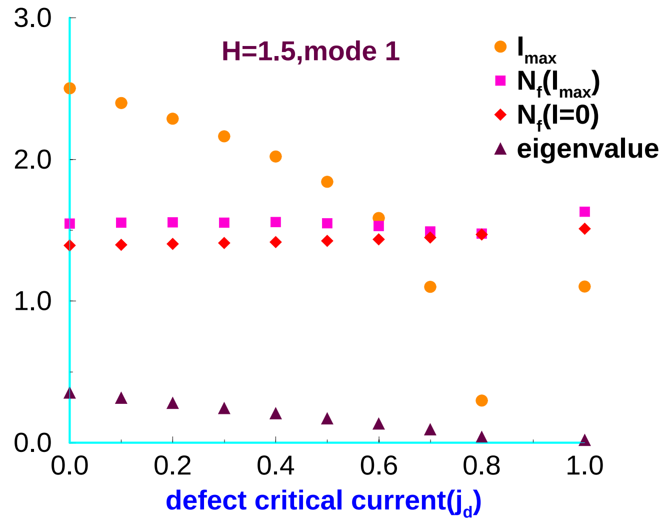

Figure 3.7: Critical current versus the defect critical current density j_d, for magnetic field equal to $H = 1.5$, for the mode 1. In the same graph the magnetic flux at zero and maximum current, and the lowest eigenvalue at $I = 0$ are plotted as a function of the j_d.

as in the 0 mode, the H_{cr} at $I = 0$ stays around 2.0 and is again due to the trapping of flux in the right edge.

In Fig. 3.7 we present the evolution of I_{max} with the defect critical current density j_d for a magnetic field $H = 1.5$. For this value of the magnetic field there are no solutions with trapped fluxons for $j_d > 0.83$. The lowest eigenvalue at $I = 0$ becomes zero at this point. For $j_d > 0.83$ and $H > 1.5$ there are solutions which are not trapped. For these solutions the maximum current coincides with the one of the perfect junction and there is a discontinuity in the curves. Notice the point at $j_d = 1.0$. In the same figure we also show the magnetic flux at $I = 0$ and at I_{max} which is almost constant as a function of j_d as expected, with small difference between the two different current curves.

3.5 Variation with the defect position

In Fig. 3.8a we see the evolution of the critical current at zero magnetic field as we move the defect from the right edge of the junction $D = 0$ to the left edge where $D = 8$. The position is measured from the edge of the junction to the nearest edge of the defect. We examine the several modes separately:

(i) mode 0

For this mode and for $I = 0$, we are able to find solutions for all the defect positions. As we can see in Fig. 3.8b the corresponding magnetic flux at I_{max} is slowly changing and equal to zero when the defect is in the junction center. But when the defect is placed close to the ends the magnetic flux at the maximum current deviates from zero. The critical current for this mode is symmetric for defect positions about the junction center, and has its maximum value when the defect is at the center. This is because at that position it does not influence the solution at the edges which is very close to the undefected case, while near the center the phase is almost zero. But when the defect comes close to the junction ends the defect cuts into the area by which the current flows, and the critical current is reduced.

For even smaller distances $D = 0.2$, and $D = 0$ there is a jump to solutions which correspond to a current, which is much higher than that of the 0 mode for nearby D values. This is because the defect

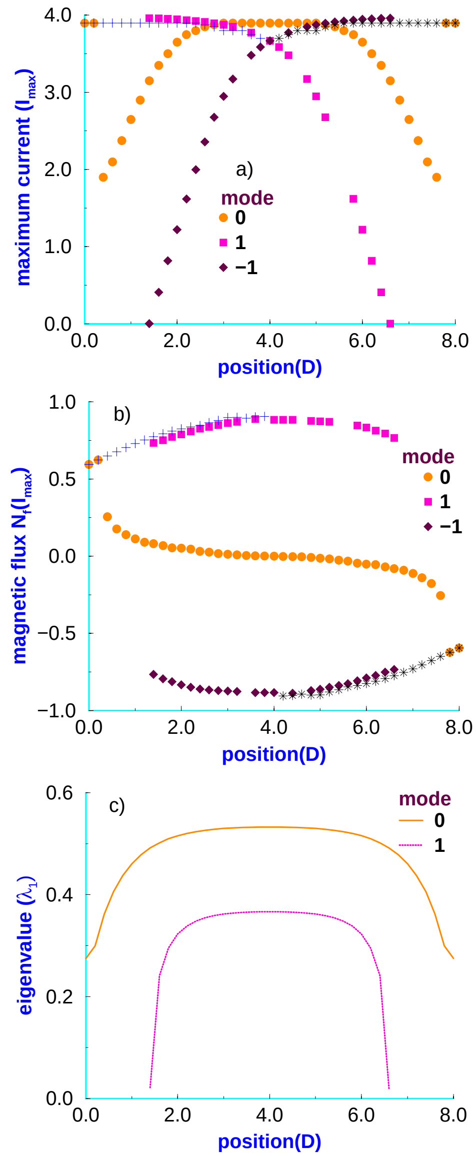

Figure 3.8: The variation of (a) the maximum current I_{max} and (b) the magnetic flux N_f at the maximum current, versus the defect position D, measured from the right edge of the junction, for the modes 0, 1, -1. The crosses and stars lines are continuations of the two points at the two ends of the graph. (c) the corresponding lowest eigenvalue at zero current versus the defect position D, for the modes 0, 1. The -1 mode eigenvalue is the same as for the 1 mode.

cuts negative current regions and for this position we have an increase of the critical current. In fact these solutions (see ++ symbols in Fig. 3.8a) are very close to the solutions of a perfect junction within the undefected area, except that now the defect at the edge can give contribution to the flux but no contribution to the current. Thus the flux is much higher than that of the 0 mode and it approaches that of mode 1. Nevertheless these points should be considered as a separate mode. In fact they are part of a branch (crosses). In these distances there are no other modes for $H = 0$. Similar results were obtained by Chow *et al.* [25] where they attributed this enhancement in the I_{max} for small distances to a self field which was generated by the current, penetrating into the defect and resisted any further penetration of field. To overcome this resistance it was necessary to apply a higher current. But they do not distinguish between modes with different flux content, and their evolution with the defect position.

(ii) modes $1, -1$

For these modes we do not have solutions for all the defect positions at $I = 0$ and $H = 0$, but only in the range $1.4 < D < 6.6$ as seen in Fig. 3.8c where the lowest eigenvalue is plotted as a function of the defect position for the different modes. The curves for the 1 and -1 modes coincide, while the 0 mode shows a change of slope corresponding to the last two points ($D = 0$ and 0.2 discussed above) which belong to another curve. Mode -1 has a trapped antifluxon in the defect. When the defect is to the left ($4.0 < D < 6.5$), then the instability in the current of mode -1 at $H = 0$ is created at the right-end of the junction when the phase reaches the critical value $\phi(l/2) = \pi$. This instability occurs for currents which are less than those necessary to unpin the antifluxon. Notice that increasing the current there is no competition with the slope of the antifluxon trapped in the left end. Thus at this point (for $4.0 < D < 6.5$) the maximum current is very close to the undefected junction mode 0, except that in this case $N_f \approx -1$ is close to an antifluxon. At the other end ($D < 4.0$) the instability for mode -1 is caused by the depinning action of the applied current, which takes now much smaller values (close to zero) because of competition with the pinned fluxon. The phase distribution at the defect free end is that expected for $H = 0$ and I close to zero. The mode 1 with a fluxon trapped has a symmetrically reflected (about the center) form in I_{max} vs

D and the instability for $D > 4.0$ occurs at the left end of the junction, which is the opposite case of mode -1. The eigenvalue becomes zero at the positions $D = 1.4$ and $D = 6.6$. The $\lambda_1(D)$ curve coincides for the modes 1 and -1 due to the fact that the phase distributions for the same D for these modes are symmetric about $x = L/2$, and the $\cos\phi(x)$ that enters the eigenvalue equation is the same.

In the rest we examine the variation of the critical value at which the instability sets in, as we scan the magnetic field in the positive (negative) direction $H_{cr}(H_{cl})$ for zero current, for the different modes, as a function of defect position. This instability can be attributed to the pinning, or the depinning field or to the critical value of $\frac{d\phi}{dx}$ at the defect free edge, depending on the particular mode that we are considering. Explicitly for the mode 0 the instability in the $H_{cl}(H_{cr})$ is due to the pinning of a fluxon (antifluxon), respectively. In this mode the defect has no influence for positions close to the center as seen in Fig. 3.9a and 3.9b. However as we move the defect close to the edges the pinning field $H_{cl}(H_{cr})$ is reduced in absolute value because it is easier to trap a fluxon (antifluxon). For the mode 1 the H_{cr} is constant for all defect positions. This is due to the fact that at $I = 0$ it is the phase distribution at the undefected edge of the junction that determines the instability. Notice that due to the reentrant character the critical magnetic field takes higher values at larger bias currents which vary with defect position. The H_{cl} curve depends on the phase distribution near the defect and therefore is strongly defect position dependent. For the mode -1 the picture is reversed compared with the 1 mode. In this case the H_{cl} is constant while the H_{cr} varies with position. Note that in this mode the depinning of an antifluxon is the reason that causes the instability at H_{cr}.

3.6 Two symmetric pinning centers

As noted defects (with $j_d < 1$) or inhomogeneities in the junction can play the role of pinning centers for a fluxon. In this section we discuss more precisely the effect of multiple pinning centers on the magnetic interference patterns $I_{max}(H)$ and the flux distribution. The pinning effect of the Josephson junction has also been analyzed in [107, 106],

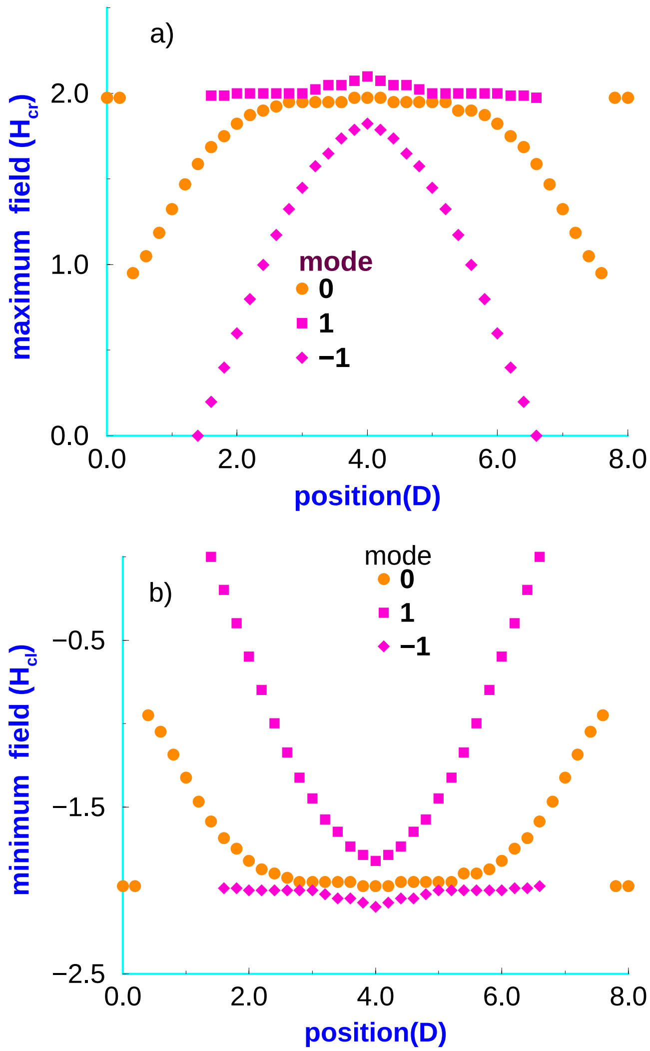

Figure 3.9: (a) The critical value of instability as we scan the magnetic field to the right H_{cr} as a function of the defect position D, for the modes 0, 1, -1. (b) The same as (a) but to the left for the H_{cl}.

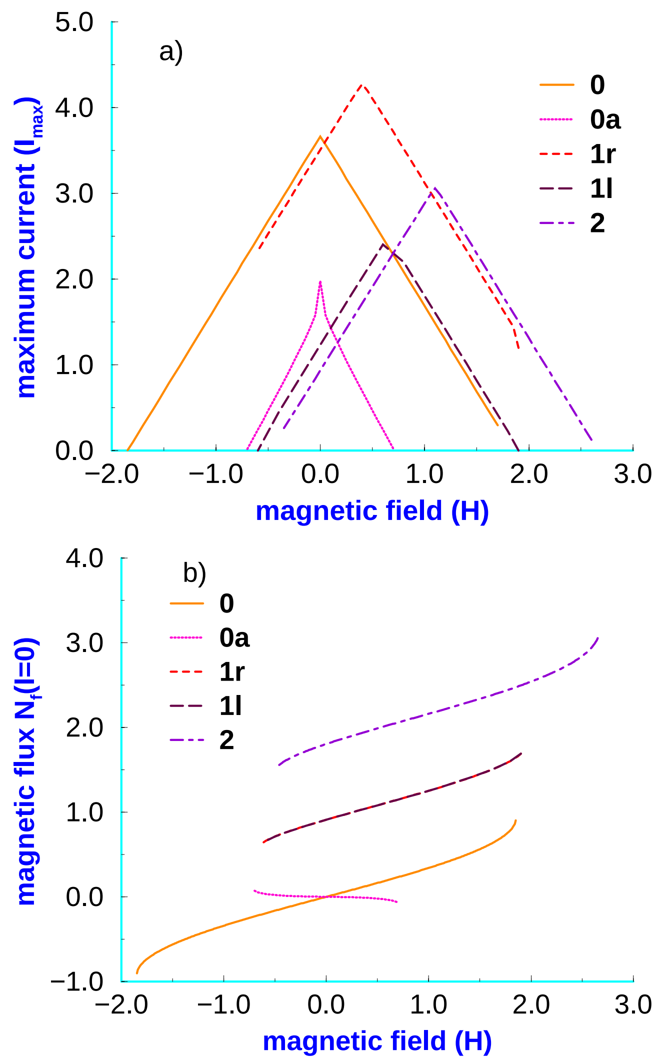

Figure 3.10: (a) Critical current I_{max} and (b) magnetic flux N_f, versus the magnetic field H, for the different modes, for a junction of length $\ell = 10$, which contains two symmetric pinning centers of length $d = 2$.

by using a simple mechanical analog. The analogies of the mixed state of type II superconductors and vortex state of the Josephson junction has been discussed in these references. In Fig 3.10a we present, as an example, the critical current I_{max} versus the magnetic field for a junction which contains two defects of length $d = 2$ placed symmetrically at a distance $D = 2$ from the junction's edges. We examine the following modes grouped according to flux content:

(i) modes 0, 0a

These modes have magnetic flux antisymmetrical around zero field, as seen form Fig. 3.10b where the magnetic flux is plotted versus the magnetic field. At $I = 0$ and magnetic field $H = -0.7$, the $0a$ mode contains one fluxon trapped in the left defect, while an antifluxon exists at the other part of the junction. As H increases towards 0.7 the picture changes slowly, so that the antifluxon is pinned in the right defect. The stability analysis shows that this mode is unstable. We remark that there are also other unstable modes near zero flux, which we will not present here. For example there is another unstable mode with the same flux as $0a$ but a much higher critical current (the same as the 0 mode). Mode 0 has phase distributions which are similar to the corresponding mode of the homogeneous junction since it has no trapped flux in each defect.

(ii) modes 1l, 1r

These modes have magnetic flux close to unity, and are both stable. For the mode $1r$ one fluxon has been trapped to the right defect, and in the mode $1l$, the vortex is trapped in the left defect. Due to the symmetry this mode has the same magnetization as the mode $1r$, but the critical current is reduced. The phase distribution for the modes $1r$, and $1l$, at zero current are related by $\phi_{1l}(x) = 2\pi - \phi_{1r}(-x)$. The maximum field $H = 1.9$ (at $I = 0$) for both modes is determined by an instability at the fluxon free side. At the other extreme there is a competition at the fluxon side between the applied field and the field created by the pinned fluxon. Thus the critical field at $H = -0.62$ can be considered as a coercive field and below this value the fluxon gets unpinned. The two modes have characteristically different currents and this depends on the current through the fluxon free defect, since the pinned fluxon itself gives no major contribution. Thus the maximum current is much larger for the $1r$ mode. The opposite would be true if we look for negative currents. There are also the symmetrically situated modes that correspond to an antifluxon in the left or right defect, which are not shown in Fig. 3.10a. The respective flux is antisymmetric with H around $H = 0$.

In Fig. 3.10a we also show the mode 2 with flux around 2 fluxons. Several unstable modes are not shown, for the sake of clarity. Their analysis however, can show the connection between different modes, while a defect in the correct place with proper characteristics can stabilize these solutions. We conclude that depending on the positions where the vortex is trapped we may have modes with the same magnetic flux content, but different critical currents. Also due to soliton localization on the defects, we may have stable states with magnetic flux close to unity, for zero magnetic field. These states together with the one existing in the homogeneous junction form a collection of stable states in a large H interval. We must comment here that states with unit flux, for zero magnetic field ($H = 0$) exist in the homogeneous junction, as a continuation of the stable (1) mode to negative magnetic fields, but as we found in a previous work [22], are unstable. So we may argue here that the presence of defects stabilizes these states.

In comparing the results for one (Fig. 3.2a) and two defects (Fig. 3.10a) we see some similarities and differences. In the case of two defects new modes appear but also the region of stability of the equivalent modes is different. This is more clearly seen in Fig. 3.11 where we plot the I_{max} vs N_f for both cases. This presentation is useful since the N_f is a nonlinear function of H. This plot (Fig. 3.11a) is a combination of Figs. 3.2a and 3.2b. We should point out that the maximum peak in the current in both case comes due to the trapping of a fluxon in the defect at the right side. The maximum of 0-mode is very close in both cases and this happens because this mode does not involve fluxon trapping. The $1r$ mode for the two defect case is very close to the 1 mode of the single defect, since in both cases there is a fluxon trapped in the same side. In the two defect case we see an enlargement of the region of stability so that the modes overlap. The thin continuation lines in modes 0 and 1 for the single defect are in the reentrant region of flux as discussed in section 3.2.

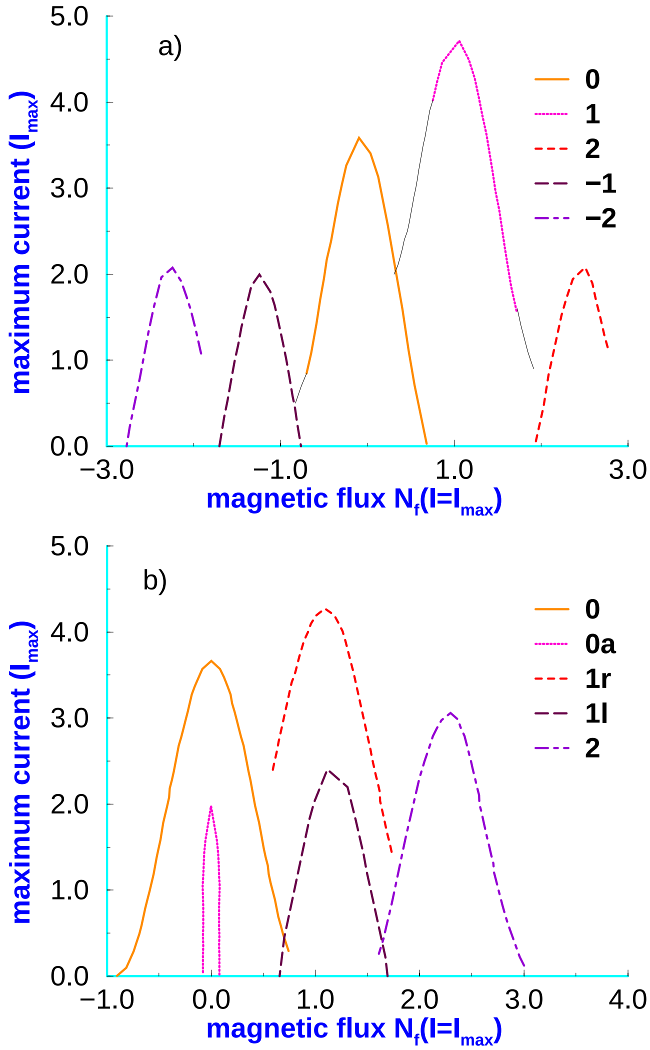

Figure 3.11: Critical current I_c, versus the magnetic flux N_f, at the maximum current for the different modes, for a junction of length $\ell = 10$, (a) for the asymmetric defect case, and (b) for the two symmetric pinning centers of length $d = 2$.

3.7 Symmetric distribution of pinning centers

In this section we study as an example the case where a junction of length $\ell = 14.2$ contains three defects of length $d = 2$, and the distance between them is 2. The length was augmented, so that we keep the same width of the defects when we increase the number of the defects, since we saw that the width of the order $d = 2$, gives the possibility of fluxon trapping and increased maximum current when the defect is situated asymmetrically. We will study the phase distribution at $I = 0$ and try to extract information about the critical field values and magnetization. We find the following modes grouped according to flux content:

i) modes 0, $0l$, $0r$, $0c$

In Fig. 3.12a we present the critical current versus the magnetic field for the modes with magnetic flux around zero (see Fig. 3.12d). This is indicated by the 0 symbol. There are four modes belonging in this category, which are stable. The solutions for the mode 0 are similar to the homogeneous junction mode 0, with no flux trapping in the defects. The only difference is that the instability in the critical field occurs when the phase at one edge, reaches a value, which is smaller (due to pinning) than the corresponding value for the undefected junction, which is $\phi(-\ell/2) < \pi$. The same was true for the two defect case. Mode $0c$ has the maximum critical current $I_{max} = 5.08$ for $H = 0$. One antifluxon is trapped to the leftmost defect, one fluxon to the rightmost, and the phase in the center defect is constant. The trapping at the edge defects leads to a positive current distribution between them, for this particular length, and enlarges the maximum current. The same type of mode was not found for the two defect case (with a shorter junction length), and we conclude that the extra defect along with the increased junction length stabilizes this solution. For the mode $0l$ one fluxon is trapped in the left defect where the phase changes about the value $\phi = \pi$. The antifluxon is distributed at the other two defects, where the phase is about the values $3\pi/2$ (or $\pi/2$), and we have a cancellation of the positive and negative current density in this region. Similar for the mode $0r$ the fluxon is trapped to the right defect, and the current

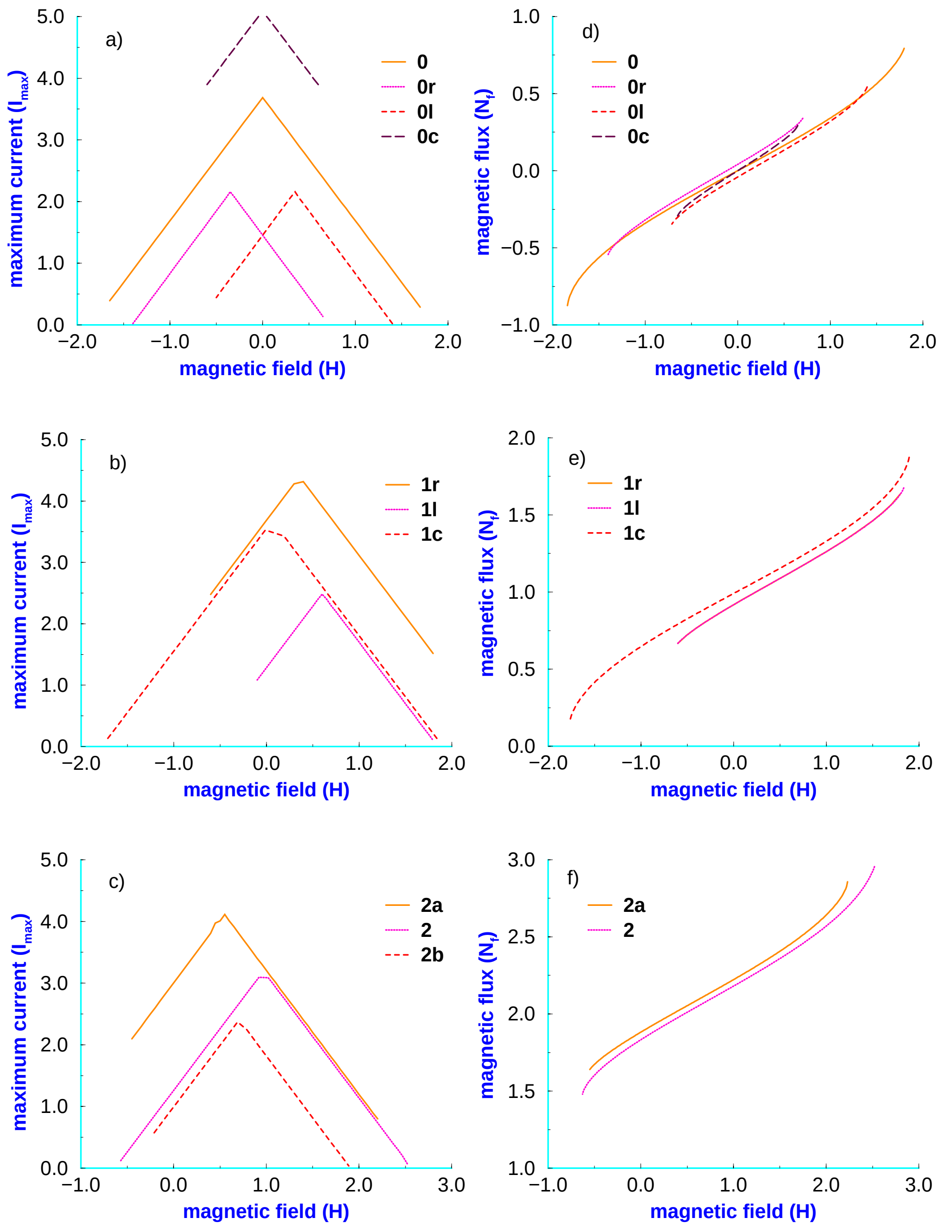

Figure 3.12: Critical current I_{max} versus the magnetic field H, for the different modes (a) 0, $0l$, $0r$, $0c$, (b) $1r$, $1l$, $1c$, and (c) 2, $2a$, $2b$. for a junction of length $\ell = 14.2$, which contains three symmetric pinning centers of length $d = 2$. The corresponding magnetic flux is presented in (d), (e), (f).

is distributed with opposite sign to the other two defects. These modes are similar to the $0a$ mode for the two defect case.

ii) modes $1l$, $1c$, $1r$

In Fig. 3.12b we see the maximum current versus the magnetic field for the modes with magnetic flux around $N_f = 1$ (see Fig. 3.12e). There are three modes with flux close to $N_f = 1$ each of which corresponds to the trapping of one fluxon in one defect. In the mode $1c$ the fluxon is trapped in the center defect. In the mode $1l$ ($1r$) it has been trapped in left (right) defect. Due to the symmetry the lowest eigenvalue, and the magnetic flux coincides for these two modes, but as we showed in the previous section, their critical currents are different, depending on the tunneling current distribution in the region with no trapping. The $1r$ mode corresponds to a higher critical current.

iii) modes 2, $2a$, $2b$

In Fig. 3.12c we see the maximum current versus the magnetic field for the modes with magnetic flux around $N_f = 2$ (see Fig. 3.12f). Only the mode 2 corresponds to stable solutions. There we have two fluxons trapped in the side defects. In mode $2a$ one fluxon is trapped in the right defect, while in mode $2b$ this trapping occurs in the center defect. We conclude that distributed pinning centers are more effective in trapping the vortex, and lead to an increased critical current. Some conclusions will continue to be valid for larger number of defects where we keep the defect width and separation fixed. In that case we also expect the results to change significantly when there is either a periodic array of defects, where we expect higher fluxon modes to give the highest current peak [47].

3.8 Defect with a smooth variation of current density

Up to now we considered defects with abrupt changes in the local critical current density and the question arises whether the abruptness of J_c variation is crucial in the significant change in I_{max} for the $n = 1$ mode. We will see that similar effects exist for smoother variation, where again the fluxon pinning is an important feature. For this reason

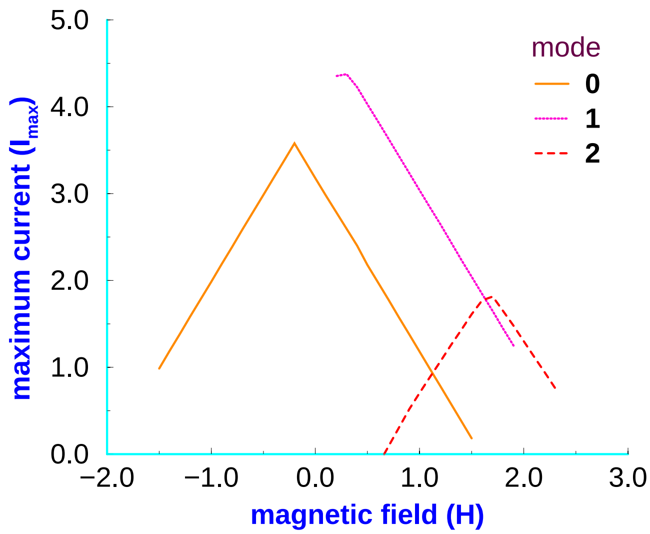

Figure 3.13: Inline critical current I_{max} versus the magnetic field H, for the modes 0, 1 and 2, for the junction with an asymmetric defect but smooth variation of the critical current density.$x_0 = 7.6$ and $\mu = 2$.

we chose a single defect at the junction center with a smoothly varying critical current density given by

$$\tilde{J}_c(x) = \tanh^2\left[\frac{2}{\mu}(x - x_0)\right], \qquad (3.9)$$

where the defect is centered at x_0, and the width is determined by μ.

In Fig. 3.13 we show the results for the case $x_0 = 7.6$ and $\mu = 2$, which can be compared with the results of the asymmetric defect in Fig. 3.2a. For the modes shown the curves are very similar and thus we see that the main results survive since the defect strengths are similar. Of course there is a quantitative difference. But most of the stability criteria described earlier are still valid.

In Fig. 3.14 we consider the effect of the form of current input and compare the case of inline with overlap for a smooth defect situated at the center of the junction i.e. $x_0 = 0$ with $\mu = 0.5$. In Fig. 3.14a we present the I_{max} for inline boundary conditions, and we show only the $-1, 0, 1$ modes. The 0 mode is not influenced at all from the defect

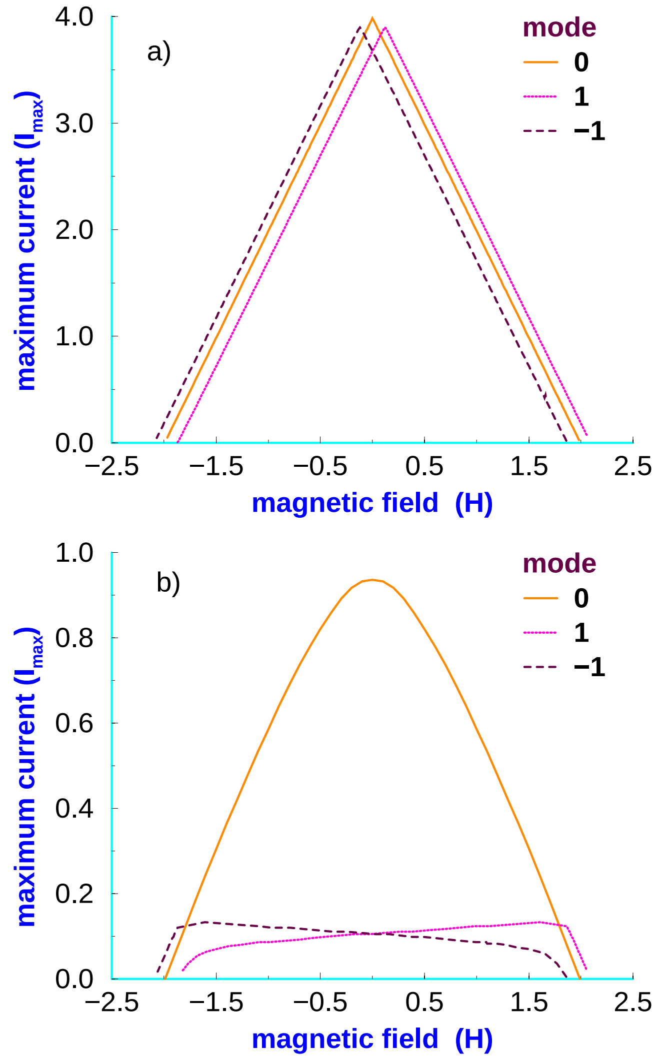

Figure 3.14: Critical current I_{max} versus the magnetic field H, for the different modes, for (a) inline current and (b) overlap current, for the junction with a centered defect, and smooth variation of the critical current density.

since all the phase variation is at the boundaries. There is a strong similarity with I_{max} for the 1, and -1 modes. The reason is that in these cases there is a trapped fluxon or antifluxon at the center and at zero current and magnetic field the phase variation dies out at the boundaries. Thus when increasing the current at $H = 0$ towards I_{max} we have the same situation at the boundaries as for the 0 mode and the instability happens at close I_{max} values. Of course due to the pinning, the fluxon content is very different from the 0 mode. The -1 and 1 modes have an enhanced I_{max} and the small difference in I_{max} from the 0 mode is attributed to the small influence of the trapped fluxon to the boundaries. Let us remark that a similar situation was seen in Fig. 3.8a for the square well defect, when the defect position is at the center for $H = 0$. By comparing with Fig. 3.9 the H_{cl} and H_{cr} values we see close agreement with the case of $j_d = 0$ in the defect. These results could change for a smaller length junction or if we move the defect towards the edges (as seen in Fig. 3.8a).

For the same defect we also investigated the effect of the overlap current input, where the current is distributed along the whole junction. In Fig. 3.14(b) we present the maximum current per unit junction length versus the magnetic field, and it should be compared to the inline case in Fig. 3.14(a). We see a significant change for the -1 and 1 modes. Of course at $I = 0$ both current inputs give the same solutions, but I_{max} is much smaller for the overlap boundary conditions. This is from the fact that due to the applied current the fluxon is pushed against the pinning barrier until it is overcome at the critical current. In the absence of applied current the phase at the defect center is $\phi(0) = \pi$, while the application of the current pushes the fluxon to the edge of the defect which is taken to be near the point where the curvature of the defect critical current distribution changes sign. So we can consider in this case this maximum current as a measure of the pinning force.

In Fig. 3.15a we plot the magnetic flux N_f at zero current versus the magnetic field H for the inline case. The lowest eigenvalues for the different modes versus the magnetic field are seen in Fig. 3.15b. For a homogeneous junction the 0 mode is the only stable state available at $H = 0$. However in the problem we consider here, the mode $1(-1)$ exists and it is stable for $H = 0$ and corresponds to the localization of the soliton (antisoliton) in the inhomogeneity. For these modes we

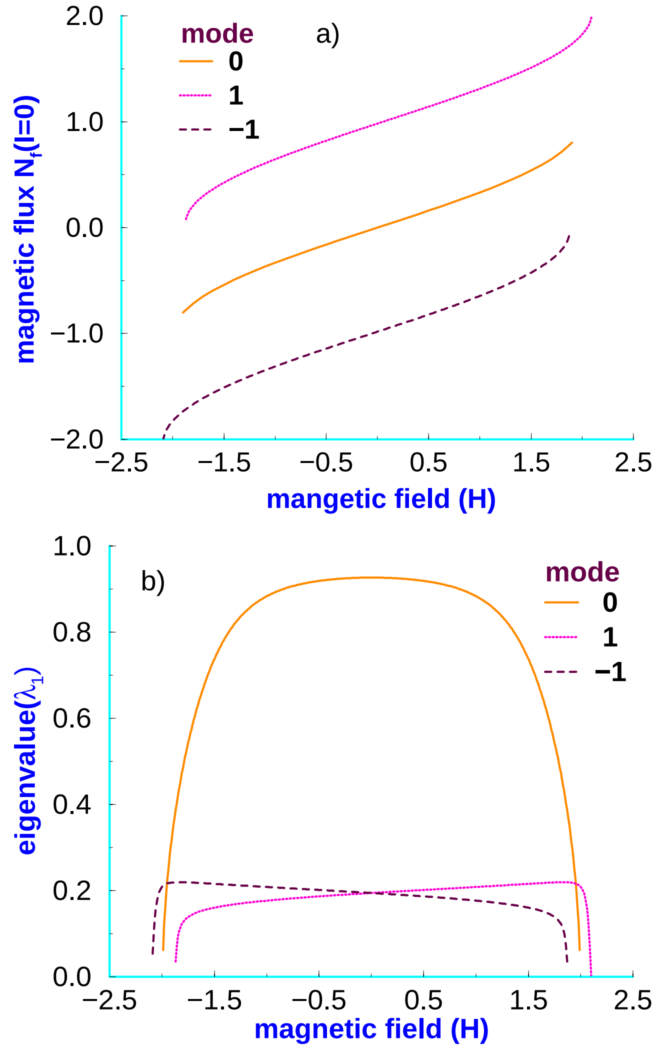

Figure 3.15: (a) Magnetic flux at zero current as a function of the external field, for the same type of inhomogeneity as in Fig. 3.14. (b) The corresponding evolution of the lowest eigenvalue λ_1 for the different modes. At the end of each mode the λ_1 vanishes.

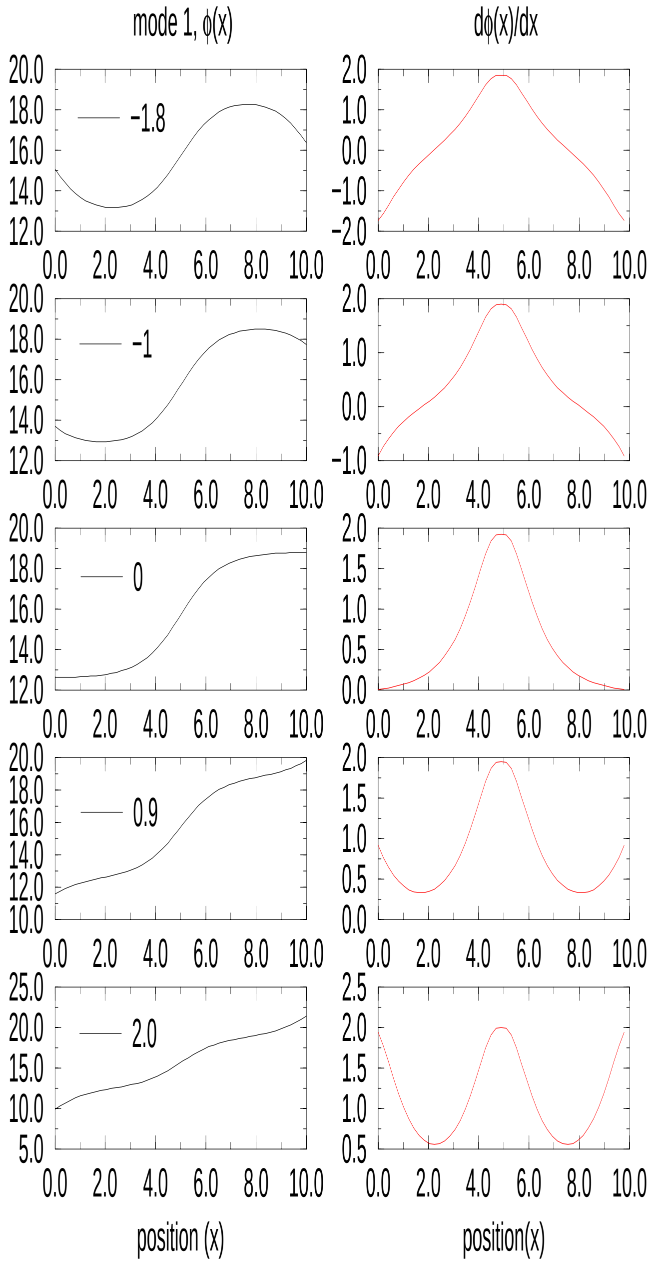

Figure 3.16: The evolution of $\phi(x)$ and $\frac{d\phi(x)}{dx}$, for the mode 1, as we change the magnetic field at $I = 0$, for the same type inhomogeneity as in Fig. 3.14. Numbers are H values.

have pinned flux at $H = 0$, with $\phi(0) = \pi$, and $\frac{d\phi}{dx} = 2$. In Fig. 3.16 we show the evolution of ϕ and $\frac{d\phi}{dx}$, for the mode 1, as we change the magnetic field at $I = 0$. Near $H = -1.9$ the fluxon content is near zero and for $H < -1.9$ an instability sets in due to the depinning of the fluxon. This is because the slope at the pinned fluxon competes with the opposite slope tried to be imposed by the external negative magnetic field at the boundaries. At the other end the flux is equal to 2, and the instability sets in when ϕ at the boundaries approaches π (or odd multiplies). The range of H values for the 1 mode, when the defect is at the center is significantly broadened and gives a corresponding range for the flux of two fluxons. Usually each mode has about one extra fluxon and in particular for the perfect junction it contains only one extra fluxon. This is because the defect is at the center and far enough from the edges where the magnetic field is applied and therefore even for negative fields there is no significant competition, with the field at the defect center. This is especially true when the distance of the defect from the edges is grater than $2\lambda_J$. When however the defect is near the edge the instability sets in before we cross to negative magnetic fields. The maximum current I_{max} for the mode 0 is greater than in the modes $1,-1$, but is reduced compared with the I_{max} for the mode 0 in the homogeneous junction, in zero field. In [33] they approximated this reduction in an analytical calculation using a delta function for the defect potential, and they found $\Delta I_{max} = -\mu/2L \approx 0.02$. In [33] they arrived at the analytical result, by minimizing the fluxon free energy, for the maximum overlap current versus the magnetic field H, for these modes, which is a good approximation of the numerical solution we consider here in the limit $L \gg 1$.

3.9 Conclusions

In several applications it is desirable to work in an extremum of the current for a region of the magnetic field. This can be achieved by the appropriate distribution of defects so that the negative lobes of the current distribution in the junction due to the fluxons are trapped in the defect with no contribution to the current. Of course if the defect is isolated (far from other defects or the edges) we expect zero contribution to the current. Due to the effect of the applied current and magnetic field at the boundaries in certain cases we can obtain positive current lobes outside the defect. In several cases in section 3.3 this was the reason for the increased current. Because the control of magnetic field is very easy compared to other system parameters (like temperature, disorder, etc.) the measurement of the effect of magnetic field on junction behavior, provides a convenient probe for the junction. The calculation of the I_{max} can characterize the quality of the junction or verify the assumed distribution of defects when they are artificially produced. The spatial variation of the critical current density on low T_c-layered junctions, and high T_c grain boundary junctions can be directly imaged with a spatial resolution of $1\mu m$ using low temperature scanning electron microscopy ($LTSEM$) [45, 36]. Information on smaller scale inhomogeneities has to rely on the magnetic field dependence of the maximum tunneling current I_{max}.

The purpose of this chapter is the consideration of large defects in order to study the interaction between fluxons and defects and give estimates of the coercive field for pinning or depinning of a fluxon from a defect. The region of consideration puts us far from the region of perturbation calculations and is amenable to direct experimental verification since it is easy to design a junction with the above characteristics. The defects influence strongly the low fluxon modes. At high magnetic fields larger than the depinning field of a single fluxon we expect only minor effect and fluxon trapping. Of course for a large number of defects interesting behavior can be obtained.[71, 62] The interaction between fluxons in the few defect case also assists to overcome coercive fields and untrap fluxons. The results of two trapped fluxons in the two defect case show that the fluxons are strongly coupled and one cannot consider an exponential interaction type potential between the fluxons. Also the critical current in a long junction, cannot be calculated as the Fourier transform of the spatial distribution of the critical current density $J_c(x)$, at least for weak magnetic fields. For strong magnetic fields, where we have the field penetrating uniformly the junction, as is the case for short junctions, we recover the diffraction like pattern.

In summary we saw that the bounds of the different modes determined by the stability analysis depend on two factors: (i) the instability at the boundaries away from the defect when ϕ_x reaches its extremal values equal to ± 2, and (ii) the instability due to the pinning or depinning of a fluxon by the defect. If the junction is near one end then we saw that both criteria play a role in determining the instability, independently in different areas. In general, however, there will be coupling between defects and the edges (surface defects) especially in the case of multiple defects. Defects also introduce hysteresis phenomena which are weaker in the case of smooth defects. We also saw that due to fluxon trapping in general we see a reentrant behavior, i.e. there are regions of magnetic field for which there is both an upper and a lower bound on the maximum current. We also find that due to the pinning of magnetic flux from the defect there exist additional stable states in a large interval of the magnetic field. The abrupt change in the critical current density is not crucial for the trapping. Similar results are expected from smooth defects, with quantitative differences. The above results can be checked experimentally since it is easy to design a junction with a particular defect structure, using masking techniques. In fact a few parameters or characteristics could give at least partial information on defect properties. In particular the measurement of H_{cr} or H_{cl} can give some information of the defects near the edges. In addition the measurement of the I_{max} vs H diagram will give us information on the defect critical current density. Also one can imagine the situation where we scan locally with an electron beam affecting thus the local critical current and observe the variation of the I_{max} as we increase the heating. Once a fluxon is trapped we can decrease the heating (or increase j_d) and observe the variation of I_{max}. Thus one can have pieces of information to put together in guessing the defect structure that might fit the whole I_{max} pattern. The extension to many defects requires considerable numerical work. It is hoped, however, that some of the stability criteria will still be useful.

Chapter 4

Magnetic-interference patterns in Josephson junctions with $d + is$ symmetry

4.1 Introduction

In this chapter the numerical techniques of chapter 2 and also the skills acquired in the problem of a macroscopic defect will be applied to a more interesting problem, which deals with the pairing symmetry of unconventional superconductors [80, 42, 103, 97, 54].

This question is crucial since it will allow the identification of the underlying mechanism of superconductivity in cuprates. The Josephson effect provides a unique tool in theory and experiment since it is sensitive to the phase as well as in the magnitude of the order parameter.

The most possible scenario is that the bulk pairing state is an admixture of a dominant d-wave with some small s-wave component. This fact is a direct consequence of the orthorhombic distortion of the systems which makes both the d-wave and s-wave indistinguishable (they transform according to the identity representation of the group). There is a basic difference in the physics if one takes into account the phase difference between the two parts of the order parameter. The mixing due to orthorhombicity predicts a $d+s$ or equivalently $d-s$ order parameter. In an orthorhombic lattice the crystal axis a and b are not equal. The order parameter has to follow the symmetry of the lattice. The $d+s$ or $d-s$ order parameter has one lobe slightly larger than the other and hence it is related to the crystal lattice structure. Therefore the order parameter in orthorhombic YBCO lattice has to be $d+s$ or $d-s$. This has been analyzed within the Ginzburg-Landau framework, valid close to T_c [17]. Experimental observation of this possibility has been clearly realized in photoemission experiments [64] and the c-axis tunneling [57].

In addition to the above work, calculations based in BCS weak-coupling theory [70, 78] predict that a mixed symmetry is realized in a certain range of interaction. This state has the time-reversal symmetry $\mathcal{T}$ broken. This symmetry $(d+is)$ is realized in bulk calculations only as a consequence of the absence of any orthorhombic distortion since the orthorhombic distortion favors the $d+s$ or $d-s$ order parameters. The $d+is$-wave state favors a phase difference of $\pi/2$ between the two components as opposed to π in the $d+s$ state. The Fermi surface is either circular or tetragonal in the particular examples. In the $d+is$ state the dominant order parameter d is superimposed with a complex s-wave order parameter in a sense that the shape of the d-wave lobes is not affected. Hence the $d+is$-wave function should be related to a crystal lattice with tetragonal symmetry.

The situation becomes more complicated if we consider surface effects. The observation of fractional vortices on the triangular grain boundary in $YBa_2Cu_3O_7$ by Kirtley *et al.* [51], may indicate a possible violation of the time-reversal symmetry near grain boundary (because the boundary breaks the bulk orthorhombic symmetry). Their experimental arrangement consists of two segments of c-axes textured YBCO films where one is a triangular inclusion within the other. Therefore it is interesting to study more this symmetry in the case of interfaces.

In the present chapter we study the static properties of a one dimensional junction which contains a twin boundary where the phase difference between the two superconductors acquires an extra relative shift in each twin. The maximum current I_c that a junction can carry versus the external magnetic field H in the direction parallel to the plane of the junction is calculated by solving numerically the sine-Gordon equation. The stability of fractional vortices f_v or antivortices f_{av} which are spontaneously formed as a consequence of the symmetry, is examined in the absence of current and magnetic field for different lengths and relative phases.

In the $\mathcal{T}$-violated state the magnetic interference pattern as has been obtained by Zhu *et al.* [108] in the short-junction limit is asymmetric. They conclude that for a long junction the magnetically modulated critical current is basically identical to the conventional 0-0 junction due to the formation of the spontaneous vortex near the center of the junction. Our exact numerical calculations show that there is a "dip" near the center of the diffraction patterns even for junctions as long as $10\lambda_J$.

The rest of the chapter is organized as follows. In Sec. 4.2 we discuss the Josephson effect between two superconductors with mixed s and d-wave symmetry. In Sec. 4.3 the role of the twin boundary is discussed. In Sec. 4.4 we present the results for the magnetic flux and the interference pattern. Finally, a summary and discussion are presented in the last section.

4.2 Josephson effect with mixed wave symmetry

The GL free-energy density in terms of two complex components of the order parameter, $n_1(\mathbf{r})$ and $n_2(\mathbf{r})$ is given by

$$f(\mathbf{r}) = a_2|n_2|^2+a_1|n_1|^2+\frac{\beta_2}{2}|n_2|^4+\frac{\beta_1}{2}|n_1|^4+\beta_3|n_1|^2|n_2|^2+\beta_4({n_2^*}^2n_1^2+{n_1^*}^2n_2^2)$$

$$+\gamma_2|\mathbf{\Pi}n_2^*|^2+\gamma_1|\mathbf{\Pi}n_1^*|^2+\gamma_\nu[(\Pi_x^*n_2\Pi_xn_1^*-\Pi_z^*n_2\Pi_zn_1^*)+c.c.]+\frac{(\nabla\times\mathbf{A})^2}{8\pi} \tag{4.1}$$

where $a_{1,2}$, β_i, $i = 1,2,3,4$ and $\gamma_{1,2,\nu}$ are real coefficients, and the operator

$$\mathbf{\Pi} = -i\hbar\nabla - \frac{2e}{c}\mathbf{A}. \tag{4.2}$$

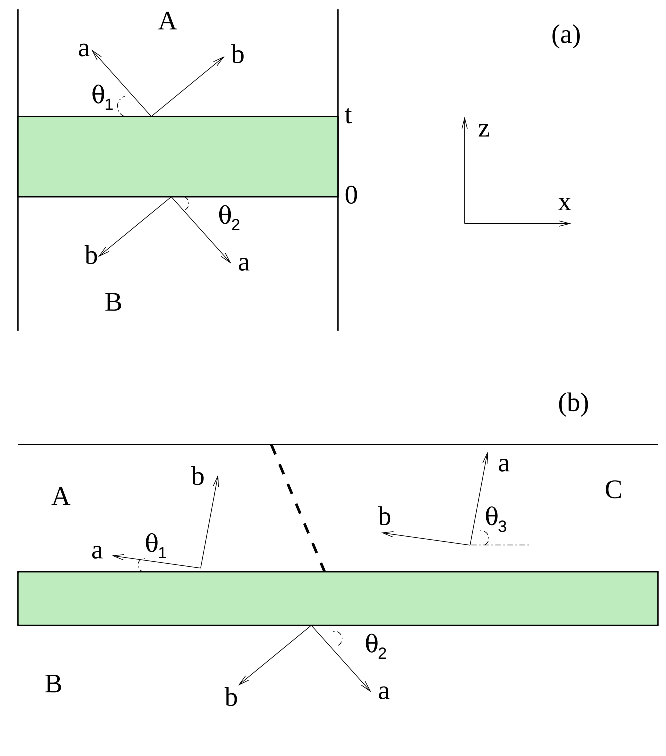

Figure 4.1: (a) A single Josephson junction between superconductors A and B with a two component order parameter. The angle between the crystalline a axis of $A(B)$ and the junction interface is $\theta_1(\theta_2)$. (b) The geometry of the junction between the twinned crystal (regions A and C) and the untwinned crystal B. The dashed line marks the twin boundary.

In the case where the interaction in the dominant pairing channel 1 and the subdominant 2 is attractive the phenomenological parameters a_2 and a_1 are taken to be proportional to $1 - T/T_2$ and $1 - T/T_1$, where T_2, and T_1 are the transition temperature for the 2 and 1 order parameter respectively. Also the parameters $\gamma_i, i = 1, 2, \nu$ are related to the effective masses in the way, $\gamma_i = 1/2m_i^*$.

By varying the free energy $\int f(\mathbf{r})d\mathbf{r}$ with respect to n_1^* and n_2^*, we obtain the field equations for the order parameter n_1 and n_2,

$$a_2 n_2 + \beta_2 |n_2|^2 n_2 + \beta_3 |n_1|^2 n_2 + 2\beta_4 n_1^2 n_2^* + \gamma_2 \mathbf{\Pi}^2 n_2 + \gamma_\nu (\Pi_x^2 - \Pi_z^2) n_1 = 0 \tag{4.3}$$

$$a_1 n_1 + \beta_1 |n_1|^2 n_1 + \beta_3 |n_2|^2 n_1 + 2\beta_4 n_2^2 n_1^* + \gamma_1 \mathbf{\Pi}^2 n_1 + \gamma_\nu (\Pi_x^2 - \Pi_z^2) n_2 = 0 \tag{4.4}$$

The current density is given by

$$\mathbf{J} = (\frac{e}{m_2^*} n_2^* \mathbf{\Pi} n_2 + \frac{e}{m_1^*} n_1^* \mathbf{\Pi} n_1 + \frac{e}{m_\nu^*} [(n_2^* \Pi_x n_1 + n_1^* \Pi_x n_2)\mathbf{e_x}$$

$$-(n_2^* \Pi_z n_1 + n_1^* \Pi_z n_2)\mathbf{e_y}]) + c.c.. \tag{4.5}$$

We consider two superconductors (A and B), with a two component order parameter $(n_1^{A(B)}, n_2^{A(B)})$, which are separated by an intermediate layer of thickness t in the z direction, as seen in Fig. 4.1(a). If the angles between the crystalline a axis of each superconductor A and B with the junction interface are defined as θ_1 and θ_2, respectively, the bulk order parameters n_1 for the d-wave component and n_2 for the s-wave component, near the interface can be written as

$$n_1 = \begin{cases} \tilde{n}_1^A e^{i\phi_1^A} = n_{10}\cos(2\theta_1) e^{i\phi_1^A}, & z > t \\ \tilde{n}_1^B e^{i\phi_1^B} = n_{10}\cos(2\theta_2) e^{i\phi_1^B}, & z < 0 \end{cases}, \tag{4.6}$$

and

$$n_2 = \begin{cases} \tilde{n}_2^A e^{i\phi_2^A} = n_{20} e^{i\phi_2^A}, & z > t \\ \tilde{n}_2^B e^{i\phi_2^B} = n_{20} e^{i\phi_2^B}, & z < 0 \end{cases}. \tag{4.7}$$

Here ϕ_1^μ and ϕ_2^μ, $\mu = A, B$, are the phases of the order parameters in superconductors A and B.

The expression for the supercurrent density can be obtained by the Ginzburg-Landau equations [108, 9] as a function of the two order parameters and evaluated at the interface to find the tunneling current density. For this we need the solution of the order parameter in the interface which is obtained by using the approximation of small thickness compared to the coherence length [7], with boundary conditions as given by Eqs. (4.6) and (4.7). The approximation leads to a linear variation of the order parameter across the interface. Applying the boundary conditions, we obtain

$$n_1 = (1 - z/W)\tilde{n}_1^B e^{i\phi_{1B}} + z/W\tilde{n}_1^A e^{i\phi_{1A}}, \tag{4.8}$$

$$n_2 = (1 - z/W)\tilde{n}_2^B e^{i\phi_{2B}} + z/W\tilde{n}_2^A e^{i\phi_{2A}}, \tag{4.9}$$

Substitution of Eq. (4.8,4.9) into Eq. (4.5) gives the supercurrent density

$$J = \sum_{i,j=1}^{2} J_{cij}\sin(\phi_i^B - \phi_j^A), \tag{4.10}$$

where

$$\begin{array}{rl} J_{c11} = & (2e\hbar/m_d^* t)\tilde{n}_1^A\tilde{n}_1^B \\ J_{c21} = & (2e\hbar/m_\nu^* t)\tilde{n}_1^A\tilde{n}_2^B \\ J_{c12} = & (2e\hbar/m_\nu^* t)\tilde{n}_2^A\tilde{n}_1^B \\ J_{c22} = & (2e\hbar/m_s^* t)\tilde{n}_2^A\tilde{n}_2^B \end{array}, \tag{4.11}$$

are implicit functions of the orientation of the crystalline axis through the tilded order parameters as seen in Eqs. (4.6) and (4.7); m_d^*, m_ν^*, m_s^* are the effective masses that enter into the Ginzburg-Landau equations.

Some special cases are the following

(i) For d-wave symmetry one component of the order parameter vanishes at the interface ($n_2 = 0$). The Josephson current density becomes $J = |J_{c11}|\sin(\phi + \phi_c)$ with $\phi_c = 0$ for $J_{c11} > 0$ and $\phi_c = \pi$ for $J_{c11} < 0$.

(ii) For $d+s$-wave and the restriction where $\phi_2^A - \phi_1^A = \phi_2^B - \phi_1^B = \pi$ is fixed on both sides of the interface, the current density J depends only on one phase difference through the interface, say $\phi = \phi_1^B - \phi_1^A$, and

$$J(\phi) = |\tilde{J}_c|\sin(\phi + \phi_c), \tag{4.12}$$

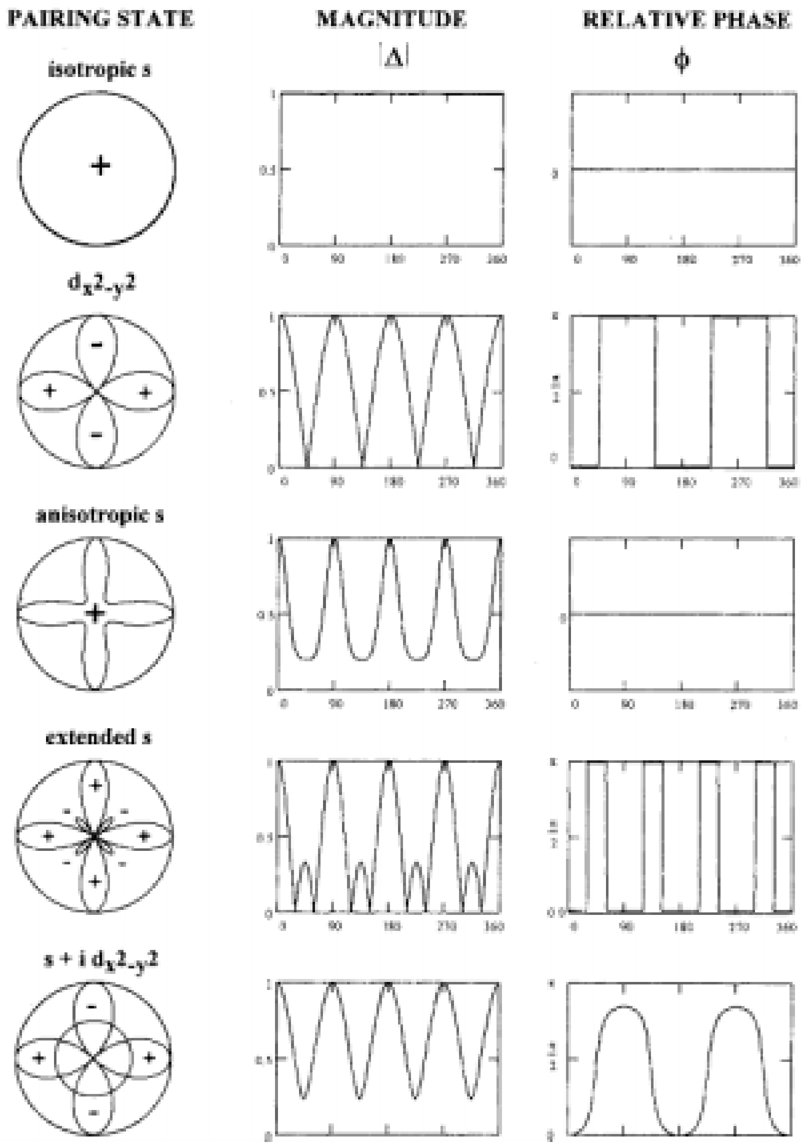

Figure 4.2: Magnitude and phase of the superconducting order parameter as a function of direction in the CuO_2 planes of the cuprates for the candidate pairing states.

with

$$\widetilde{J}_c = J_{c11} + J_{c22} - J_{c12} - J_{c21}. \tag{4.13}$$

In Eq. (4.12) $\phi_c = 0$ for $\widetilde{J}_c > 0$ and $\phi_c = \pi$ for $\widetilde{J}_c < 0$.

(iii) For the $d + is$-wave case the intrinsic phase difference within each superconductor A and B can be assumed to be $\phi_2^A - \phi_1^A = \phi_2^B - \phi_1^B = \pi/2$. The current density J is

$$J(\phi) = \widetilde{J}_c \sin(\phi + \phi_c), \tag{4.14}$$

with

$$\widetilde{J}_c = \sqrt{(J_{c11} + J_{c22})^2 + (J_{c12} - J_{c21})^2}, \tag{4.15}$$

$$\phi_c = \begin{cases} \tan^{-1} \frac{J_2}{J_1}, & J_1 > 0 \\ \pi + \tan^{-1} \frac{J_2}{J_1}, & J_1 < 0 \end{cases}, \tag{4.16}$$

where $J_1 = J_{c11} + J_{c22}$,$J_2 = J_{c21} - J_{c12}$. Equation (4.16), through (4.6,4.7,4.11), defines the relationship, between θ_1, θ_2 and the phase ϕ_c. In Fig. 4.2 we present the magnitude and the relative phase of the possible pairing states.

4.3 Role of the twin boundary

We consider two superconducting sheets A and C which overlap for a distance L with the superconducting sheet B, in the x-direction, [as shown in Fig. 4.1(b)]. The relative phase of the s- and d-wave order parameter in all three superconducting regions is assumed to be $\pi/2$. The regions A and C are separated with a twin boundary, with odd reflection symmetry. At an odd reflection symmetry twin boundary, the relative orientation of the a and b axes changes by $\pi/2$ on reflection across the twin boundary, and the lobes of the s and d order parameter with different sign face each other along the boundary [101]. This symmetry is a consequence of the dominant d-wave order parameter that we have assumed, and the fact that the order parameter is continuous and varies as little as possible at the twin boundary. Experiments have shown that the transition temperature (T_c) of a twinned crystal remains the same following the removal of the twin boundary

[37]. We then choose the angle between the a-axis in region A, and the x-direction to be $\theta_1 = 15°$, causing the angle between the a-axis and the junction interface in region C to be $\theta_3 = 75°$. The missorientation angle of superconductor B with the junction interface is $\theta_2 = 22.5°$. This choice of angles was made intentionally in order to compare our results with those of Ref. [108]. With the above arrangement a simple calculation from Eq. (4.16) yields $\phi_{c1} = 0.01\pi$ in $0 < x < L/2$ and $\phi_{c2} = 1.08\pi$ in $L/2 < x < L$. The current transport across the junction is taken to be only along the z direction. We describe the entire junction with width w small compared to λ_J in the y direction, of length L in the x direction, in external magnetic field H in the y direction. We expect that experiments in Josephson junctions between twinned and untwinned superconductors will show the results that we present. Our analysis can equally well apply to explain the results of Ref. [51]. The superconducting phase difference ϕ across the junction is then the solution of the sine-Gordon equation

$$\frac{d^2\phi(x)}{dx^2} = \frac{1}{\lambda_J^2}\sin[\phi(x) + \phi_c(x)], \tag{4.17}$$

with the inline boundary conditions

$$\frac{d\phi}{dx}|_{x=0,L} = \pm\frac{I}{2} + H. \tag{4.18}$$

The Josephson penetration depth is given by

$$\lambda_J = \sqrt{\frac{\hbar c^2}{8\pi e t \widetilde{J}_c}},$$

where d is the sum of the penetration depths in two superconductors plus the thickness of the insulator layer. We also assume that the critical current density $\widetilde{J}_c$ is constant within each segment of the interface.

The spatial variation of ϕ induces a local magnetic field given by the expression

$$\mathcal{H}(x) = \frac{\Phi_0}{2\pi t}\frac{d\phi(x)}{dx}. \tag{4.19}$$

We can classify the different solutions obtained from Eq. (4.17) with their magnetic flux content

$$\Phi = \frac{\Phi_0}{2\pi}(\phi_R - \phi_L), \tag{4.20}$$

where $\phi_{R(L)}$ is the value of ϕ at the right(left) edge of the junction, and $\Phi_0 = \frac{hc}{2e}$ is the flux quantum.

To check the stability we consider small perturbations $u(x,t) = v(x)e^{st}$ on the static solution $\phi(x)$, and linearize the time-dependent sine-Gordon equation to obtain:

$$\frac{d^2v(x)}{dx^2} + \cos[\phi(x) + \phi_c(x)]v(x) = \lambda v(x), \tag{4.21}$$

under the boundary conditions $\frac{dv(x)}{dx}|_{x=0,L} = 0$, where $\lambda = -s^2$. It is seen that if the eigenvalue equation has a negative eigenvalue the static solution $\phi(x)$ is unstable.

We can also compute the free energy of the solution for zero current and external magnetic field

$$F = \frac{\hbar \widetilde{J}_c w}{2e} \int_0^L \left[1 - \cos\left[\phi(x) + \phi_c(x)\right] + \frac{\lambda_J^2}{2} \left(\frac{\partial \phi}{\partial x} \right)^2 \right] dx. \tag{4.22}$$

Note that the no vortex solution $\phi = 0$ everywhere is not a solution of this problem.

When $\phi_{c1} = \phi_{c2} = 0$ we have the conventional s-wave junction. In case $\phi_{c1} = 0$, $\phi_{c2} = \pi$ we have the d-wave or $d+s$-wave junction. The above cases have time reversal symmetry ($\mathcal{T}$-conservation). When ϕ_{c1}, ϕ_{c2} are slightly different from 0 and π, we have the $d+is$-wave pairing, which is a broken time reversal symmetry state ($\mathcal{T}$ violation). In this chapter, the particular parameters we use are $\phi_{c1} = 0.01\pi$, $\phi_{c2} = 1.08\pi$, and the pairing state is $d+is$.

4.4 Spontaneous flux and interference patterns

We consider first a symmetric $0-\pi$ junction. Here the change of ϕ_c from 0 to π introduces spontaneous flux lines i.e., vortices with half the conventional flux quantum ($\Phi = \pm\Phi_0/2$), if the junction length is much larger then λ_J. We call them half-vortex (h_v) and antivortex (h_{av}) solutions. To obtain these vortices as solutions of Eq. (4.17) for zero

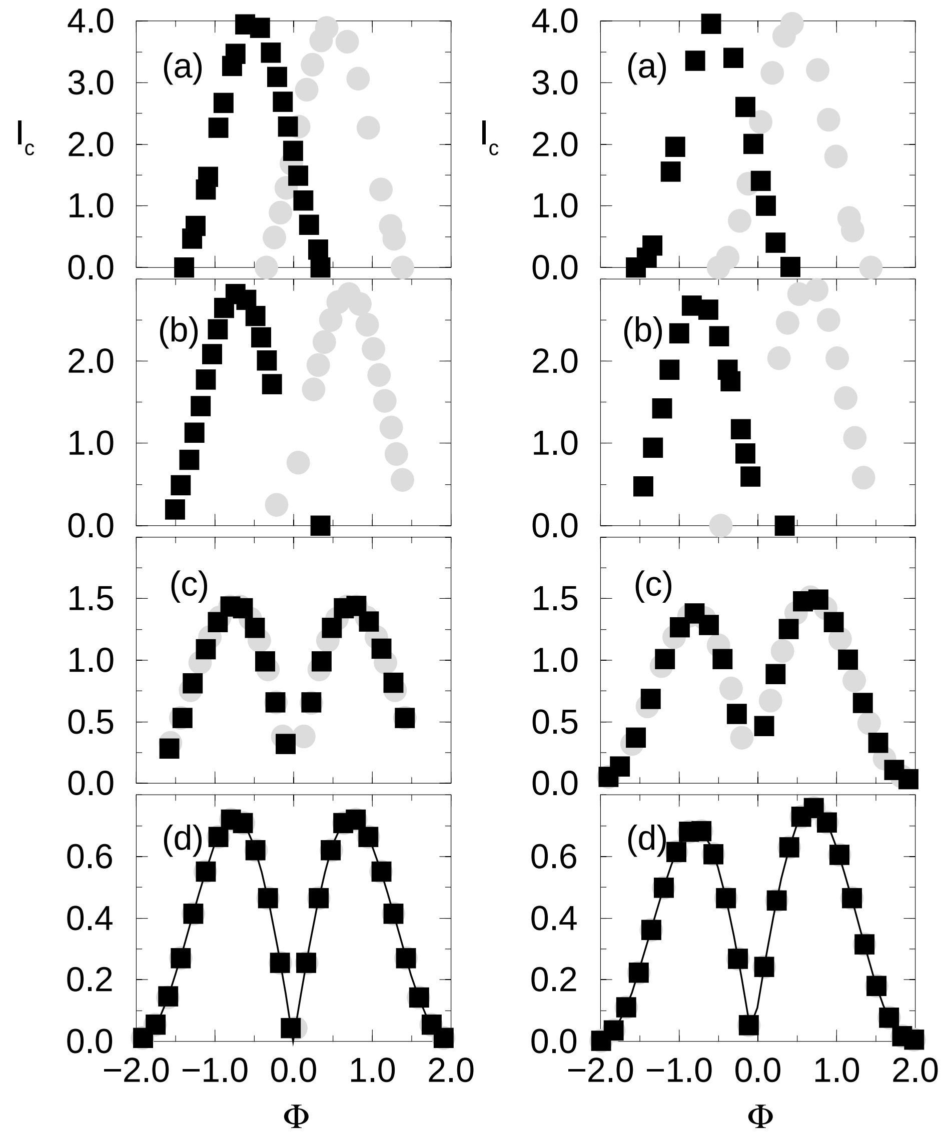

Figure 4.3: Critical current I_c versus the magnetic flux Φ (in units of Φ_0) for a symmetric $0-\pi$ junction(left),and a junction with $d+is$ symmetry (right), for different junction lengths: (a) $L=10$, (b)$L=4$, (c)$L=2$, (d)$L=1$.

current and magnetic field, a kink or antikink like initial condition is used, which is iterated until convergence. Using the h_v and h_{av} solutions as initial conditions and increasing the current we are able to reach the critical current I_c for a given magnetic field. In Fig. 4.3(left) we plot the critical current I_c as a function of the magnetic flux Φ (in units of Φ_0) for different junction lengths: (a) $L = 10$, (b) $L = 4$, (c) $L = 2$, and (d) $L = 1$ ($\lambda_J = 1$). The circles (squares) in this figure correspond to the half vortex (antivortex) branch. For most of the range of existence of h_v (h_{av}) the magnetic flux is positive (negative) while there is a small region where it turns into an antivortex (vortex). A similar calculation has been done in Refs. [105] and [52] where they considered only the h_v solution. As we can see, there is a "dip" at $\Phi = 0$, for lengths as long as $L = 10$.

In the $d + is$-wave case, where $\phi_{c1} = 0.01\pi$ and $\phi_{c2} = 1.08\pi$, the phase ϕ must form a kink or antikink near $x = 0$ in order to match the conditions on both sides. The flux quantization is $\Phi = \chi\Phi_0$ where χ is neither integer nor half-integer. We call the solution with positive flux a fractional vortex (f_v) while the negative flux solution is the fractional antivortex (f_{av}). Note that χ is equal to $1 - (\phi_{c2} - \phi_{c1})/2\pi$ for the (f_v) solution [108] and $(-\phi_{c2} + \phi_{c1})/2\pi$ for the (f_{av}) in the long junction limit.

In Fig. 4.3(right) we present our calculations for the $\mathcal{T}$-violation case where $\phi_{c1} = 0.01\pi$ and $\phi_{c2} = 1.08\pi$. We also plot for $L = 1$ the analytical result (solid line) of Zhu *et al.* [108]. In contrast to the pure d-wave case, for small lengths this pattern is asymmetric and the "dip" in the maximum current does not occur at $\Phi = 0$, but at a finite Φ value. This behavior also exists for lengths as long as $L = 10$.

In Fig. 4.4 and 4.5 we plot I_c vs H for the d and $d + is$-wave states respectively. For large lengths the f_v and f_{av} branches are almost coincident and one might draw the conclusion that the behavior for a long junction is the same independent of the symmetry. The proper quantity to consider though is the total magnetic flux which includes both the contribution from the external field and the induced self-field. It should be remarked that for an s-wave junction the relation between Φ and H is linear for small H so that the plot of I_c vs H or Φ does not show any differences for small H. For higher H, however, the overlapping branches (for long L) are unfolded. In the case of a different

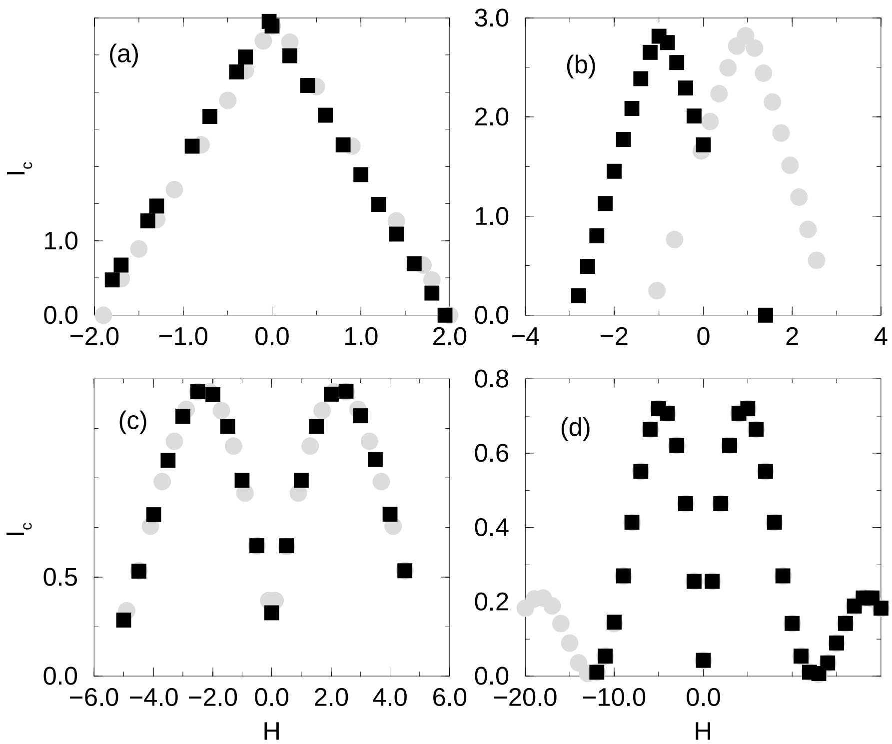

Figure 4.4: Critical current I_c versus the magnetic field H for a symmetric $0-\pi$ junction, for different junction lengths: (a) $L=10$, (b)$L=4$, (c)$L=2$, (d)$L=1$.

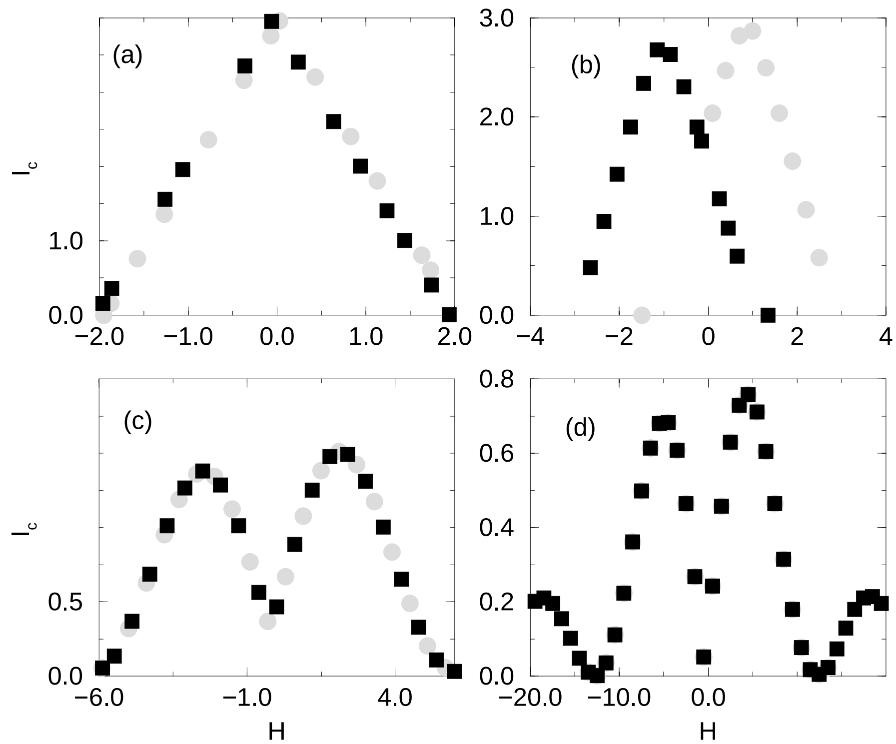

Figure 4.5: Critical current I_c versus the magnetic field H for a symmetric $d + is$ junction, for different junction lengths: (a) $L = 10$, (b)$L = 4$, (c)$L = 2$, (d)$L = 1$.

symmetry even the small H form can change due to the existence of spontaneous magnetization.

In Figs. 4.3(right)(a) and 4.3(right)(b) both f_v and f_{av} branches are stable. There are also unstable branches which are not presented, but are seen in Fig. 4.3(right)(c). The I_c almost coincides for two solutions, one of which is stable and the other unstable. Still we can distinguish the two peaks corresponding to f_v and f_{av}. As expected for the short length ($L = 1$) the stable and unstable branches are exactly coincident. These unstable branches also exist for longer lengths but we need different initial conditions to obtain them due to the strong nonlinear dependence of Φ on the magnetic field H. In the calculations we vary nonmonotonically the magnetic field, but the slope of $\Phi(H)$ changes sign near the boundary separating the stable and unstable solution.

Figure 4.6 addresses the question of spontaneous flux generation in junctions with broken time reversal symmetry ($\mathcal{T}$ violation) as a function of the reduced length (L) and the relative factor of s and d components. The long-dashed line is the result of Ref. [108] which compares with our numerical result (solid line). Both cases have $\phi_{c1} = 0.01\pi, \phi_{c2} = 1.08\pi$. The approximation they made is that the formation of the spontaneous vortex at the junction center simply changes the phase in the left (right) part of the junction by $\phi_{c1}(\phi_{c2})$. This approximation is valid for long junctions but as we can see in Fig. 4.6 does not hold for junctions with lengths less than $10\lambda_J$, since the exponentially decaying analytic solution does not satisfy the zero current boundary conditions at the ends. We have also used two other values for ϕ_{c2}, i.e., 0.9π (dotted line) and 0.8π (dashed line). We conclude that as we decrease the value of ϕ_{c2} the fractional vortex f_v tends out to be a 2π vortex, whereas the fractional antivortex gradually loses its flux content.

In Fig. 4.7(a) we have plotted the magnetic flux Φ (solid line, $\Phi_0 = 1$) versus the value ϕ_{c2} for $L = 10$ and $H = 0$. In the limit $\phi_{c2} = 0$ and $\phi_{c1} = 0$ the junction behaves as the usual s-type junction [74], where the different solutions are distinguished by the number of complete vortices present in the junction. Solutions where the junction contains more than n and less than $n + 1$ vortices we say that they belong to the $(n, n + 1)$ branch. In this case the only stable solution

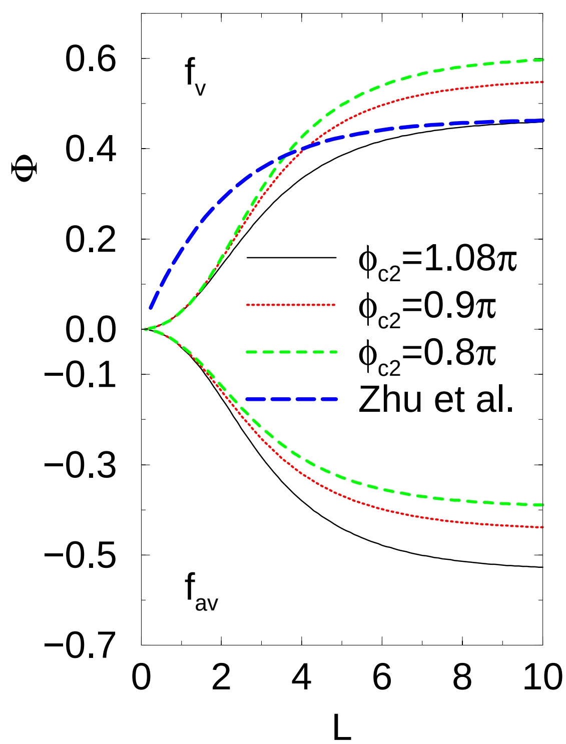

Figure 4.6: The spontaneous magnetic flux Φ as a function of the reduced junction length L, for different values of the intrinsic phase ϕ_{c2} in the right part $L/2 < x < L$ of the junction and $\phi_{c1} = 0.01\pi$.

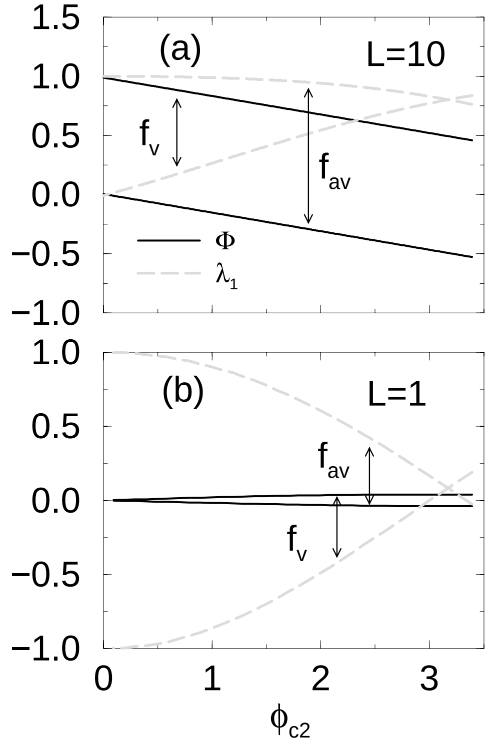

Figure 4.7: The evolution of the fractional vortex f_v and antivortex f_{av} as a function of ϕ_{c2}, for two different lengths (a) $L = 10$, (b) $L = 1$. The stability of theses branches is also denoted by the lowest eigenvalue λ_1 of the linearized eigenvalue problem. Note that the double arrow connects the flux with its stability curve.

present in the junction is that with $\phi = 0$ everywhere. This solution has magnetic flux $\Phi = 0$ and belongs to the $(0, 1)$ branch. The vortex and antivortex solutions with $\Phi = 1$ and $\Phi = -1$, respectively, also exists for $H = 0$, but as seen in Ref. [22] are unstable. As we increase the value ϕ_{c2}, the no vortex solution with $\Phi = 0$ of the usual s-type junction is transformed to the fractional antivortex f_{av}. If we further increase ϕ_{c2} (not presented in the figure) it will reach the full antivortex of the s-wave junction when $\phi_{c2} = 2\pi$. Besides, the unstable vortex solution of the s-type junction with $\Phi = 1$, as we increase ϕ_{c2}, goes to the f_v of the $d + is$ junction stabilizing itself as seen by the stability analysis from which the lowest eigenvalue is also displayed (light line). If we continue increasing the ϕ_{c2} it will go to the no vortex solution of the usual s-type junction. The linear dependence of Φ from ϕ_{c2} can also be seen in the analytical result of Ref. [108] for large lengths, where the approximation they made is valid. When we change ϕ_{c1} and keep $\phi_{c2} = 0$, from 0 to 2π, the $(0, 1)$ branch goes to f_v and then to the unstable $(1, 2)$, while the unstable $(-2, -1)$ branch goes to f_{av} and then to the stable $(0, 1)$.

The situation is a little bit different for small lengths as can be seen from Fig. 4.7(b) where $L = 1$, $H = 0$. Here the stable solution of the s-wave junction will be transformed to the f_{av} of the $d + is$-wave junction, with the increase of ϕ_{c2}, while the unstable $\Phi = 0$ solution of the s-wave junction will go to the stable f_v when ϕ_{c2} is equal to 1.08π. Notice that the magnetic flux remains almost constant - almost zero - which can be expected since we are in the short junction limit where self currents are neglected.

In Fig. 4.8 we plot the ratio F/F_0 of the free energy of the state with some spontaneous flux to the state with no flux. This ratio becomes larger than 1 as we decrease the ϕ_{c2}, for the f_v branch, for small lengths. On the other hand, when $F/F_0 < 1$ the no-flux state is metastable and the final state will be the one with spontaneous flux.

4.5 Conclusions

We have studied the static properties of a one-dimensional junction with $d + is$ order parameter symmetry. The magnetic interference pattern

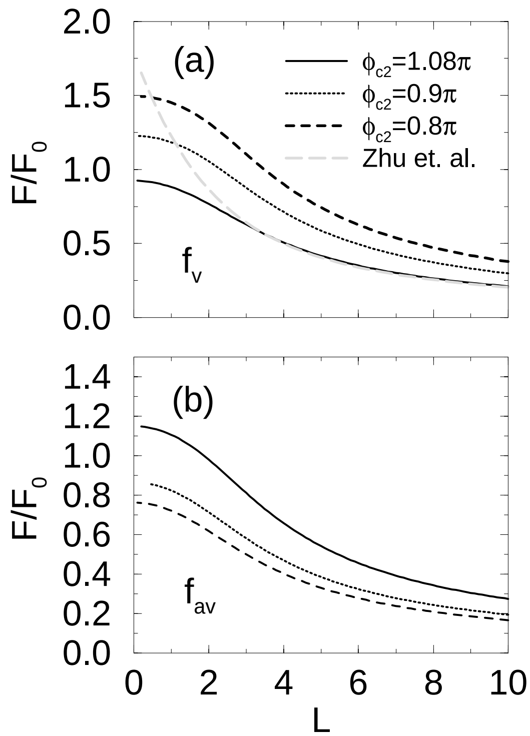

Figure 4.8: The ratio of the free energy F/F_0 as a function of the reduced junction length L, for different values of ϕ_{c2}: (a) f_v, (b) f_{av}.

is asymmetric, and there exist a "dip" near $\Phi = 0$ for lengths as long as $10\lambda_J$. The diffraction pattern of a junction can give us information about the pairing symmetry, at least where junctions are formed.

We have followed the evolution of spontaneously formed vortex and antivortex solutions for different mixing between the s and d components of the order parameter. We have shown that for small lengths the fractional vortex becomes unstable as we decrease the extra phase of the pair transfer integral in the right part of the junction. We conclude that when a mixing state symmetry is realized, the fractional vortex and antivortex solutions evolve differently and this characterizes the $d + is$-wave pairing. We expect these findings to hold even if a bulk $d + s$ state evolves continuously as a function of distance from the interface to a $d + is$ one, as long as the there is a well defined area close to the interface where the time-reversal symmetry is not conserved and the junction is formed.

Chapter 5

Critical currents in Josephson junctions, with unconventional pairing symmetry: $d_{x^2-y^2}+is$ versus $d_{x^2-y^2}+id_{xy}$

5.1 Introduction

One of the main questions in the research activity on high-T_c superconductors nowadays is the identification of the order parameter symmetry and its underlying mechanism[80, 42]. The most possible scenario is that the bulk pairing state has a $d_{x^2-y^2}$-wave character. Theoretical calculations, suggest that an imaginary s-wave component which breaks the time reversal symmetry is induced in some cases, wherever the $d_{x^2-y^2}$-wave order parameter varies spatially such as near a vortex, or near the surface [66]. Also the observation of fractional vortices on a triangular grain boundary in $YBa_2Cu_3O_7$ by Kirtley *et al.* [51], may indicate a possible violation of the time-reversal symmetry near grain boundary. Theoretical explanation of this experiment is given by Bailey et. al. in Ref. [9] where they study a triangular grain boundary in d-wave superconductors. They conclude that under the assumption of

d-wave symmetry the flux at the edges of this triangle can take the values $\pm\Phi_0/2$, which does not agree with the experiment. However under the assumption of $d_{x^2-y^2}+is$-wave symmetry an intrinsic phase shift $\phi_c(x)$ exists in each triangle edge. In turn the phase $\phi(x)$ must change in order to connect the different values of ϕ_c in each segment. This arrangement leads to fractional vortices or antivortices at each three corners, in agreement with the experiment.

Another pairing state which breaks the time reversal symmetry is the $d_{x^2-y^2}+id_{xy}$-wave. Patches of complex d_{xy} components are induced around magnetic impurities at low temperatures in a $d_{x^2-y^2}$-wave superconductor forming a phase coherent state as a result of tunneling between different patches [10]. Violation of parity and time reversal symmetry occurs in this state. Also on the high field region, $H \leq H_{c2}$ the $d_{x^2-y^2}$-wave state can be perturbed by the external filed, producing a $d_{x^2-y^2}+id_{xy}$ state in the bulk [11].

The observation of the splitting of the zero energy peak in the conductance spectra at low temperatures indicates that a secondary component is induced which violates locally the time reversal symmetry [26]. Theoretical explanation based on surface-induced Andreev states, has been proposed [35]. Recently the field dependence of this splitting has been observed in the tunneling spectra of YBCO [6, 60]. This observation is consistent with a $d_{x^2-y^2}+is$ surface order parameter as well as a $d_{x^2-y^2}+id_{xy}$ bulk order parameter. Another question which can be asked is to what extend, the observation of a symmetric magnetic interference pattern in the corner junction experiments [42] is an identification of $d_{x^2-y^2}$-wave symmetry, or could also imply a $d_{x^2-y^2}+id_{xy}$ pairing state also? In this work we propose a phase sensitive experiment based on the Josephson effect, which may be used to distinguish which symmetry ($d_{x^2-y^2}+is$ or $d_{x^2-y^2}+id_{xy}$) the order parameter has near the surface. We study the static properties of a frustrated junction which is made of two one-dimensional junctions, of $d_{x^2-y^2}+ix$-wave, (where $x=d_{xy}$ or $x=s$) and s-wave superconductors. By introducing an extra relative phase in one part of this junction, the above junction can be mapped into the corner junctions experiments[42, 99]. We examine the spontaneous flux and the critical current modulation of the vortex states with the junction orientation angle θ, the magnitude of the secondary component n_s, and the magnetic field H. In each case we derive simple arguments which are useful to discriminate between the time reversal symmetry broken states. For example, when the orientation is exactly such that the lobes of the dominant $d_{x^2-y^2}$-wave order parameter points towards the junction interface the magnetic interference pattern is symmetric (asymmetric) when the secondary order parameter is $x = d_{xy}(s)$. This is verified for small junctions as well as in the long junction limit, and can be used to distinguish between broken time reversal symmetry states.

The rest of the chapter is organized as follows. In Sec. 5.2 we discuss the Josephson effect between a superconductor with broken time reversal symmetry and an s-wave superconductor. In Sec. 5.3 the geometry of the corner junction is discussed. In Sec. 5.4 we present the results for the magnetic flux of the spontaneous vortex states in corner junctions with some intrinsic magnetic flux. In Sec. 5.5 the parameters which can modulate the spontaneous flux and the critical currents are considered. In Sec. 5.6 a connection with the experiment is made. Finally, a summary and discussion are presented in the last section.

5.2 Josephson junction with mixed wave symmetry

We consider the junction shown in Fig. 5.1(a), where two superconductors (A in the region $z > t$ and B in the region $z < 0$), are separated by an intermediate layer. We assume that each superconductor has a two component order parameter. The order parameter for each component $k(k = 1, 2)$ in the superconductors, can be written as

$$n_k = \begin{cases} \tilde{n}_k^A e^{i\phi_k^A}, & z > t \\ \tilde{n}_k^B e^{i\phi_k^B}, & z < 0 \end{cases} . \tag{5.1}$$

Here $\phi_k^{A(B)}$ is the phase of the order parameter n_k in superconductor $A(B)$. Then phenomenological Ginzburg-Landau theory is used to calculate the supercurrent density given by [108]

$$J = \sum_{k,l=1}^{2} J_{ckl} \sin(\phi_k^B - \phi_l^A), \tag{5.2}$$

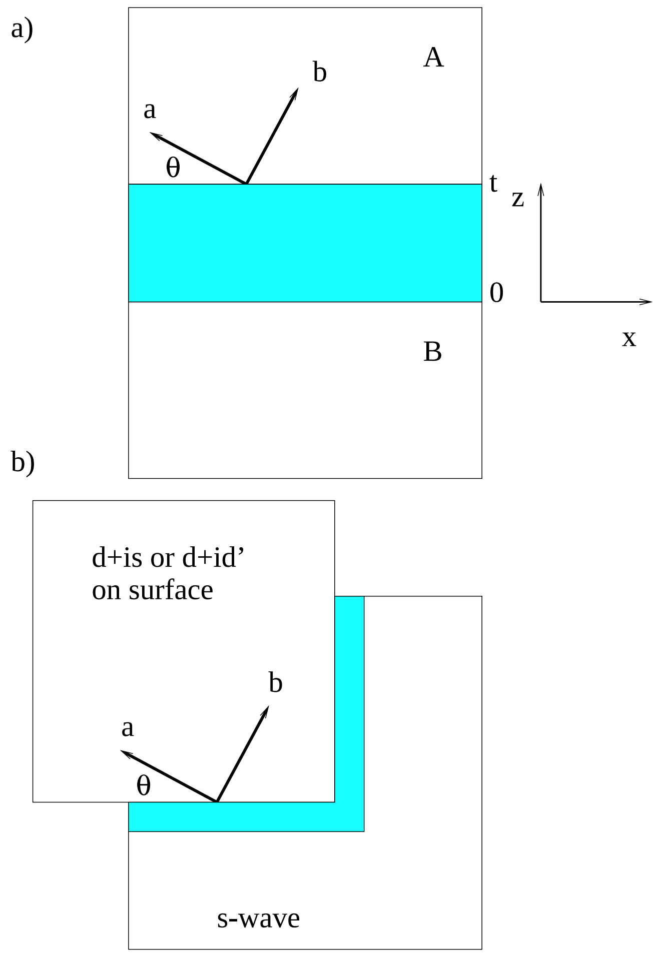

Figure 5.1: (a) A single Josephson junction between superconductors A and B with a two component order parameter. The angle between the crystalline a axis of A and the junction interface is θ. (b) The geometry of the corner junction between a mixed symmetry superconductor, and an s-wave superconductor.

where

$$\begin{array}{rl} J_{c11} = & (2e\hbar/m_a^* d)\tilde{n}_1^A \tilde{n}_1^B \\ J_{c21} = & (2e\hbar/m_\nu^* d)\tilde{n}_1^A \tilde{n}_2^B \\ J_{c12} = & (2e\hbar/m_\nu^* d)\tilde{n}_2^A \tilde{n}_1^B \\ J_{c22} = & (2e\hbar/m_b^* d)\tilde{n}_2^A \tilde{n}_2^B \end{array}, \tag{5.3}$$

m_a^*, m_ν^*, m_b^* are the effective masses that enter into the Ginzburg-Landau equations. In the following these masses are taken equal to an effective mass m^*.

We restrict to the case where B is s-wave. In this case $\tilde{n}_1^B = 0$, and $\tilde{n}_2^B$=constant. We define $\phi = \phi_2^B - \phi_1^A$, as the relative phase difference between the two superconductors. We consider the case where the intrinsic phase difference within superconductor A is $\phi_2^A - \phi_1^A = \pi/2$. Then the order parameter in A is complex and breaks the time reversal symmetry. The supercurrent density can be written as:

$$J(\phi) = \tilde{J}_c \sin(\phi + \phi_c), \tag{5.4}$$

with

$$\tilde{J}_c = \sqrt{J_1^2 + J_2^2}, \tag{5.5}$$

$$\phi_c = \begin{cases} \tan^{-1}\frac{J_2}{J_1}, & J_1 > 0 \\ \pi + \tan^{-1}\frac{J_2}{J_1}, & J_1 < 0 \end{cases}, \tag{5.6}$$

where $J_1 = J_{c21}$, $J_2 = -J_{c22}$. The Josephson critical current density $\tilde{J}_c$ is scaled in units of $J_{c0} = \frac{e\hbar}{m^* d}$. Two special cases are the following:

i) For $d_{x^2-y^2} + is$ wave case the magnitude of the $d_{x^2-y^2}$-wave component in (5.1) is $\tilde{n}_1^A = n_{10}\cos(2\theta)$, where θ is the angle of the crystalline a-axis of superconductor A with the junction interface. The magnitude of the secondary order parameter in superconductor A is $\tilde{n}_2^A = n_{20} = 0.1 n_{10}$.

ii) For $d_{x^2-y^2} + id_{xy}$ wave case, the magnitude of the $d_{x^2-y^2}$-wave component in (5.1) is given by $\tilde{n}_1^A = n_{10}\cos(2\theta)$, while the d_{xy} wave component is $\tilde{n}_2^A = n_{20}\sin(2\theta)$, where $n_{20} = 0.1 n_{10}$. This order parameter can occur in the following way: The order parameter magnitude for the d-wave state $\Delta_0(\theta) = \Delta_0 \cos(2\theta)$ is an equal admixture of pairs with orbital moment $L_z = \pm 2$, and can be written as $\Delta_0(\theta) = (\Delta_0/2)[\exp(2i\theta) + \exp(-2i\theta)]$. In the presence of perturbation such as (feromagnetically) ordered impurity spins S_z the coefficients of $L_z = \pm 2$ components will shift linearly in S_z with opposite signs. The final state will be $\Delta_0(\theta) \rightarrow \Delta_0(\theta) + iS_z\Delta_1(\theta)$, where $\Delta_1(\theta) = \sin(2\theta)$. The strength of the secondary component is proportional to the perturbation S_z.

5.3 The corner junction geometry

We consider the corner junction shown in Fig. 5.1(b), between a superconductor with broken time reversal symmetry at the surface and an s-wave superconductor. If the angle of a-axis with the interface in the x-direction is θ, then the corresponding angle in the z-direction will be $\pi/2 - \theta$. We map the two segments each of length $L/2$ of this junction into a one-dimensional axis. In this case the two dimensional junction can be considered as being made of two one dimensional junctions described in Sec. II connected in parallel. Their characteristic phases ϕ_{c1} and ϕ_{c2} depend upon the angle θ. We call this junction frustrated since the two segments have different characteristic phases ϕ_{c1}, ϕ_{c2}. The fabrication details of corner junctions or superconducting interference devices (SQUIDS), between sample faces at different angles can be found in Ref. [42, 99].

The superconducting phase difference ϕ across the junction is then the solution of the sine-Gordon (s-G)equation

$$\frac{d^2\phi(x)}{dx^2} = \widetilde{J}_c \sin[\phi(x) + \phi_c(x)] - I^{ov}, \tag{5.7}$$

with the boundary conditions

$$\frac{d\phi}{dx}|_{x=0,L} = H. \tag{5.8}$$

The length x is scaled in units of the the Josephson penetration depth given by

$$\lambda_J = \sqrt{\frac{\hbar c^2}{8\pi e d J_{c0}}},$$

where d is the sum of the s-wave, and mixed wave λ_{ab} penetration depths plus the thickness of the insulator layer. The relative phase

Table 5.1: The magnetic flux (Φ) in terms of ϕ_{c1}, ϕ_{c2} for the spontaneous solutions that exist in the corner junction geometry between a superconductor with time reversal broken symmetry and an s-wave superconductor (ϕ_{c1}, ϕ_{c2} is the extra phase difference in the two edges of the corner junction due to the different orientations, of the a-axis of the dominant $d_{x^2-y^2}$-wave superconductor). We present only the minimum flux states $n = 0, -1, 1$.

Vortex state n	Magnetic flux (Φ)
0	$(-\phi_{c2} + \phi_{c1})/2\pi$
1	$(-\phi_{c2} + \phi_{c1} + 2\pi)/2\pi$
-1	$(-\phi_{c2} + \phi_{c1} - 2\pi)/2\pi$

$\phi_c(x)$ is $\phi_{c1}(\phi_{c2})$ in the left (right) part of the junction. The external magnetic field H, scaled in units of $H_c = \frac{\hbar c}{2ed\lambda_J}$ is applied in the y direction, which is considered small compared to λ_J. The bias current per unit length I^{ov} in the overlap geometry is scaled in units of $\frac{c}{4\pi}H_c$, and is uniformly distributed along the entire x axis of the junction.

We can classify the different solutions obtained from Eq. (5.7) with their magnetic flux content

$$\Phi = \frac{1}{2\pi}(\phi_R - \phi_L), \tag{5.9}$$

where $\phi_{R(L)}$ is the value of ϕ at the right(left) edge of the junction, in units of the flux quantum $\Phi_0 = \frac{hc}{2e}$.

5.4 Spontaneous vortex states

Firstly let us consider the case where the two one-dimensional junctions of $d_{x^2-y^2} + ix$-wave where $x = s$ or $x = d_{xy}$, and s-wave supeconductors, each of length $L/2$, described in Sec. II are uncoupled. Then for $0 < x < L/2$ the stable solutions for the s-G equation are $\phi(x) = -\phi_{c1} + 2n_1\pi$, where $n_1 = 0, \pm1, \pm2, ...$, while for $L/2 < x < L$ the stable solutions for the s-G equation are $\phi(x) = -\phi_{c2} + 2n_2\pi$, where $n_2 = 0, \pm1, \pm2, ...$, where ϕ_{c1}, ϕ_{c2}, are the relative phases in each part of the junction due to different orientations. These solutions are plotted

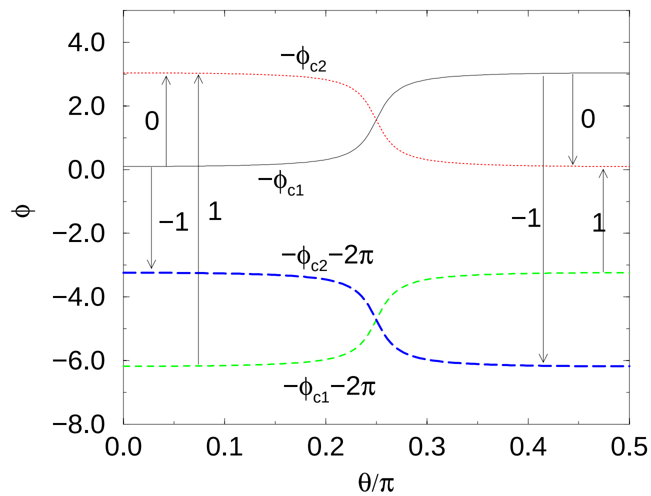

Figure 5.2: The stable solutions $\phi = -\phi_{c1} + 2n_1\pi$ ($\phi = -\phi_{c2} + 2n_2\pi$), for $n_i = 0, -1$, $i = 1, 2$, that exist in the left(right) junction, of $d_{x^2-y^2} + is$-wave and s-wave superconductors, when considered uncoupled, at zero current, versus the orientation angle θ. Each junction has length $L/2$, where $L = 10\lambda_J$, and $\phi_{c1}, (\phi_{c2})$ is the extra phase difference in the left (right) junction due to the different orientations. The arrows denote the variation of the phase ϕ in order to connect these stable solutions in the frustrated junction geometry. We present three possible solutions i.e. $n = 0, -1, 1$, and down(up) arrow denotes negative(positive) magnetic flux.

in Fig. 5.2, for $n_i = 0, -1$, $i = 1, 2$ as a function of the orientation angle θ. When the frustrated junction is formed, and we consider the above junctions in parallel, the phase ϕ is forced to change around $x = L/2$, to connect these stable solutions. This variation of the phase ϕ, along the junction describes the Josephson vortices. The flux content of these states (in units of Φ_0) is [82]

$$\Phi = [\phi(L) - \phi(0)]/2\pi = (-\phi_{c2} + \phi_{c1} + 2n\pi)/2\pi, \tag{5.10}$$

where the n-value ($n = n_1 - n_2 = 0, \pm 1, \pm 2, ...$) distinguishes between solutions with different flux content. We will concentrate to solutions called modes with the minimum flux content i.e., $n = 0, 1, -1$. Their magnetic flux in terms of ϕ_{c1}, ϕ_{c2} is shown in table 5.1. Generally the flux content is fractional i.e. is neither integer nor half-integer, as a consequence of the broken time reversal symmetry of the problem.

In the actual numerical simulations, the stable solutions of the sine-Gordon equation in the left(right) part of the junction are taken as the initial conditions for the iteration procedure. For example for the $n = 0$ solution the phase $\phi(x)$ is taken $\phi(x) = -\phi_{c1}$ ($-\phi_{c2}$) in the left (right) part of the junction, as an initial condition and then is iterated until convergence. Besides if we take as initial condition , $\phi(x) = -\phi_{c1}$, in the left side, and $\phi(x) = -2\pi - \phi_{c2}$ in the right side, the final state of the system, after the iteration procedure, is the solution which we call $n = -1$, with negative magnetic flux, and not exactly opposite to $n = 0$. We comment here that the solutions after the iteration procedure have smooth variation as a function of the position, as opposed to the step function variation of the initial conditions.

For the $0 - 0$ junction $\phi_{c1} = \phi_{c2} = 0$, and the flux becomes $\Phi = n$, so we say that the flux is quantized in integer units of Φ_0. In this case, there exist solutions with flux $\Phi = ..., -1, 0, 1, ...$ [22]. These solutions, when $n \neq 0$ are stabilized by the application of an external magnetic field. In the case of a junction with some spontaneous flux, at least for the modes with lower flux content, the external field is not necessary since the spontaneous magnetization state is stable.

In the case of $0 - \pi$ junction, where the intrinsic phase in the right (left) part of the junction is $\phi_{c2} = -\pi$ ($\phi_{c1} = 0$), the stable solutions of the s-G equation are $\phi(x) = 2n\pi$ for the left part, while $\phi(x) = \pi(2n+1)$

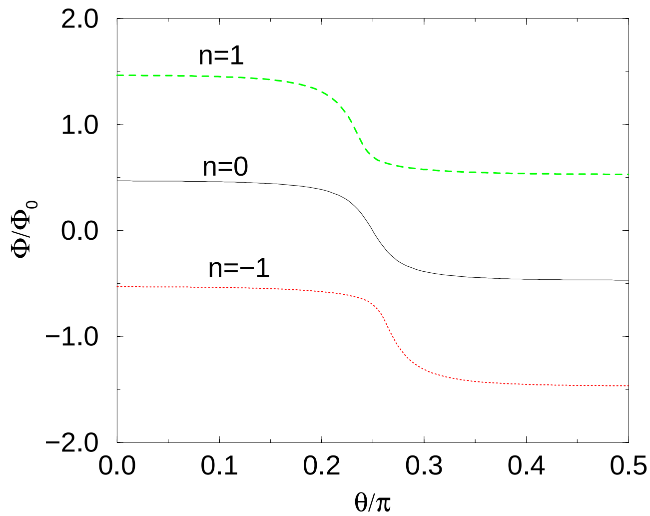

Figure 5.3: The magnetic flux Φ as a function of the angle θ, for the various vortex states, $n = 0, -1, 1$, that exist spontaneously in a corner junction between a $d_{x^2-y^2} + is$-wave and an s-wave superconductor, with length $L = 10\lambda_J$. The flux for $\theta = 0$ is fractional.

for the right part of the junction. In this case a $0-\pi$ junction is formed. The corresponding flux becomes $\Phi = (n + 1/2)\pi$, and the particular values of $n = 0$, $n = -1$ give the half vortex and antivortex solutions, with opposite fluxon content, $\Phi = 0.5$ and $\Phi = -0.5$ respectively.

5.5 Magnetic flux and critical current modulation

In the following we will describe three parameters which can alter the spontaneous flux and the critical currents of the vortex states described in the previous section, in a corner junction between a superconductor with time reversal broken symmetry and an s-wave superconductor. These include the orientation angle θ, the magnitude of the secondary order parameter n_s, and the magnetic field H. In each parameter separately we will point out the differences between the $d_{x^2-y^2} + is$-wave, and $d_{x^2-y^2} + id_{xy}$-wave.

5.5.1 Junction orientation

For the $d_{x^2-y^2} + is$-wave case, we consider first the situation where θ is varied from 0 to $\pi/2$. In Fig. 5.3 we plot the spontaneous magnetic flux versus the angle (θ) for the different modes $n = 0, -1, 1$ in the corner junction geometry. As we can see the magnetic flux changes with orientation. For angles θ close to 0 or $\pi/2$ the spontaneous modes existing at $H = 0$ are separated by an integer value of the magnetic flux. This is also the case in the perfect junction problem. The difference is that the modes are found displaced to fractional values of magnetic flux, contrary to the s-wave case where the magnetic flux takes on integer values at $H = 0$. In particular the vortex solution in the $n = 0$ mode (solid line) contains less that half a fluxon for $\theta = 0$, and as we increase the angle θ towards $\pi/4$ it continuously reduces its flux, i.e. it becomes flat exactly at $\theta = \pi/4$ and then it reverses its sign and becomes an antivortex with exactly opposite flux content at $\theta = \pi/2$ from that at $\theta = 0$. In addition we have plotted in Fig. 5.4a the phase distributions for the mode $n = 0$ in different orientations $\theta = 0, \pi/4, \pi/2$. The transition form the vortex to the antivortex mode as the orientation changes is clearly seen in this figure. Note that the solutions in this mode remain stable for all junction orientations. This is seen in Fig. 5.5 where we plot the lowest eigenvalue (λ_1) of the linearized eigenvalue problem as a function of the angle θ [22]. We see that $\lambda_1 > 0$, denoting stability for all values of the angle θ in this mode.

Let as now examine the solution in the $n = -1$ mode, (dotted line in Fig. 5.3). We see that at $\theta = 0$ it has negative flux, which in absolute value is more than $\Phi_0/2$ and as we increase the angle θ it decreases its flux to a full antifluxon when the orientation is slightly greater than $\pi/4$ and than to flux greater than Φ_0 when θ reaches $\pi/2$. As seen in Fig. 5.5 this solution becomes unstable at a point to the left of $\theta = \pi/4$ (point ι) due to the abrupt change of flux at this angle. More strictly the instability sets in due to the competition between the slope of the phase at the edges of the junction and at the junction center as the angle θ approaches the value $\pi/4$. At this point the slope competition makes the antivortex unstable. This is seen in Fig. 5.4b) (dotted line) where the phase distribution for the $n = -1$ mode solution is plotted at the point where the instability starts i.e. $\theta = 0.242\pi$, for $L = 10\lambda_J$.

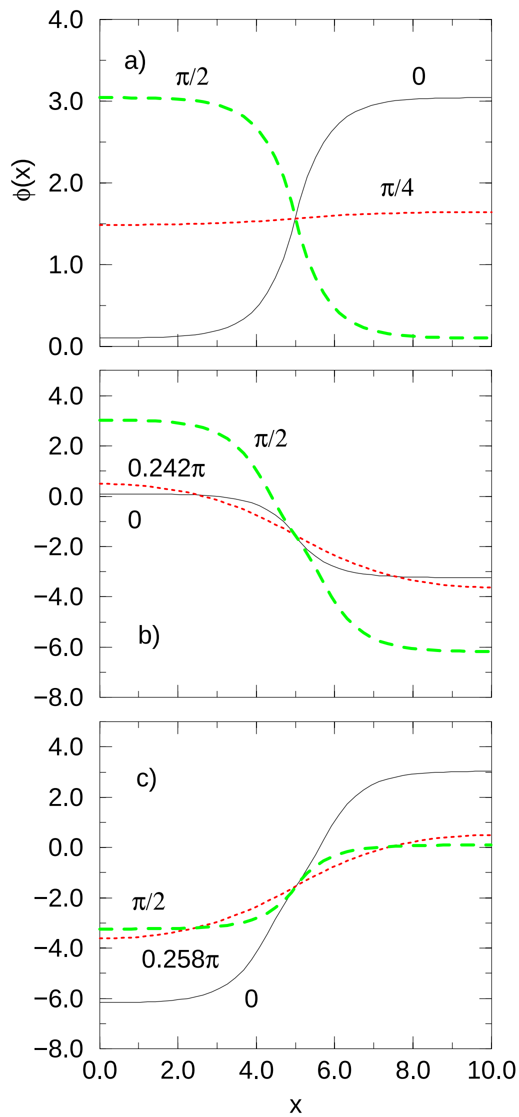

Figure 5.4: The phase distribution of the vortex solutions a) $n = 0$, at $\theta = 0$, $\pi/4$, $\pi/2$; b) $n = -1$, at $\theta = 0$, 0.242π, where the instability sets in, and $\pi/2$; c) $n = 1$, at $\theta = 0$, 0.258π, at the point where the instability occurs, and $\pi/2$, for a corner junction of $d_{x^2-y^2} + is$-wave and s-wave superconductors, with length $L = 10\lambda_J$, and zero overlap external current $I^{ov} = 0$.

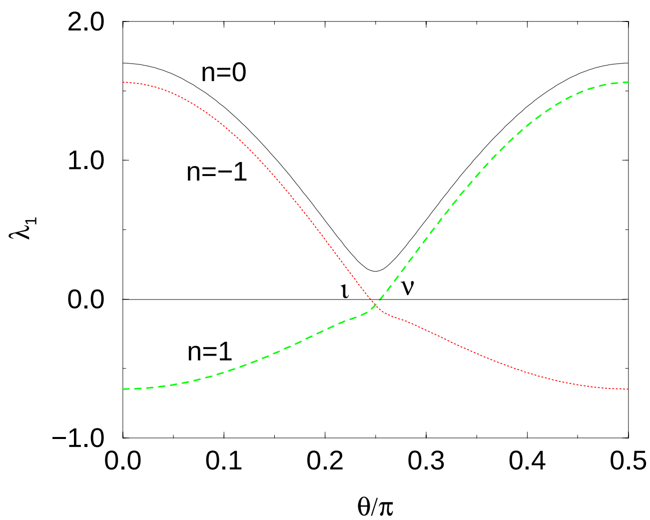

Figure 5.5: The lowest eigenvalue λ_1 of the linearized eigenvalue problem as a function of angle θ, for the $n = 0, -1, 1$ solutions. In the range where θ is close to zero, the eigenvalues for both $n = 0$, and -1 are positive and correspond to stable solutions.

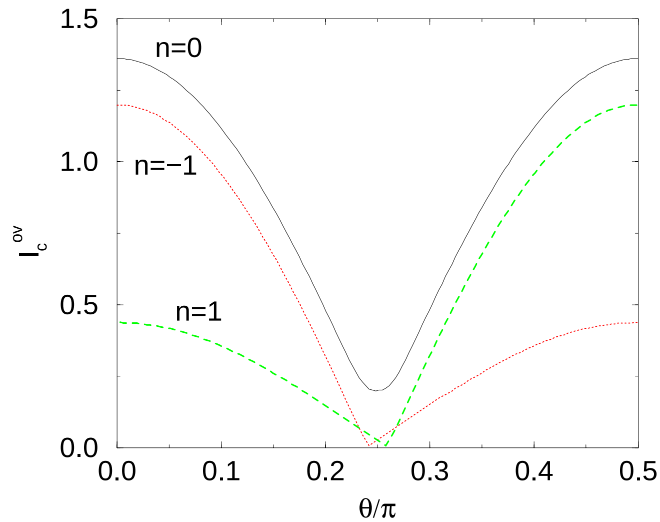

Figure 5.6: Critical overlap current I_c^{ov} per unit length versus the angle θ for a corner junction of $d_{x^2-y^2}+is$-wave and s-wave superconductors, with length $L = 10\lambda_J$, for the vortex solutions $n = 0, -1, 1$ that exist spontaneously in the junction.

Finally the solution in the $n = 1$ mode contains more than one fluxon at $\theta = 0$ and is clearly unstable. It becomes stable at an angle slightly on the right of $\theta = \pi/4$, (point ν in Fig. 5.5) where the flux varies more smoothly, see $\theta = 0.258\pi$ in Fig. 5.4c. At $\theta = \pi/2$ it contains more than $\Phi_0/2$ in flux. We expect a time reversal broken symmetry state like $d_{x^2-y^2}+is$ to be characterized by either the solution in the fractional vortex or antivortex mode, because due to the different character of these solutions a change from one variant to the other would demand the application of an external current or magnetic field and in this sense it would cost additional energy. So since these states are stable in external perturbations, once the system is prepared in one of these it will remain to that state.

In general we see that for each value of θ there exist in the junction a pair of stable solutions which when applying an external bias current will lead to observable critical currents. In Fig. 5.6 we plot the overlap critical current per unit length I_c^{ov} as a function of θ, at $H = 0$, for the $n = 0, -1, 1$-mode solutions, in the $d_{x^2-y^2} + is$-wave case. In the overlap geometry the current is distributed in the entire x-axis. In the calculations we have taken into account that the Josephson critical current density $\widetilde{J}_c$ has a characteristic variation with the orientation. We find that for a given orientation it is possible for the junction current density to vary in the way that several modes with different critical currents can exist.

In Fig. 5.7 we plot the current density when the total current is maximum, for different modes, and orientations, which will give us information about the actual shapes of the vortices. Let us consider the situation where the junction contains a solution in the mode $n = 0$, at $\theta = 0$, when the net current is maximum. The spatial variation of ϕ is described by a fractional vortex which is displaced around the value $\phi = \pi$, from the corresponding distribution at zero current which is around $\pi/2$ (see Fig. 5.4a). The current density distribution as seen in Fig. 5.7a (solid line) at the maximum current is flat above unit with a small variation around the junction center giving rise to the large value on the net current, seen in Fig. 5.6. Also at $\theta = \pi/4$ the flat phase distribution corresponding to the $n = 0$ solution at zero current is displaced towards the value $\phi = \pi$ when applying an external current. The corresponding current distribution seen in Fig. 5.7a, (dotted line) is straight line and the net current is small for this orientation. For the $n = -1$ solution at the point where the instability sets in i.e. $\theta = 0.242\pi$, the current density distribution is symmetric around zero as seen in Fig. 5.7b (dotted line) and carries zero net current at this point. Thus the instability occurs just before the angle where a full antifluxon enters the junction. A slightly different situation occurs in the magnetic interference pattern of a perfect junction [74] where, the net current is zero at the magnetic field where a full fluxon or antiluxon enters the junction, in the no flux 0-mode. At the point $\theta = \pi/2$, of the $n = -1$-mode the junction contains more than one fluxon causing the characteristic oscillations in the current density around the junction center as seen in Fig. 5.7b (dashed line). This reduces the critical current for this orientation.

For the $d_{x^2-y^2} + id_{xy}$ pairing symmetry state, we plot in Fig. 5.8a) the flux content for the $n = 0, -1, 1$, versus the angle θ. Note the half integer or multiplies value of Φ at θ close to 0 or $\pi/2$. For this grain

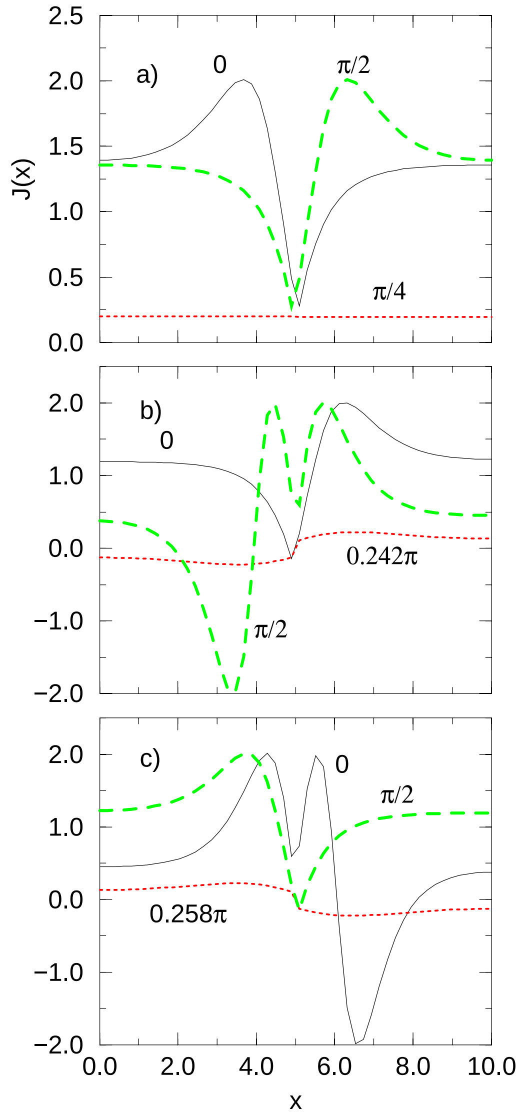

Figure 5.7: The current density distribution $J(x)$ of the vortex solutions a) $n = 0$, at $\theta = 0$, $\pi/4$, $\pi/2$, b) $n = -1$, at $\theta = 0$, 0.242π, where the instability sets in, and $\pi/2$, c) $n = 1$, at $\theta = 0$, 0.258π, at the point where the instability occurs, and $\pi/2$, for a corner junction of $d_{x^2-y^2} + is$-wave and s-wave superconductors, with length $L = 10\lambda_J$, and maximum external overlap current I_c^{ov}.

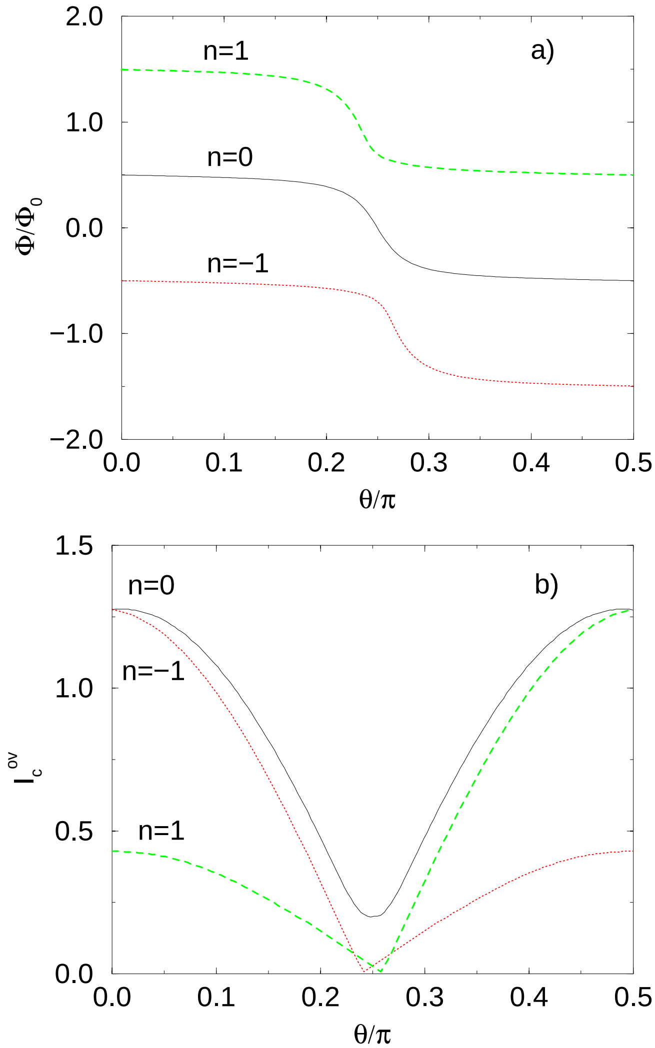

Figure 5.8: a) The spontaneous magnetic flux Φ as a function of the angle θ, for the various vortex states, $n = 0, -1, 1$, for a corner junction between a $d_{x^2-y^2}+id_{xy}$-wave and an s-wave superconductor, with length $L = 10\lambda_J$. The flux for $\theta = 0$ is integer multiply of $\Phi_0/2$. b) The corresponding critical current I_c^{ov} per unit length.

orientation the magnetic flux is only sensitive to the real part of the order parameter, which has a sign change but does not break time-reversal symmetry. In the $d_{x^2-y^2}+is$-wave state the order parameter is complex for all junction orientations and breaks the time-reversal symmetry. Close to 0 or $\pi/2$ the flux is fractional. The flux quantization at $\theta=0$ can be used to discriminate between these states.

In Fig. 5.8b) we plot the critical current per unit length evolution with the grain angle θ in the $d_{x^2-y^2}+id_{xy}$-wave state. Close to $\theta=0$ we see that the I_c^{ov} for the $n=0,-1$ solutions, coincide. This happens also at $\theta=\pi/2$ for the $n=0,1$ solutions. In these orientations the order parameter becomes pure real and does not break the time-reversal symmetry. As a result the critical current at these angles is the same as in a junction with pure d-wave symmetry. At $\theta=\pi/4$ the order parameter is pure imaginary and has the same magnitude for both pairing states. As a consequence for $\theta=\pi/4$, the critical currents for both junctions coincide. Also the unstable part of the $n=1$ branch, in the I_c vs θ is almost the same for the two symmetry states, due to the small difference in the flux, compared with the large flux content of the solutions in this region.

5.5.2 Magnitude of the secondary order parameter

In the above calculations the magnitude of the secondary order parameter is small compared to the dominant (i.e. $n_{20}=0.1n_{10}$). However the maximum fraction of the secondary component that has been observed in phase coherent experiments employing different materials, geometries, and techniques is up to 25% of the dominant [42]. This triggered our interest to study the magnetic flux and also the critical currents as a function of the strength (n_s) of the secondary order parameter, where the magnitude of the dominant order parameter n_d is also varied in a way that $n_s+n_d=1$. When $n_s=0$ only the $d_{x^2-y^2}$-wave order parameter is present, while when $n_s=1$ only the s-wave order parameter appears. This situation can be realized for example near the surface where the $d_{x^2-y^2}$-wave order parameter is suppressed and the s-wave order parameter is enhanced. The result is presented in Fig. 5.9a) and 5.9b) for the $d_{x^2-y^2}+is$-wave case at $\theta=0$. We see that when the secondary component is absent (i.e. $n_s=0$) the picture of

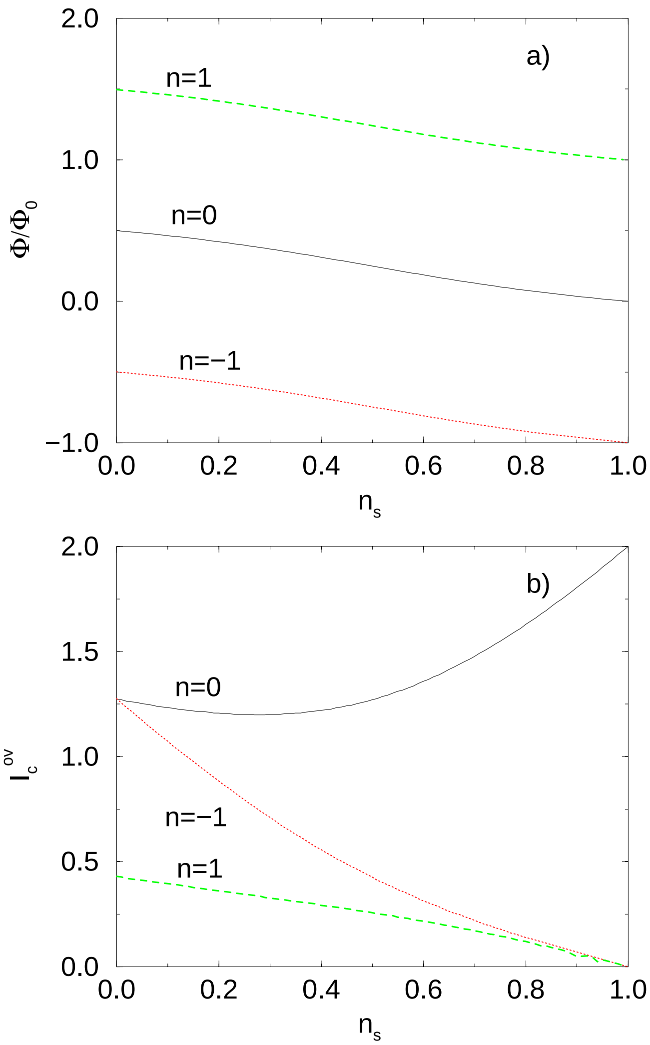

Figure 5.9: a) The spontaneous magnetic flux Φ and b) the critical current I_c^{ov} per unit length versus the strength n_s of the secondary s-wave component for a corner junction of $d_{x^2-y^2}+is$-wave and s-wave superconductors, with length $L = 10\lambda_J$, for the vortex solutions $n = 0, -1, 1$ that exist spontaneously in the junction. The magnitude n_d of the $d_{x^2-y^2}$-wave order parameter is given by the relation $n_s + n_d = 1$.

the $d_{x^2-y^2}$-wave state is reproduced. The same picture also holds for the $d_{x^2-y^2}+id_{xy}$-wave state at $\theta=0$, since the order parameter for the $d_{x^2-y^2}+id_{xy}$-wave state at $\theta=0$ is real not breaking the time-reversal symmetry. So for $\theta=0$ the magnetic flux and the critical current for the $d_{x^2-y^2}+id_{xy}$-wave state would not show any change with the variation of the secondary order parameter d_{xy}. As n_s is increasing the modes $n=0$ and $n=-1$ are no more degenerate, in the sense that their flux deviates from the value $\Phi_0/2$ and $-\Phi_0/2$ respectively and also their critical currents are no longer equal. The mode $n=0$ has larger critical current because it has smaller flux content in absolute value. For values of n_s close to unity, the different modes contain integer magnetic flux, as in the junction between s-wave superconductors, and also their critical currents have the same values as in the perfect junction problem. The conclusion is that the larger the secondary component is in a sample the easier is to be detected in a flux measurement experiment.

5.5.3 Magnetic field

We now examine the influence of the magnetic field on the spontaneous vortices for broken time reversal symmetry pairing states. In Fig. 5.10 we plot the magnetic flux at zero current versus the magnetic field H for the $d_{x^2-y^2}+id_{xy}$-wave state at $\theta=0$. The corresponding critical current as a function of the magnetic field is plotted in Fig. 5.11. In the pure s-wave superconductor junction there is no overlap between different modes in the magnetic flux, and each mode has magnetic flux which is more than $n\Phi_0$ and less than $(n+1)\Phi_0$. In this problem due to spontaneous magnetization the range of the modes is different and in some cases overlapping, and the labeling is with a single index n, corresponding to the pure s-wave superconductor junction (n,n+1) mode [74]. Moreover the range in magnetic flux of each mode is displaced compared to the pure s-wave superconductor junction problem by an amount which corresponds to the intrinsic flux. Also we have the existence of stable vortex states i.e. $n=0,-1$, together with the unstable ones i.e. $n=1$, -2 in a large interval of the magnetic field, which is almost the same. The $n=-2$ mode extends to zero magnetic field, and the reason we didn't examine this mode in Sec. IV is because the

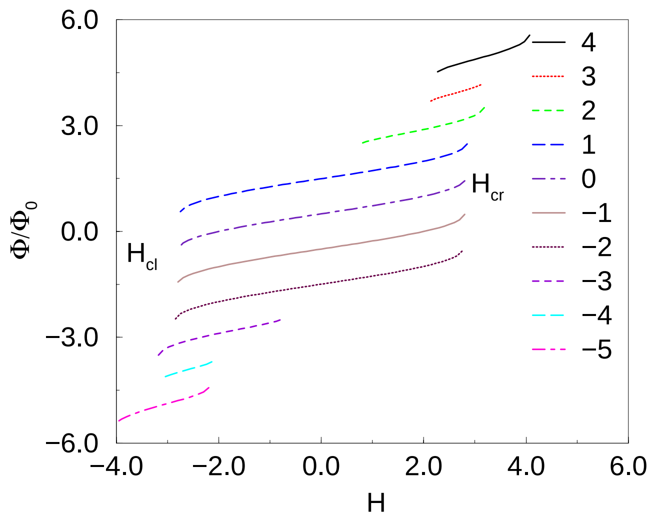

Figure 5.10: Magnetic flux Φ/Φ_0 at zero external current versus the magnetic field H for a corner junction of $d_{x^2-y^2} + id_{xy}$-wave and s-wave superconductors, with length $L = 10\lambda_J$, for angle $\theta = 0°$. $H_{cl}(H_{cr})$ denotes the critical values of the magnetic field where the mode $n = 0$, terminates.

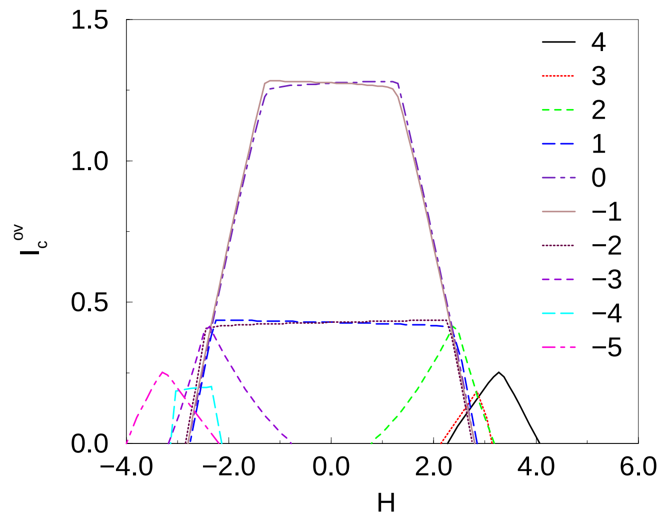

Figure 5.11: Overlap critical current versus the magnetic field H for a corner junction of $d_{x^2-y^2}+id_{xy}$-wave and s-wave superconductors, with length $L=10\lambda_J$, for angle $\theta=0°$.

stability analysis shows negative eigenvalues for all the range of junction orientations, at $H=0$. In the long s-wave junction the extremum of the mode $(0,1)$ in H is the critical field for one fluxon (antifluxon) penetration from the edges, [denoted by H_{cr} (H_{cl}), for the right (left) edge], and is equal to $2(-2)$. The solution for the phase at these extremum values of the field becomes unstable because the value of the phase at the junction edges reaches a critical value. In the problem of a junction with some spontaneous flux, we consider here, the range of the corresponding mode 0 in H is significantly broadened and also the instability at the boundaries sets in due to different reasons. In particular the instability occurs due to the interaction of the flux entering from the junction edges, when the magnetic field reaches the critical value $H_{cr}(H_{cl})$, with the spontaneous flux at the center. Similar features are encountered in the problem of flux pinning from a macroscopic defect in a conventional s-wave junction. [92]

We now examine the magnetic-interference pattern for the two symmetries where the bias current enters in the overlap geometry. In the $d_{x^2-y^2}+id_{xy}$-wave case, where $\theta=0$, this pattern has a symmetric form

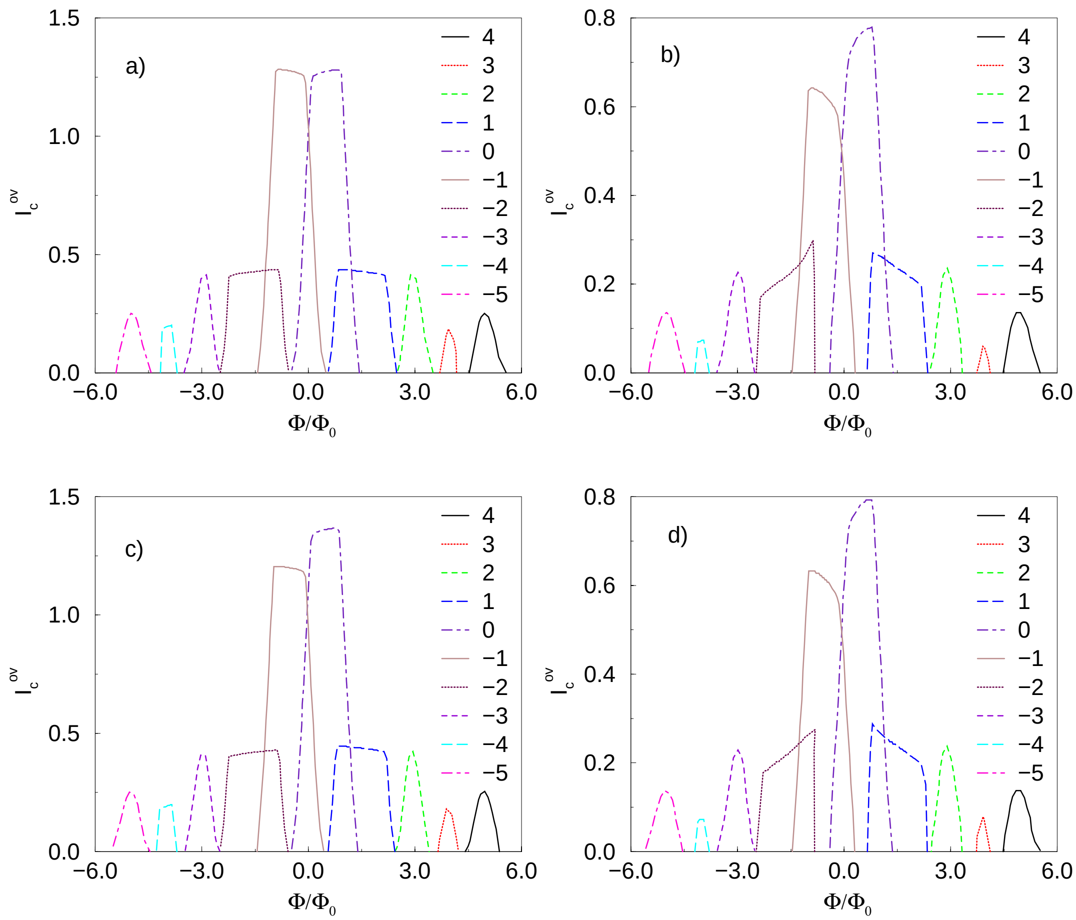

Figure 5.12: (a) Overlap critical current I_c^{ov} per unit length versus the magnetic flux Φ in units of Φ_0, for a corner junction of $d_{x^2-y^2}+id_{xy}$-wave and s-wave superconductors, with length $L = 10\lambda_J$, for angle $\theta = 0°$. (b) The same as in (a) but for $\theta = 0.5$. (c) The same as in (a) but for $d_{x^2-y^2}+is$-wave and s-wave superconductors for angle $\theta = 0°$. (d) The same as in (c) but for $\theta = 0.5$.

as we can see from Fig. 5.12(a). This is because this result is only sensitive to the real part of the order parameter, which has a sign change but does not break time-reversal symmetry. For the angle $\theta = 0.5$ where the order parameter has a finite imaginary part and breaks the time-reversal symmetry this pattern becomes asymmetric and the "dip" appears to a value of flux slightly different than zero. Note that the asymmetry refers mainly to the modes $n = 0$, and $n = -1$. The other modes are not influenced much due to their higher flux content. Also the critical current is suppressed compared to the case where $\theta = 0$ as can be seen in Fig. 5.12(b), due to the drop in J_c.

In the $d_{x^2-y^2} + is$-wave symmetry, in the limit where $\theta \to 0$, the order parameter is complex and the pattern is asymmetric as can be seen in Fig. 5.12c, for the angle $\theta = 0$. This is in agreement with our previous work for the inline current input for a junction with $d_{x^2-y^2} + is$ symmetry [88]. There it was found that the pattern is asymmetric for lengths as long as $L = 10\lambda_J$. For angles close to $\pi/4$, the magnetic interference pattern is similar with the $d_{x^2-y^2} + id_{xy}$-state. This is because the $\sin(2\theta)$ dependence of the d_{xy} component is almost unity. This is seen in Fig. 5.12d where we present the variation of the critical current per unit length versus the enclosed flux for $\theta = 0.5$, and the symmetry state is $d_{x^2-y^2} + is$.

In the short junction limit $L < \lambda_J$ the same argument can be applied without any explicit reference to fractional vortex and antivortex solutions. However as we found in our previous work [88], both $n = 0$ and $n = -1$ (there f_{va}, f_a) exist, with reduced flux content, in this limit as a continuation of the corresponding solutions in the large junction limit. In this case the external applied magnetic field becomes equal to the self field, and the maximum current can be calculated analytically [108],

$$\frac{I_m(\Phi)}{I_{m0}} = \left| \frac{\sin(\pi\Phi/2\Phi_0)\cos[\pi\Phi/2\Phi_0 + (\phi_{c2} - \phi_{c1})/2]}{\pi\Phi/2\Phi_0} \right|. \qquad (5.11)$$

As we see at $\theta = 0$ for the $d_{x^2-y^2} + id_{xy}$-wave case, the relation $\phi_{c2} - \phi_{c1} = n\pi$ holds, and the magnetic interference pattern becomes symmetric, while for the $d_{x^2-y^2} + is$, this difference is a fraction of π and the pattern is asymmetric. However as we increase the junction length, we expect this symmetric pattern for the d-wave order parameter to be continued. This symmetry in the large junction limit, is described more effectively by the assumption of the $n = 0, -1$ solutions which give a symmetric magnetic interference pattern as we presented. Also the $n = -1$ solution extends to values for the magnetic flux, where the $n = 0$ solution is absent. Eliminating one of them will break the symmetry of the diagram.

5.6 Experimental relevance

The symmetric pattern with a minimum at zero applied field observed in corner junction experiments between YBCO and Pb at $\theta = 0$ has been interpreted as an indication of $d_{x^2-y^2}$-wave symmetry. [104, 103] This result refers to short junctions where the junction size is much smaller than the Josephson penetration depth. However as we found here these experimental data are also consistent with an order parameter with $d_{x^2-y^2} + id_{xy}$ pairing symmetry at $\theta = 0$.

Also the critical current I_c versus the magnetic flux Φ of a SQUID, consisting of two planar Josephson junctions on the faces of YBCO superconducting crystal, connected by a loop of a second superconductor, for $\theta = 0$ or $\theta = \pi/2$ is found shifted by $\Phi = 0.5\Phi_0$ and has a minimum at $\Phi = 0$ (instead of a maximum as in a SQUID involving conventional s-wave superconductors or the edge SQUID in which both junctions are on the same crystal face) but is still symmetric. This result has been attributed to an order parameter with $d_{x^2-y^2}$-wave symmetry. However the theoretical analysis done by Beasley et al. [15] shows that it is also consistent with an order parameter with $d_{x^2-y^2} + id_{xy}$-pairing symmetry at $\theta = 0$.

In both cases of SQUID and corner junction the symmetric pattern observed at $\theta = 0$ rules out the $d_{x^2-y^2} + is$-wave pairing state where the order parameter is complex everywhere resulting in an asymmetric I_c versus Φ pattern for all angles θ. However the small asymmetry (less than 2%) observed at $\theta = 0$ in some experiments can be attributed to various complicating factors e.g. fluxon trapping, as will discussed latter.

The experiment proposed here to resolve ambiguity between $d_{x^2-y^2} +$

id_{xy} and $d_{x^2-y^2}$ at $\theta = 0$, is to execute the same experiments using SQUID or corner junction at an angle between sample faces θ between 0 and $\pi/2$. Our calculation predicts symmetric(asymmetric) pattern for the $d_{x^2-y^2}$-wave ($d_{x^2-y^2} + id_{xy}$)-wave pairing state for the corner junction case. This kind of experiment has already been done in the case of SQUID geometry. [99] The tunneling directions are defined lithographically and patterned by ion milling of a c-axis oriented film. A YBCO thin film is patterned into a circle with a series of Nb-Au-YBCO edge junctions at orientations spaced every 7.5°. The measurement of the I_c vs θ, which probes mainly the magnitude of the order parameter has an angular anisotropy, indicating an anisotropic order parameter. Also the execution of these experiments is not easy due to the difficulty in cleaning, polishing a crystal at angle θ, between 0 and $\pi/2$.

Also in an experiment analogous to the corner junction Miller, Ying et. al. [69] used frustrated thin-film tricrystal samples to probe the pairing symmetry of YBCO. They found a minimum in the I_c vs the externally applied flux Φ_e diagram at $\Phi_e = 0$ in the short junction limit and a maximum at $\Phi_e = 0$ for a wide junction where the junction length is much larger than the λ_J. However for a wide junction the correct quantity to be compared should be the total flux Φ which involves contribution both from the externally applied flux and the intrinsic flux.

There is a number of complicating factors in the interpretation of the experiments involving corner junctions that could lead to an asymmetric pattern even for $\theta = 0$. These are the asymmetry of the junction (meaning that the critical current of the two junction faces are not equal). In the SQUID case, this asymmetry will generate circulating current with its own flux and will modify the I_c vs Φ diagram. In general the effects of asymmetry are to suppress, skew and shift the SQUID flux modulation pattern. However in the corner junction case it will only cause the dip to be shallower and will maintain the symmetry of the I_c vs Φ diagram. In order to extract the intrinsic phase shift of the crystal it is necessary either to reduce the asymmetry or to extrapolate the results to the zero current limit. Also these experiments are influenced by the sample geometry and the effect of flux trapping i.e. there can be vortices trapped between the planes of the cuprate superconductors that could affect the I_c vs Φ diagram. In the SQUID case it shifts the flux modulation pattern that is indistinguishable from the intrinsic phase shift arising from the order parameter symmetry, while in the corner junction case, it creates an asymmetry in the flux modulation curves. In this regard the single corner junction experiment may be more accurate in verifying a state with time-reversal symmetry broken. [53] However these flux trapping effects are not sufficiently large to change the qualitative interpretation of these experiments. The probability of flux trapping is smaller for corner junctions than SQUIDs due to the smaller junction area.

The suppression of the order parameter near (110) surfaces give way to subdominant order parameter to be formed at low temperatures. The presence of a subdominant order parameter can be detected by SQUID interferometry where a phase shift between 0 and π should be observed in interfaces in the (110) direction. The phase shift depends on the ratio of the $d_{x^2-y^2}$-wave to the subdominant s or d_{xy} order parameter, and also on the temperature. In the absence of such a state the SQUID will yield a phase shift of 0 or π indicating $d_{x^2-y^2}$-wave symmetry. Alternatively these time-reversal symmetry broken states can be directly observed by measuring the magnetic field distribution around the edge of a superconductor island or hole with the edges along (100) or (110)-directions,using a scanning SQUID microscope. In both cases vortices are formed at the edges consistent with spontaneous currents. [99]

5.7 Conclusions

We studied numerically the possible spontaneous vortex states that may exist in a corner junction between a superconductor with time reversal symmetry broken, (i.e. $d_{x^2-y^2} + id_{xy}$ or $d_{x^2-y^2} + is$), and an s-wave superconductor, in the long junction limit. We studied separately three parameters which can be used to modulate the spontaneous flux. These are the magnetic field H, the interface orientation θ, and the magnitude of the secondary order parameter n_s. We pointed out the differences between time reversal broken states under these modulation parameters.

We found that in flux modulation experiments involving superconductors with some spontaneous flux the range in magnetic flux of each mode is displaced compared to the case of a perfect junction by an amount which corresponds to the intrinsic flux. In particular when the magnetic field H is considered as the modulation parameter, the range in H of the lower fluxon modes is significantly broadened compared to the s-wave case, and the instability at the boundary values of the field sets in due to the interaction of the flux entering from the junction edges with the intrinsic flux. In any case, for each value of the parameter which changes the flux, the modes are separated by a single flux quantum.

We also derived some simple arguments to discriminate between the different pairing states that break the time reversal symmetry. For the $d_{x^2-y^2} + id_{xy}$-wave pairing state, the junction orientation where $\theta = 0$ i.e. the lobes of the dominant $d_{x^2-y^2}$-wave order parameter are at right angles for the corner junction, give flux quantization condition $\Phi = n\Phi_0/2$ as in the $d_{x^2-y^2}$-wave state, which is different from the corresponding flux quantization for the $d_{x^2-y^2} + is$-wave pairing state, at $\theta = 0$, which is $\Phi = (n/2 + f)\Phi_0$, where f is a small quantity. These different conditions provide a way experimentally to distinguish between time reversal broken symmetry states. Note that since the magnitude of the secondary order parameter is small compared to the dominant, the detection of time reversal broken states requires a very precise measurement of the spontaneous magnetic flux.

Also we showed that the magnetic interference pattern at $\theta = 0$ is symmetric (asymmetric) for the $d_{x^2-y^2} + id_{xy}$ ($d_{x^2-y^2} + is$), and this also can be used to probe which symmetry the order parameter has, at least where the junctions are formed. We expect our findings, for the magnetic field dependence of the critical current, to hold even in the short junction limit, where the most experiments on corner junctions have been performed [42, 99].

Chapter 6

Concluding remarks

In this report we discussed phase sensitive tests of the pairing symmetry in unconventional superconductors. These tests give direct evidence in favor of dominant d-wave pairing symmetry in cuprate superconductors. However it does not suggest a mechanism for high-temperature superconductivity. A number of other features such as the pseudogap, pairing interactions, the anomalous normal state and the stripe phase should be considered in order to provide a possible mechanism. Also this have to be established by impurity-doping experiments, and other techniques that are sensitive to the interactions that mediate the superconductivity.

The possibility of coexistence of subdominant s-wave or d_{xy}-wave components with the predominant bulk d-wave state near surfaces has been extensively discussed. This subdominant order parameter breaks the time reversal symmetry and modifies the junction's properties. However further experimental tests are needed to provide the origin of such states.

Using the magnetization and critical current measurements the signature of various types of defects (twin boundaries oxygen vacancies site defects) could be discovered, which could help to tailor devices with the desired critical current.

Phase sensitive tests on the pairing symmetry should be carried out in other superconducting systems such as the organic superconductors or heavy-fermion superconductors in future experiments in order to test for unconventional superconductivity. Also it is important to apply the phase sensitive techniques in other cuprate materials beyond YBCO in order to examine whether the apparent d-wave pairing is specific to YBCO or whether it also occurs in materials with similar layered structure.

The applications of HTS include the microwave filters for mobile phones base stations, wires and cables for current limiters, beam-steering magnets in high-energy accelerators and energy-storage systems. Also the bistable magnetic-flux state in a π ring can be used for quantum computation. Quantum computation is based on the superposition principle of quantum mechanics.

Acknowledgments

I would like to express my great gratitude to my supervisor N. Flytzanis for his great help and guidance throughout the study.

I am grateful to N. Lazaridis, for discussions on the fluxon dynamics, and also to A.V. Balatsky for stimulating my interest to $d_{x^2-y^2} + id_{xy}$ symmetry. I thank J. Betouras for discussions on the Ginsburg-Landau theory and the Hubburd model. I wish also to acknowledge useful discussions with Prof. Dr. Zoran Radovik during his visit in the Physics Department, in Crete, Dec. 1999. I am also grateful to G.C. Psaltakis, J. Giapinzakis, G. Varelogianis for interesting and stimulating discussions.

I would also like to thank all my colleagues in Department of Physics, University of Crete for always being kind and helpful and for having an excellent collaboration. I wish to thank the stuff of the computer center.

Financial support is acknowledged from the Department of Physics, University of Crete through its graduate programme and also from the Institute of Electronic Structure and Laser (I.E.S.L.), of the Foundation for Research and Technology - Hellas (FO.R.T.H.). My participation to the conference "Anomalous, complex superconductors" in Crete, 1998, and also to several Greek conferences on Solid State Physics was made possible through a fellowship from IESL, FORTH, which I greatfully acknowledge.

Bibliography

[1] In V.V. Molshchakov, P.H. Kes, and E.H. Brandt, editors, *Proceedings of the first Euroconference on Vortex Matter in Superconductors at Extreme Scales and Conditionsi, Crete, Greece, September 18-24, 1999*, North Holland, 2000. Elsevier Sience.

[2] M. Abramowitz and I.A. Stegun. *Handbook of Mathematical Functions*. Dover, New York, 1965.

[3] A.A. Abrikosov. *Sov. Phys. - JETP*, 5:1174, 1957.

[4] N. Alexeeva and T. Boyadjiev. *Bulgarian Jour. of Physics*, 24:63–73, 1997.

[5] P.W. Anderson and J.M. Rowell. *Phys. Rev. Lett.*, 10:230, 1963.

[6] M. Aprili, E. Badica, and L.H. Greene. *Phys. Rev. Lett.*, 83:4630, 1999.

[7] L.G. Aslamazov and A.I. Larkin. *JETP Lett.*, 9:87, 1969.

[8] J. Ayache, A. Torel, J. Lesueur, and U. Dahmen. *J. Appl. Phys.*, 84:4921, 1998.

[9] D.B. Bailey, M. Sigrist, and R.B. Laughlin. *Phys. Rev. B*, 55:15239, 1997.

[10] A. V. Balatsky. *Phys. Rev. Lett.*, 80:1972, 1998.

[11] A.V. Balatsky. *Phys. Rev. B*, 61:6940, 2000.

[12] L. Balents and S.H. Simon. *Phys. Rev. B*, 51:6515, 1995.

[13] J.B. Bardeen, L.N. Cooper, and J.R. Schrieffer. *Physical Review*, 108:1175, 1957.

[14] A. Barone and G. Paternó. *Physics and Applications of the Josephson Effect.* John Wiley & Sons, New York, 1982.

[15] M.R. Beasley, D. Lew, and R.B. Laughlin. *Phys. Rev. B*, 49:12330, 1994.

[16] J.G. Bednorz and K.A. Muller. *Z. Phys. B*, 64:186, 1986.

[17] J.J. Betouras and R. Joynt. *Phys. Rev. B*, 57:11752, 1998.

[18] D. Brown, M. Forest, B. Miller, and N. Petersson. *SIAM J. Appl. Math.*, 54:1048–1066, 1994.

[19] L.N. Bulaevskii, V.V. Kuzii, and A.A. Sobyanin. *JETP Lett.*, 25:290, 1977.

[20] A. Callegari and E. Reiss. *J. Math. Phys.*, 14:276, 1973.

[21] C. Camerlingo, C. Nappi, M. Russo, G. Testa, E. Mezzetti, R. Gerbaldo, G. Ghigo, and L. Gozzelino. *Phys. C*, 332:93, 2000.

[22] J.-G. Caputo, N. Flytzanis, Y. Gaididei, N. Stefanakis, and E. Vavalis. *Supercond. Sci. Technol.*, 13:423–438, 2000.

[23] J.G. Caputo, N. Flytzanis, Y. Gaididei, and E. Vavalis. *Phys. Rev. E*, 54:2092, 1996.

[24] J.G. Caputo, N. Flytzanis, and E. Vavalis. *Int. J. Modern Physics*, C7:191, 1996.

[25] T.C. Chow, H. Chou, H.G. Lai, C.C. Liu, and Y.S. Gou. *Phys. C*, 245:143, 1995.

[26] M. Covington, M. Aprili, E. Paraoanu, L.H. Greene, F. Xu, J. Zhu, and C.A. Mirkin. *Phys. Rev. Lett.*, 79:277, 1997.

[27] M. Covington, R. Scheuerer, K. Bloom, and L. Greene. *Appl. Phys. Lett.*, 68:1717, 1996.

[28] R. Dickey. Stability theory for the damped Sine–Gordon equation. *SIAM J. Appl. Math.*, 30:248–262, 1976.

[29] D. Dimos, P. Chaudhari, and J. Mannhart. *Phys. Rev. B*, 41:4038, 1995.

[30] H. Ding, M. R. Norman, J. C. Campuzano, M. Randeria, A. F. Bellman, T. Yokoya, T. Takahashi, T. Mochiku, and K. Kadowaki. *Phys. Rev. B*, 54:9678, 1996.

[31] V.J. Emery and S.A. Kivelson. *Nature*, 374:434, 1995.

[32] R. Fehrenbacher, V.B. Geshkenbein, and G. Blatter. *Phys. Rev. B*, 45:5450, 1992.

[33] A.T. Filippov, Yu.S. Gal'pern, T.L. Boyadjiev, and I.V. Puzynin. *Phys. Lett. A*, 120:47, 1987.

[34] R. Flesch, M.G. Forest, and A. Sinha. *Phys. D*, 48:169–231, 1991.

[35] M. Fogelstrom, D. Rainer, and J.A. Sauls. *Phys. Rev. Lett.*, 79:281, 1997.

[36] R. Gerdemann, K. D. Husemann, R. Gross, L. Alff, A. Beck, B. Elia, W. Reuter, and M. Siegel. *J. Appl. Phys.*, 76:8005, 1994.

[37] J. Giapintzakis, D.M. Ginsberg, and P.-D. Han. *J. Low Temp. Phys.*, 77:155, 1989.

[38] L.P. Gorkov. *Sov. Phys. - JETP*, 9:1364, 1959.

[39] R. Gross, P. Chaudhari, D. Dimos, , A. Gupta, and G. Kozen. *Phys. Rev. Lett.*, 64:228, 1990.

[40] R. Gross, P. Chaudhari, M. Kawasaki, M.B. Ketchen, and A. Gupta. *Phys. Rev. Lett.*, 57:727, 1990.

[41] W. N. Hardy, D. A. Bonn, D. C. Morgan, Ruixing Liang, and Kuan Zhang. *Phys. Rev. Lett.*, 70:3999, 1993.

[42] D.J. Van Harlingen. *Rev. Mod. Phys.*, 67:515, 1995.

[43] L.C. Hebel and C.P. Slichter. *Phys. Rev.*, 107:901, 1957.

[44] H. F. Hess, R. B. Robinson, R. C. Dynes, J. M. Valles Jr., and J. V. Waszczak. *Phys. Rev. Lett.*, 62:214, 1989.

[45] R.P. Huebener. *Adv. Electron. Elect. Phys.*, 70:1, 1988.

[46] E. Ilichev, V. Zakosarenko, R.P.J. Isselsteijn, V. Schultze, H.-G. Meyer, H.E. Hoenig, and H. Topfer. *IEEE Trans. Appl. Supercond.*, 9:3994, 1999.

[47] M. A. Itzler and M. Tinkham. *Phys. Rev. B*, 51:435, 1995.

[48] B.D. Josephson. *Phys. Rev. Lett.*, 1:251, 1962.

[49] J.H. Miller Jr., Q.Y. Ying, Z.G. Zou, N.Q. Fan, J.H. Xu, M.F. Davis, and J.C. Wolfe. *Phys. Rev. Lett.*, 74:2347, 1995.

[50] M.B. Ketchen. *IEEE Trans. Magnetics*, 27:2916, 1991.

[51] J.R. Kirtley, P. Chaudhari, M.B. Ketchen, N. Khare, S.Y. Lin, and T. Shaw. *Phys. Rev. B*, 51:12057, 1995.

[52] J.R. Kirtley, K.A. Moler, and D.J. Scalapino. *Phys. Rev. B*, 56:886, 1997.

[53] J.R. Kirtley, K.A. Morel, G. Villard, and A. Maignan. *Phys. Rev. Lett.*, 81:2140, 1998.

[54] J.R. Kirtley, C.C. Tsuei, and L.S. Yu-Jahnes. *Nature (London)*, 373:225, 1995.

[55] Yu.S. Kivshar, N. Gronbech-Jensen, and M.R. Samuelsen. *Phys. Rev. B*, 45:7789, 1992.

[56] A.W. Kleinsasser, W.H. Mallison, R.E. Miller, and G.B. Arnold. *IEEE Trans. Appl. Supercond.*, 5:2735, 1995.

[57] K.A. Kouznetsov, A.G. Sun, B. Chen, A.S Katz, S.R. Bahcall, J. Clarke, R.C. Dynes, D.A. Gajewski, S.H. Han, M.B. Maple, J.Giapintzakis, J.-T. Kim, and D.M. Ginsberg. *Phys. Rev. Lett.*, 79:3050, 1997.

[58] V.M. Krasnov, V.A. Oboznov, and N.F. Pedersen. *Phys. Rev. B*, 55:14486, 1997.

[59] K. Kroger, L.N. Smith, and D.W. Jllie. *Appl. Phys. Lett.*, 280, 1994.

[60] R. Krupke and G. Deutscher. *Phys. Rev. Lett.*, 83:4634, 1999.

[61] L. Landau and I. Lifshitz. *Classical Mechanics.* Pergamon Press, New York, 1987.

[62] B.H. Larsen, J. Mygind, and A.V. Ustinov. *Phys. Lett. A*, 193:359, 1994.

[63] K.K. Likharev and V.K. Semenov. *IEEE Trans. Appl. Supercond.*, 1:3, 1991.

[64] J. Ma, C. Quitmann, R.J. Kelley, H. Berger, G. Margaritondo, and M. Onellion. *Europhys. Lett.*, 31:119, 1995.

[65] J. Mannhart, B. Mayer, and H. Hilgenkamp. *Z. Phys. B*, 101:175, 1996.

[66] M. Matsumoto and H. Shiba. *J. Phys. Soc. Jpn.*, 64:1703, 1995.

[67] D.E. McCumber. *J. Appl. Phys.*, 39:3113, 1968.

[68] E. Mezzetti, A. Chiodoni, R. Gerbaldo, G. Ghigo, L. Gozzelino, B. Minetti, C. Camerlingo, and A. Monaco. *Phys. C*, 332:115, 2000.

[69] D.J. Miller, H. Talvacchio, D.B. Buchholz, and R.P.H Chang. *Appl. Phys. Lett.*, 66:2561, 1995.

[70] K.A. Musaelian, J. Betouras, A.V. Chubukov, and R. Joynt. *Phys. Rev. B*, 53:3598, 1996.

[71] V.A. Oboznov and A.V. Ustinov. *Phys. Lett. A*, 139:481, 1989.

[72] T. Oka, Y. Itoh, Y. Yanagi, H. Tanaka, S. Takashima, Y. Yamada, and U. Mizutani. *Phys. C*, 200:55, 1992.

[73] J. Orenstein and A.J. Millis. *Science*, 288:468, 2000.

[74] C.S. Owen and D.J. Scalapino. Vortex structure and critical currents in josephson junctions. *Phys. Rev.*, 164:538–544, 1967.

[75] J. A. Pals, W. van Haeringen, and M. H. van Maaren. *Phys. Rev. B*, 15:2592, 1977.

[76] C.H. Pennington and C.P. Slichter. *Physical Properties of High T_c sperconductors II.* Word Scientific, 1994.

[77] G. Reinisch, J.C. Fernandez, N. Flytzanis, M. Taki, and S. Pnevmatikos. *Phys. Rev. B*, 38:11284, 1998.

[78] Y. Ren, J.H. Xu, and C.S. Ting. *Phys. Rev. B*, 53:2249, 1996.

[79] E. Sarnelli, P. Chaudhari, and J. Lacey. *Appl. Phys. Lett.*, 62:777, 1993.

[80] D.J. Scalapino. *Phys. Rep.*, 250:329, 1995.

[81] Z.-X. Shen, D. S. Dessau, B. O. Wells, D. M. King, W. E. Spicer, A. J. Arko, D. Marshall, L.W. Lombardo, A. Kapitulnik, P. Dickinson, S. Doniach, J. DiCarlo, T. Loeser, and C. H. Park. *Phys. Rev. Lett.*, 70:1553, 1993.

[82] M. Sigrist. *Prog. Theor. Phys.*, 99:899, 1998.

[83] M. Sigrist and T.M. Rice. *Z. Phys. B*, 68:9, 1987.

[84] M. Sigrist and T.M. Rice. *J. Phys. Soc. Jpn.*, 61:4283, 1992.

[85] N. Stefanakis and N. Flytzanis. Critical currents in josephson junctions with unconventional pairing symmetry: $d_{x^2-y^2}+is$ versus $d_{x^2-y^2}+id_{xy}$. Accepted for publication in Phys. Rev. B.

[86] N. Stefanakis and N. Flytzanis. Maximum tunneling current in a josephson junction with a large defect. In *International Conference, Solitons and Coherent Structures in Physics and Biology*, Lyngby, Denmark, 1997.

[87] N. Stefanakis and N. Flytzanis. Static characteristics of a josephson junction and stability analysis. In *Proceedings, 14th Greek conference in Solid State Physics*, pages 433–436, Ioanina, 1998.

[88] N. Stefanakis and N. Flytzanis. *Phys. Rev. B*, 61:4270–4275, 2000.

[89] N. Stefanakis and N. Flytzanis. *Phys. C*, 332(1-4):349, 2000.

[90] N. Stefanakis and N. Flytzanis. Critical currents in josephson junctions with time-reversal broken symmetry. In *Conference, Non-Fermi liquid effects in metallic systems with strong electronic correlations*, Campridge, United Kingdom, 2000.

[91] N. Stefanakis and N. Flytzanis. Josephson junction with anisotropic order parameter symmetry. In *Proceedings, 16th Greek conference in Solid State Physics*, Nafplio, 2000.

[92] N. Stefanakis and N. Flytzanis. Critical currents in josephson junctions with macroscopic defects. *Supercond. Sci. Technol.*, 14:16–29, 2001.

[93] N. Stefanakis, M. Kostakis, N. Flytzanis, J.G. Caputo, and E. Vavalis. Josephson junction with macroscopic defects. In *Proceedings, 13th Greek conference in Solid State Physics*, pages 327–330, Thesalonikh, 1997.

[94] A. Takagi, T. Yamazaki, T. Oka, Y. Yanagi, Y. Itoh, M. Yoshikawa, Y. Yamada, and U. Mizutani. *Phys. C*, 250:222, 1995.

[95] M. Takigawa, P.C. Hammel, R.H. Heffner, and Z. Fisk. *Phys. Rev. B*, 39:7371, 1989.

[96] M. Tinkham. *Introduction to superconductivity.* McGraw-Hill, New York, 1975.

[97] C.C. Tsuei, J.R. Kirtley, C.C Chi, L.S. Yu-Jahnes, A. Gupta, T. Shaw, J.Z. Sun, and M.B. Ketchen. *Phys. Rev. Lett.*, 73:593, 1994.

[98] C. J. van der Beek, M. Konczykowski, R.J. Drost, P.H. Kes, A.V. Samoilov, N. Chikumoto, S. Bouffard, and M.V. Feigel'man. *Phys. C*, 332:178, 2000.

[99] D.J. van Harlingen, J.E. Hilliard, B.L.T. Plourde, and B.D. Yanoff. *Phys. C*, 317-318:410, 1999.

[100] M. Virokur and A.E. Koshelev. *JETP*, 70:547, 1990.

[101] M.B. Walker and J. Luettmer-Strathmann. *Phys. Rev. B*, 54:588, 1996.

[102] Th. Wolf, A-C. Bornarel, H. Kupfer, R. Meier-Hirmer, and B. Obst. *Phys. Rev. B*, 56:6308, 1997.

[103] D.A. Wollman, D.J. Van Harlingen, J. Giapintzakis, and D.M. Ginsberg. *Phys. Rev. Lett.*, 74:797, 1995.

[104] D.A. Wollman, D.J. Van Harlingen, W.C. Lee, D.M. Ginsberg, and A.J. Leggett. *Phys. Rev. Lett.*, 71:2134, 1993.

[105] J.H. Xu, J.H. Miller, and C.S. Ting. *Phys. Rev. B*, 51:11958, 1995.

[106] T. Yamashita and L. Rinderer. *J. Low Temp. Phys.*, 21:153, 1975.

[107] T. Yamashita, L. Rinderer, K. Nakajima, and Y. Onodera. *J. Low Temp. Phys.*, 17:191, 1974.

[108] J.-X. Zhu, W. Kim, and C.S. Ting. *Phys. Rev. B*, 58:6455, 1998.